

SUPERCONTINUUM GENERATION AND COMPRESSION

A dissertation submitted to the
SWISS FEDERAL INSTITUTE OF TECHNOLOGY ZURICH
for the degree of
DOCTOR OF NATURAL SCIENCES

presented by
BIRGIT SCHENKEL
Dipl. Phys. (University of Heidelberg, Germany)
born on March 15, 1976
citizen of Germany

accepted on the recommendation of
Prof. Dr. U. Keller, Supervisor
Prof. Dr. M. Nisoli, Co-Examiner
Dr. J. Biegert, Co-Examiner

June, 2004

Table of Contents

List of Abbreviations and Physical Symbols	IV
Abstract	VIII
Kurzfassung	X
Introduction	1
Generation of Supercontinua	5
2.1 Nonlinear Pulse Propagation in Optical Fibers	6
2.1.1 Fiber nonlinearities.....	6
2.1.2 Advantages of optical fibers over bulk	9
2.1.3 Basic propagation equation	11
2.2 Supercontinuum Generation in Hollow Fibers	15
2.2.1 Spectral broadening mechanisms in hollow fibers.....	15
2.3 Supercontinuum Generation in Microstructure Fibers.....	17
2.3.1 Special properties of microstructure fibers	17
2.3.2 Spectral broadening mechanisms in microstructure fibers	19
Compression of Supercontinua	27
3.1 Different Compression Techniques	28
3.1.1 Classical techniques	28
3.1.1.1 Gires-Tournois Interferometer (GTI).....	28
3.1.1.2 Prism-pair.....	29
3.1.1.3 Grating-pair.....	30
3.1.1.4 Fiber-grating-compressor.....	31
3.1.2 Chirped mirrors	32
3.2 Pulse Shaping Techniques: Deformable Mirrors and Spatial Light Modulators ..	34
3.2.1 Femtosecond pulse shaping basics	35
3.2.1.1 Linear filtering	35
3.2.1.2 Pulse shaping apparatus.....	37
3.2.2 Deformable mirrors	38
3.2.3 Liquid crystal spatial light modulators.....	39

3.3	Compressor Resolution	41
3.4	Broadband Pulse Characterization	42
3.4.1	Spectral phase interferometry for direct electric-field reconstruction (SPIDER)	43
3.4.2	Implementation of a broadband SPIDER setup	44
3.5	Adaptive Compression	47
Hollow-Fiber Experiments		49
4.1	Motivation and Overview	49
4.2	Experimental Setup	51
4.2.1	Continuum generation	51
4.2.2	Pulse shaper	52
4.2.3	Pulse characterization and compression	53
4.3	Results	53
4.4	Error Estimations	60
Microstructure-Fiber Experiments		63
5.1	Experimental Setup	64
5.1.1	Supercontinuum generation	64
5.1.2	Pulse shaper	67
5.1.3	Pulse characterization and compression	67
5.2	Experimental Results	68
5.2.1	Microstructure fiber with 2.6 μm core diameter	68
5.2.2	Microstructure fiber with 1.7 μm core diameter	70
5.3	Theoretical Considerations	72
5.3.1	Simulation basics	73
5.3.2	Calculation of coherence	74
5.3.3	Results for 2.6 μm core diameter fiber and comparison with experiment	75
5.3.4	Results for 1.7 μm core diameter fiber and comparison with experiment	78
5.4	Discussion	80
5.4.1	Coherence degradation due to power fluctuations	80
5.4.2	Cladding modes due to short fibers	82
5.4.3	SPIDER problem for structured spectra	83
5.5	Conclusions	83

Conclusion and Outlook	85
References	89
Curriculum Vitae	97

List of Abbreviations and Physical Symbols

α	Fiber loss
β	Mode propagation constant
γ	Nonlinearity coefficient
$\delta(t)$	Delta function
ε	Dielectric constant
ε_0	Vacuum permittivity
λ	Wavelength
μ_0	Vacuum permeability
$\Delta\nu_B$	Brillouin-gain bandwidth
$\Delta\nu_P$	Pump bandwidth
$\delta\phi$	Phase change per pixel
ϕ	Phase-shift
ϕ_{NL}	Nonlinear phase-shift
χ	Susceptibility
$\chi^{(1)}$	Linear dielectric susceptibility
$\chi^{(2)}$	Second order nonlinear susceptibility
$\chi^{(3)}$	Third order nonlinear susceptibility
ω	Angular frequency
ω_0	Carrier frequency
$\Delta\omega$	Spectral width
$\Delta\omega_P$	Frequency-bandwidth covered by one pixel
a	Capillary radius
A_{eff}	Effective core area
Ar	Argon
AR	Anti-reflection
BASIC	Back-side coated
BBO	β -barium-borate
c	Speed of light in vacuum
c_n	Speed of light in a dielectric material
CCD	Charge-coupled device
CEO	Carrier-envelope offset
CPA	Chirped pulse amplification
cw	continuous wave
d	Thickness of a GTI

DCM	Double chirped mirror
E	Electric field
$e_{in}(t)$	Input pulse
$e_{out}(t)$	Output pulse
$E_{in}(\omega)$	Input spectrum
$E_{out}(\omega)$	Output spectrum
f_R	Fractional contribution of the delayed Raman response
FROG	Frequency resolved optical gating
FWHM	Full width at half maximum
FWM	Four-wave mixing
g_B	Brillouin-gain coefficient
g_R	Raman-gain coefficient
GD	Group delay
GDD	Group-delay dispersion
GTI	Gires-Tournois Interferometer
GVD	Group-velocity dispersion
$h(t)$	Impulse response function
$H(\omega)$	Frequency response function
$h_R(t)$	Raman response function
HHG	Higher-order harmonic generation
I	Optical intensity
I_0	Peak intensity
I_p	Pump intensity
I_p^{th}	Threshold pump intensity
I_S	Stokes intensity
IAC	Interferometric Autocorrelation
J_0	Zero-order Bessel function
k	Wavenumber
KLM	Kerr-lens-modelocking
L	Fiber length
L_D	Dispersion length
L_{eff}	Effective interaction length
L_{NL}	Nonlinear length
L_{opt}	Optimum fiber length
m	Order of diffraction
n	Refractive index
n_2	Nonlinear-index coefficient
P	Polarization
P_L	Linear polarization
P_{NL}	Nonlinear polarization
P	Optical power
r	Radial coordinate
$R(t)$	Nonlinear response function
rms	Root-mean-square
S	Distance between two prisms

SBS	Stimulated Brillouin scattering
SFG	Sum-frequency generation
SHG	Second-harmonic generation
SPIDER	Spectral phase interferometry for direct electric-field reconstruction
SPM	Self-phase modulation
SRS	Stimulated Raman scattering
t	Time
T_0	Pulse half-width (at the 1/e-intensity point)
THG	Third-harmonic generation
w_0	Spot size
XPM	Cross-phase modulation
z	Spatial coordinate along beam direction
z_0	Rayleigh-range
ZDW	Zero dispersion wavelength
θ_i	Angle of incidence
θ_m	Angle of diffraction
θ_0	Beam crossing angle

Abstract

In recent years, the generation of supercontinua has become possible by a variety of different techniques. Especially two methods allowing for the generation of spectra spanning more than an optical octave found widespread use, namely, supercontinuum generation using hollow fibers and microstructure fibers. A number of fundamental experiments, ranging from the production of single attosecond pulses via high-order harmonic generation (HHG) to the investigation of various nonlinear processes in which the absolute phase plays an important role, rely on the generation of high-peak-power light pulses in the single-cycle regime. Therefore, the desire arose to compress the enormous bandwidths of the generated supercontinua to yield a single-cycle optical pulse.

In this thesis, the generation and compression of supercontinua using the above mentioned techniques for their production is studied experimentally. Adaptive pulse compression is achieved by using the spectral phase obtained from a spectral phase interferometry for direct electric field reconstruction (SPIDER) measurement as feedback for a liquid crystal spatial light modulator (SLM). In addition, numerical simulations on the compressibility of microstructure fiber generated supercontinua are presented.

The generation of supercontinua in hollow-core fibers calls for input pulses with mJ pulse energies at a repetition rate of typically 1 kHz. The spectral phase of these supercontinua is found to be extremely stable over several hours. This allowed us to demonstrate successful compression to pulses as short as 3.8 fs with a pulse energy of 15 μ J. These pulse are among the shortest pulses ever generated in the visible and near-

infrared spectral region. Compared to other pulses with similar durations these pulses provide more than an order of magnitude higher pulse energies.

Using microstructure fibers for supercontinuum generation is already possible with nanojoule pulse energies at the full oscillator repetition rate. We investigate supercontinuum generation and compression in two different fibers, pumping in the normal and anomalous dispersion regime, respectively. Pumping in the normal dispersion regime allowed for the compression of the generated bandwidths to 5.5 fs pulses. On the other hand, compression could not be demonstrated for the broader supercontinua generated in the anomalous dispersion regime.

We have performed numerical simulations of pulse propagation in both fibers, including a calculation of the coherence of the generated supercontinua and taking into account that the compressor has only a limited resolution. These simulations suggest that pumping in the normal dispersion regime should lead to the production of compressible spectra. This is in excellent agreement with our experimentally obtained results. Pumping in the anomalous dispersion regime leads to a significant coherence degradation and due to the broader spectra the finite compressor resolution starts to play a role. Nonetheless, the simulation predicts that compression to sub-2-fs pulses should still be possible, however only with a poor pulse quality. The fact that we were not able to compress these supercontinua at all is probably due to a limitation of the SPIDER-technique. The spectra generated in the anomalous dispersion regime exhibited strong spectral features, which were directly imposed onto the SPIDER-signal. As a consequence, the fringe visibility was destroyed rendering a correct reconstruction of the spectral phase impossible.

In conclusion, we have successfully demonstrated the compression of both a hollow fiber supercontinuum and a microstructure fiber supercontinuum generated in the normal dispersion regime to pulse durations never achieved before with these techniques. Following our numerical simulations, we believe that a clean compression of the supercontinua generated in the anomalous dispersion regime using today's state-of-the-art pulse compressors is not possible.

Kurzfassung

Die Erzeugung von Superkontinua konnte in den letzten Jahren mit Hilfe verschiedener Techniken demonstriert werden. Besonders zwei Methoden, die die Erzeugung von Spektren über mehr als eine optische Oktave ermöglichen, haben verbreitet Einsatz gefunden. Dies sind die Superkontinuumserzeugung in Hohlfasern und in Mikrostrukturfasern. Einige Grundlagenexperimente, wie z. B. die Produktion von einzelnen Attosekundenpulsen durch die Erzeugung höherer Harmonischer oder die Untersuchung verschiedener nichtlinearer Prozesse, bei denen die absolute Phase eine wichtige Rolle spielt, sind von der Erzeugung von Lichtpulsen mit hoher Spitzenleistung und einer Pulsdauer im Einzyklenbereich abhängig. Daraus entstand der Wunsch die riesigen Bandbreiten der erzeugten Superkontinua zu einem Puls mit nur einem optischen Zyklus zu komprimieren.

Im Rahmen dieser Dissertation wurde die Erzeugung und Kompression von Superkontinua mit Hilfe der oben genannten Methoden und einem adaptiven Pulskompressionsverfahren experimentell untersucht, das auf der Messung der spektralen Phase mittels eines “spectral phase interferometry for direct electric field reconstruction” (SPIDER) Aufbaus basiert, welche dann als Feedback für einen Modulator mit Flüssigkristallmaske (SLM) benutzt wird. Ausserdem wurden numerische Simulationen zur Kompressibilität der in Mikrostrukturfasern erzeugten Superkontinua durchgeführt.

Für die Superkontinuumserzeugung in Hohlfasern werden Eingangspulse mit einer Pulsenergie im mJ-Bereich bei Repetitionsraten von typischerweise 1 kHz benötigt. Es zeigt sich, dass die spektrale Phase dieser Superkontinua über mehrere Stunden

hinweg extrem stabil ist. Dies ermöglichte uns eine erfolgreiche Kompression zu einer Pulsdauer von nur 3.8 fs mit einer Pulsenergie von 15 μ J. Diese Pulse gehören zu den kürzesten, die jemals im sichtbaren und nahen infraroten Spektralbereich erzeugt worden sind. Verglichen mit anderen Pulsen mit ähnlicher Pulsdauer haben diese Pulse eine um mehr als eine Grössenordnung höhere Pulsenergie.

Mit Hilfe von Mikrostrukturfasern ist die Superkontinuumserzeugung bereits mit Pulsenergien im nJ-Bereich bei der vollen Repetitionsrate eines Oszillators möglich. Wir untersuchen die Superkontinuumserzeugung und Kompression mit zwei verschiedenen Fasern. Eine wird im normalen Dispersionsbereich, die andere im anomalen Dispersionsbereich gepumpt. Wenn wir im normalen Dispersionsbereich pumpen, konnten wir die Kompression dieser Bandbreiten zu 5.5 fs langen Pulsen demonstrieren. Allerdings gelang uns keine Kompression der breiteren, im anomalen Dispersionregime erzeugten Superkontinua.

Wir haben numerische Simulationen zur Propagation von Lichtpulsen durch beide Fasern durchgeführt, einschliesslich einer Berechnung der Kohärenz der Superkontinua und unter Berücksichtigung der Tatsache, dass der Kompressor nur eine limitierte Auflösung besitzt. Diese Simulationen legen nahe, dass eine Kompression der im normalen Dispersionsregime erzeugten Spektren möglich sein sollte, was perfekt mit unserem experimentell erhaltenen Result übereinstimmt. Dagegen führt Pumpen im anomalen Dispersionsbereich zu einer signifikanten Verschlechterung der Kohärenz. Ausserdem beginnt hier die limitierte Auflösung des Kompressors eine Rolle zu spielen, da die erzeugten Spektren breiter sind. Trotzdem sollte laut Simulation eine Kompression zu Pulsen, die kürzer als 2 fs sind, noch möglich sein, wenn auch nur mit schlechter Pulsqualität. Vermutlich ist eine Limitation der SPIDER-Technik der Grund dafür, dass wir diese Superkontinua überhaupt nicht komprimieren konnten. Die im anomalen Dispersionsbereich erzeugten Superkontinua zeigen starke spektrale Strukturen, welche auch im SPIDER-Signal sichtbar sind. Dies zerstört das Interferenzmuster, was eine korrekte Rekonstruktion der spektralen Phase unmöglich macht.

In dieser Arbeit wurde die erfolgreiche Kompression sowohl eines Hohlfasers als auch eines Mikrostrukturfaser-Superkontinuums zu Pulsdauern demonstriert, wie sie vorher mit diesen Methoden nie erreicht worden sind. Aus unseren Simulationen schliessen wir, dass eine saubere Kompression der im anomalen Dispersionsbereich erzeugten Superkontinua mit heute verfügbaren Pulskompressoren nicht möglich ist.

Chapter 1

Introduction

At the beginning of mankind, God set his rainbow in the sky as a sign of the everlasting covenant between himself and all living creatures of every kind on the earth [1]. Since then the rainbow has preserved the fascination that emanates from it. With the invention of the electric bulb in the nineteenth century, white light, spanning the whole spectral range of a rainbow, found its way into almost every house. Although this light is extremely useful in our everyday lives, it has the disadvantage of not being coherent.

Many applications would benefit from a coherent white-light source. Therefore, in the past decades research groups tried to develop such white-light sources, spanning the whole spectral range of a rainbow from violet over blue, green, yellow and orange to the red and near-infrared. The process used to generate these white-light sources is called supercontinuum generation and is a complex nonlinear phenomenon that is characterized by the dramatic spectral broadening of intense light pulses passing a nonlinear material [2].

The first observation of supercontinuum generation producing a 200-THz-wide continuum in bulk glass was reported in 1970 [3, 4]. Since then, supercontinuum generation has been successfully demonstrated in a wide variety of nonlinear media including solids [3, 4, 5], organic and inorganic liquids [6, 7, 8, 9], gases [10, 11, 12], and different types of waveguide structures such as silica optical fibers [13, 14] and hollow optical waveguides [15].

These supercontinua have found applications in time-resolved absorption and excitation spectroscopy, in which the high-brightness and wide frequency band of the

the supercontinua have permitted single-shot recording of broad spectra [2]. Subsequently, the exploitation of supercontinuum generation in pulse compression techniques has led to the design of sources of coherent optical femtosecond pulses [2, 15, 16, 17].

These “first generation” supercontinua had in common, that they did not span one optical octave. The generation of supercontinua spanning more than one optical octave has become possible only in the last decade. With the invention of microstructure fibers in the late 1990s, supercontinua over two optical octaves have been demonstrated [18]. Supercontinuum generation over more than one optical octave has as well been achieved with an improved version of the hollow-fiber technique using either a single or two cascaded hollow fibers [19, 20].

As a result of these research efforts, it has recently become possible to measure and control the carrier-envelope offset (CEO) phase of femtosecond pulses [21]. This has led to dramatic advances in optical frequency metrology, enabling absolute measurements of optical frequencies with unprecedented accuracy [21, 22, 23, 24]. Therefore, supercontinuum generation could be the key to direct optical frequency and optical waveform synthesis and to the development of a new frequency standard based on an all-optical clock.

Other applications rely on the generation of ultrashort pulses in the single-cycle regime. Such applications include the study of nonlinear processes, in which the absolute phase plays a relevant role [25], and - in combination with a stabilized CEO-phase - the generation of single attosecond pulses via higher-order harmonic generation (HHG) [26]. To produce such pulses, a coherent supercontinuum spanning approximately one optical octave in the visible spectral region has to be properly compressed.

Until now, the supercontinuum output of a single hollow fiber has been compressed to 4.5 fs using a combination of chirped mirrors and thin prisms [27]. Pulses with a duration of 5 fs were obtained with the same technique by using either only chirped mirrors [28] or a sole spatial light modulator (SLM) [29] for dispersion compensation. Generation of 4.5-fs pulses was achieved from a fiber-compressed output of a cavity-dumped Ti:sapphire laser [30]. Using noncollinear optical amplification, pulses as short as 4 fs with an energy of 0.5 μ J were generated. In this case a dispersive delay line consisting of chirped mirrors, gratings, and a programmable deformable mirror was used for compression [31].

In this thesis, we study the generation and compression of octave spanning supercontinua using two methods for their production: Supercontinuum generation in cascaded hollow fibers using amplified pulses at kHz repetition rates and in two different microstructure fibers using nanojoule pulses directly from a Ti:sapphire oscillator. For pulse compression, we use in both cases a state-of-the-art liquid crystal SLM with 640 pixels. Compression of these ultrabroadband spectra was performed in an iterative procedure.

In Chapter 2, we start with an introduction to nonlinear pulse propagation in optical fibers. The fundamental fiber nonlinearities are explained and the propagation equation for ultrashort pulses is derived. Then, the particular spectral broadening mechanisms in hollow-core fibers and microstructure fibers are explained in more detail. For microstructure fibers, it has to be differentiated mainly between two pumping regimes: normal and anomalous dispersion pumping. Continuum generation mechanisms in these regimes will be discussed.

A broad variety of pulse compression techniques exists. In Chapter 3, we introduce the classical dispersion compensation methods such as Gires-Tournois Interferometers (GTI), prism and grating compressors. These techniques however are not applicable to ultrabroadband pulse compression because of their limited bandwidth. A new variant of chirped mirrors, the back-side-coated (BASIC) mirrors offers a large bandwidth, but has the disadvantage of not being flexible. This drawback is overcome with adaptive pulse shaping using deformable mirrors and in particular SLMs as is explained in this Chapter in more detail. Successful pulse compression is closely linked to correct pulse characterization. Thus, in this Chapter, we also discuss the particular implementation of our spectral phase interferometry for direct electric-field reconstruction (SPIDER) setup optimized for pulses with more than octave spanning spectra. The Chapter ends with a description of the optimization procedure used in our compression experiments, which relied on a direct feedback from the measured spectral phase to the pulse shaper.

Our experiments with cascaded hollow fibers are presented in Chapter 4. These experiments resulted in successful compression to 3.8 fs pulses with a pulse energy of 15 μ J. These pulses are among the shortest pulses ever generated in the visible to near-infrared spectral region. Compared to other similarly short pulses the pulse energy is more than an order of magnitude higher. Due to the subtleties involved in characterizing

such ultrashort pulses, we conclude the Chapter with a thorough estimation of measurement errors.

In Chapter 5, we present our experiments using microstructure fibers for supercontinuum generation. We show that pumping in the normal dispersion regime leads to a relatively stable continuum. In this case, we were able to demonstrate successful compression to a pulse duration of 5.5 fs. To the best of our knowledge, this is the shortest pulse ever generated using microstructure fibers. Pumping in the anomalous dispersion regime allowed for the generation of a much broader but heavily structured spectrum. Here, compression failed due to a combination of several factors such as coherence degradation due to power fluctuations, the finite compressor resolution, and a limitation of the SPIDER-technique for strongly structured spectra. To study the influence of these effects, we performed numerical simulations of pulse propagation through both available fibers including the effects of coherence degradation and the limited compressor resolution. Our simulations predict excellent compressibility in the normal dispersion regime. This is in good agreement with our experimental result. In the anomalous dispersion regime however, a bigger coherence degradation is observed and due to the broader spectra, the compressor resolution starts to play a role. Nonetheless, the simulation predicts that pulse compression should still be possible, but only with a reduced pulse quality.

In Chapter 6, we will draw the conclusions on the work presented in this thesis and provide a short outlook on the future development of ultrashort pulse compression.

Chapter 2

Generation of Supercontinua

The first supercontinuum generation experiments were based on focusing short, intense optical pulses into bulk materials exhibiting a $\chi^{(3)}$ nonlinearity. In those experiments the primary mechanism that led to spectral broadening was self-phase-modulation (SPM) [4, 5, 9]. The main problem these experiments had in practice, was that due to the tight focusing necessary to reach high enough intensities the interaction length was limited. In addition, if the intensities are too high multiphoton ionization occurs, which leads to damage and destroys the spatial beam quality. Therefore, the second-generation experiments on supercontinuum generation were based on silica optical waveguides. Optical fibers allow high optical intensities to be maintained over long lengths, thereby enhancing the nonlinear effects. This high effective nonlinearity of optical fibers has led to a dramatic reduction in the pump power requirements compared with those for bulk media. In these early fiber experiments the supercontinuum resulted from the direct generation of new spectral components through cascaded stimulated Raman scattering (SRS) and four-wave mixing (FWM) and from a further broadening and merging of these frequency components [13, 14]. The role of SPM was limited because the pump pulses were relatively long (10 ps – 10 ns). The latest step in the development of supercontinuum sources is the generation of supercontinua covering the whole visible spectral range, which became possible with the advent of femtosecond pump pulses. There exist several techniques with which such supercontinua can be produced, e.g. by focusing high energy pulses into gases or liquids, or by using an optical parametric amplifier [31] or by producing the continuum in different fibers. In this Chapter we will discuss the two techniques used in our experiments in more detail. These are launching amplified pulses at a reduced repetition rate into gas-filled hollow fibers [15, 20], and seeding

the recently developed photonic crystal fibers (PCF) or microstructure fibers with low energy pulses at the full oscillator repetition rate [18, 32].

In this Chapter, the basic mechanisms of supercontinuum generation will be introduced and a mathematical description of nonlinear pulse propagation is given. First, an overview of the nonlinear phenomena in optical fibers is presented and in order to understand these phenomena we shortly discuss the theory of electromagnetic wave propagation in dispersive nonlinear media. From this we derive a basic propagation equation for optical pulses in single-mode fibers.

Depending on the fiber type, different nonlinear mechanisms dominate the spectral broadening process. In gas-filled hollow fibers supercontinuum generation is governed mainly by one process, namely self-phase modulation (SPM). Whereas in the recently developed PCFs or microstructured fibers spectral broadening results from a complicated interplay of different nonlinear mechanisms. This interplay is not yet fully understood and there is continuing research going on in this field. We will explain the differences in supercontinuum generation between hollow and microstructured fibers in more detail later in this Chapter.

2.1 Nonlinear Pulse Propagation in Optical Fibers

This section follows very closely the book of G. P. Agrawal [33]. For simplicity, we begin this Chapter with a description of the nonlinear effects in fibers for continuous wave (cw) laser beams. It is straightforward to transfer these mechanisms to pulsed laser sources. The derivation of the basic propagation equation in Subsection 2.1.3 is then given for pulsed laser beams.

2.1.1 Fiber nonlinearities

As in any other dielectric the response to light becomes nonlinear in optical fibers for intense electromagnetic fields. The origin of this nonlinear response is related to anharmonic motion of bound electrons under the influence of an applied field. Therefore, the induced polarization P from the electric dipoles is not linear in the electric field E anymore, but satisfies the relation [34]

$$P = \varepsilon_0 [\chi^{(1)}E + \chi^{(2)}E^2 + \chi^{(3)}E^3 + \dots], \quad (2.1)$$

where ε_0 is the vacuum permittivity and $\chi^{(i)}$ ($i = 1, 2, \dots$) is the i -th order susceptibility. Here, the linear susceptibility $\chi^{(1)}$ is the dominant contribution to P . The second-order susceptibility $\chi^{(2)}$ is responsible for processes such as second-harmonic generation (SHG) and sum-frequency generation (SFG) [34]. However, it is zero for media exhibiting an inversion symmetry at the molecular level. Therefore, $\chi^{(2)}$ vanishes for silica glasses since SiO_2 is isotropic. As a result, optical fibers do not normally show second-order nonlinear effects.

This is the reason why the lowest order nonlinear effects in optical fibers originate from the third-order susceptibility $\chi^{(3)}$, which is responsible for phenomena such as third-harmonic generation (THG), four-wave mixing (FWM), and nonlinear refraction [34]. However, the processes which involve the generation of new frequencies like THG and FWM (nonlinear refraction does not generate new frequencies for cw laser beams) are not efficient in optical fibers unless special efforts are made to achieve phase matching (this is the matching of fundamental and signal phase velocities). Therefore, most of the nonlinear effects in optical fibers originate from nonlinear refraction. This phenomenon corresponds to an intensity dependence of the refractive index resulting from the contribution of $\chi^{(3)}$. That means, the refractive index becomes

$$\tilde{n}(\omega, I) = n(\omega) + n_2 I, \quad (2.2)$$

where $n(\omega)$ is the linear refractive index, I is the optical intensity inside the fiber and n_2 is the nonlinear-index coefficient. Strictly speaking, n_2 is also dependent on ω , but is assumed to be constant in the following discussions.

The higher-order susceptibilities $\chi^{(4)}$, $\chi^{(5)}$, ... in Equation (2.1) can be neglected since all even-order susceptibilities are zero for silica fibers like $\chi^{(2)}$, and $\chi^{(5)}$ is the susceptibility corresponding to the contribution of E^5 to the polarization P .

The intensity dependence of the refractive index leads to a large number of interesting nonlinear effects. The two most widely studied are SPM and cross-phase modulation (XPM). SPM refers to the self-induced phase shift experienced by an optical field during its propagation in optical fibers. Its magnitude can be obtained by noting that the phase of an optical field changes by

$$\phi = (n + n_2 I) \cdot kL, \quad (2.3)$$

where $k = 2\pi/\lambda$ and L is the fiber length. The intensity-dependent nonlinear phase shift $\phi_{NL} = n_2 kLI$ is due to the nonlinear refraction. This process generates new frequencies for pulsed laser light, because the intensity becomes time-dependent. In this case, SPM broadens the bandwidth of the pulses, because the frequency is given by

$$\omega(t) = -\frac{d\phi_{NL}(t)}{dt} = -n_2 kL \frac{dI(t)}{dt}. \quad (2.4)$$

For a bandwidth-limited pulse SPM generates in the leading part of the pulse (meaning $dI(t)/dt > 0$) a decrease in frequency ($\omega(t) < 0$) and in the trailing part of the pulse ($dI(t)/dt < 0$) an increase in frequency ($\omega(t) > 0$). Among other things, SPM is responsible for spectral broadening of ultrashort pulses [35] and the existence of optical solitons in the anomalous-dispersion regime of fibers [36].

XPM refers to the nonlinear phase shift of an optical field induced by a second field at a different wavelength. Due to the fact that we never have two different fields in our experiments, the effect of XPM does not occur and we will therefore not explain it further.

The nonlinear effects governed by the third-order susceptibility are elastic in the sense that no energy is exchanged between the electromagnetic field and the dielectric medium. A second class of nonlinear effects results from stimulated inelastic scattering in which the optical field transfers part of its energy to the nonlinear medium. Two important nonlinear effects in optical fibers fall into this category. Both of them are related to vibrational excitation modes of silica. These phenomena are known as stimulated Raman scattering (SRS) and stimulated Brillouin scattering (SBS) [37, 38]. The main difference between the two is that optical phonons participate in SRS while acoustic phonons participate in SBS. In a simple quantum-mechanical picture applicable to both SRS and SBS, a photon of the incident field (the pump) is annihilated to create a photon at the downshifted Stokes frequency and a phonon with the right energy and momentum to conserve the energy and the momentum. Of course, a higher-energy photon at the so-called anti-Stokes frequency can also be created via the inverse process if a phonon of right energy and momentum is available. The generation of an anti-Stokes photon is achieved via FWM, where two pump photons annihilate themselves to

produce Stokes and anti-Stokes photons provided the total momentum is conserved. The momentum-conservation requirement leads to a phase-matching condition, that must be satisfied for FWM to take place. This phase-matching condition is not easily satisfied in single-mode fibers, thus the anti-Stokes wave is rarely observed during SRS. Even though SRS and SBS are very similar in their origin, different dispersion relations for acoustic and optical phonons lead to some basic differences between the two. A fundamental difference is that SBS in optical fibers occurs only in the backward direction whereas SRS dominates in the forward direction.

Although a complete description of SRS and SBS in optical fibers is quite involved, the initial growth of the Stokes wave can be described by a simple relation. For SRS, this relation is given by

$$\frac{dI_S}{dz} = g_R I_p I_S, \quad (2.5)$$

where I_S is the Stokes intensity, I_p the pump intensity, and g_R the Raman-gain coefficient. The growth of the anti-Stokes wave is not discussed here, because as we have seen above its contribution is negligible. A similar relation holds for SBS with g_R replaced by the Brillouin-gain coefficient g_B . The Raman-gain spectrum is measured to be very broad extending up to ~ 30 THz [37]. By contrast, the Brillouin-gain spectrum is extremely narrow with a bandwidth of only ~ 10 MHz [38]. The peak value of Brillouin-gain decreases by a factor of $\Delta\nu_p/\Delta\nu_B$ for a broad-bandwidth pump, where $\Delta\nu_p$ is the pump bandwidth and $\Delta\nu_B$ is the Brillouin-gain bandwidth. Therefore SBS is negligible for pump pulses shorter than approximately 50 ns with a broad spectrum.

An important feature of SRS and SBS is that they exhibit a threshold-like behavior, which means that significant conversion of pump energy to Stokes energy occurs only when the pump intensity exceeds a certain threshold level. For SRS the threshold pump intensity typically is $I_p^{th} \sim 10 \text{ MW/cm}^2$.

2.1.2 Advantages of optical fibers over bulk

Recent measurements of the nonlinear-index coefficient n_2 in silica fibers yield a value in the range $2.2\text{-}3.4 \cdot 10^{-20} \text{ m}^2/\text{W}$ depending on the core composition and on whether the input polarization is preserved inside the fiber or not. This value is small compared to

most other nonlinear media by at least two orders of magnitude. But in spite of these intrinsically small values of the nonlinearity coefficients in fused silica, the nonlinear effects in optical fibers can be observed at relatively low power levels. This is possible because of two important characteristics of single-mode fibers: A small spot size ($\sim 2 - 4 \mu\text{m}$) and extremely low loss ($\leq 1 \text{ dB/km}$).

A figure of merit for the efficiency of a nonlinear process in bulk media is the product IL_{eff} , where I is the optical intensity and L_{eff} is the effective length of interaction [39]. If light is focused to a spot of radius w_0 , then $I = P/\pi w_0^2$, where P is the incident optical power. Clearly, I can be increased by focusing the light tightly to reduce w_0 . However, this results in a smaller L_{eff} since the length of the focal region decreases with tight focusing. For a Gaussian beam, $L_{\text{eff}} \cong \pi w_0/\lambda$ (corresponds to Rayleigh-range), and the product

$$IL_{\text{eff}} = \frac{P}{\pi w_0^2} \frac{\pi w_0^2}{\lambda} = \frac{P}{\lambda} \quad (2.6)$$

is independent of the spot size w_0 .

In contrast, the situation in fibers is the following: because of dielectric waveguiding, the same spot size can be maintained along the entire fiber length L . In this case the interaction length is limited by the fiber loss α . Using $I(z) = I_0 \exp(-\alpha z)$, where $I_0 = P/\pi w_0^2$ and P is the optical power coupled into the fiber, the product IL_{eff} becomes

$$IL_{\text{eff}} = \int_0^L \frac{P}{\pi w_0^2} e^{-\alpha z} dz = \frac{P}{\pi w_0^2} \left(\frac{1 - e^{-\alpha L}}{\alpha} \right). \quad (2.7)$$

A comparison of Equations 2.6 and 2.7 shows that the efficiency of the nonlinear process in optical fibers can be improved by a factor [39]

$$\frac{(IL_{\text{eff}})_{\text{fiber}}}{(IL_{\text{eff}})_{\text{bulk}}} = \frac{\lambda}{\pi w_0^2 \alpha}, \quad (2.8)$$

where $\alpha L \gg 1$ was assumed. In the visible region, for $\lambda = 0.53 \mu\text{m}$, $w_0 = 2 \mu\text{m}$, and $\alpha = 2.5 \cdot 10^{-5} \text{ cm}^{-1}$ (10 dB/km), the enhancement factor is $\sim 10^7$. It is this tremendous enhancement in the efficiency of the nonlinear processes that makes silica fibers a suit-

able nonlinear medium for the observation of a wide variety of nonlinear effects at relatively low power levels.

As will be discussed in Chapter 5, when using a microstructured fiber for supercontinuum generation only very short pieces of fiber (2 - 5 mm) are used in our experiments for dispersion management reasons. Here, the question might arise, why still use such short fibers, but not bulk? The effective interaction length of a 2 mm piece of fiber with a core diameter of 1.7 μm is 2 mm. But the effective interaction length in bulk when focusing to the “same” spot size ($w_0 = 0.85 \mu\text{m}$) is the Rayleigh-range $z_0 = \pi w_0^2 / \lambda$. With $\lambda = 0.53 \mu\text{m}$, we retrieve for the Rayleigh-range a value of $z_0 = 4.3 \mu\text{m}$, which is much smaller than the effective interaction length even in very short pieces of fiber.

As already mentioned, another advantage of fibers over bulk is the higher threshold for multiphoton ionization. In bulk, tight focusing is necessary to achieve high enough intensities. These are easily above the threshold for multiphoton ionization, thus causing damage and the generation of a filament, which destroys the spatial properties of the beam.

2.1.3 Basic propagation equation

The study of most nonlinear effects in optical fibers involves the use of short pulses with widths ranging from ~ 10 ns to ~ 10 fs, because of the high peak intensities which can be achieved with them. When such optical pulses propagate inside the fiber, both dispersive and nonlinear effects influence their shape and spectrum. In this subsection we derive a basic equation that governs the propagation of optical pulses in nonlinear dispersive fibers.

The starting point is the wave equation that describes light propagation in optical fibers obtained by using Maxwell's equations. If we include only the third-order nonlinear effects governed by $\chi^{(3)}$, the induced polarization consists of two parts

$$P(r, t) = P_L(r, t) + P_{NL}(r, t), \quad (2.9)$$

such that the wave equation can be written in the form

$$\nabla^2 E - \frac{1}{c^2} \frac{\partial^2 E}{\partial t^2} = \mu_0 \frac{\partial^2 P_L}{\partial t^2} + \mu_0 \frac{\partial^2 P_{NL}}{\partial t^2}, \quad (2.10)$$

where c is the speed of light in vacuum, μ_0 is the vacuum permeability and P_L and P_{NL} are the linear and nonlinear induced polarizations respectively.

It is necessary to make several simplifying assumptions in order to solve Equation 2.10. First, P_{NL} is treated as a small perturbation to P_L . Second, the optical field is assumed to maintain its polarization along the fiber length so that a scalar approach is valid. Third, the slowly varying envelope approximation is used, that means, the optical field is assumed to be quasi-monochromatic, *i.e.* its spectrum, centered at ω_0 , has a spectral width $\Delta\omega$ such that $\Delta\omega/\omega_0 \ll 1$. Numerical simulations show that this approximation still holds very well even for few-cycle pulses.

Further considerable simplification occurs if the nonlinear response is assumed to be instantaneous, which corresponds to neglecting the contribution of molecular vibrations to $\chi^{(3)}$ (the Raman effect). In general, both electrons and nuclei respond to the optical field in a nonlinear manner. The nuclei response is inherently slower compared with the electronic response. For silica fibers the vibrational or Raman response occurs over a time scale 60-70 fs. Thus, the assumption of instantaneous nonlinear response is approximately valid for pulse durations > 1 ps.

Before solving Equation 2.10 we introduce the mode propagation constant $\beta(\omega)$ and expand it in a Taylor series about the carrier frequency ω_0 , *i.e.*,

$$\beta(\omega) = n(\omega) \frac{\omega}{c} = \beta_0 + (\omega - \omega_0) \beta_1 + \frac{1}{2} (\omega - \omega_0)^2 \beta_2 + \frac{1}{6} (\omega - \omega_0)^3 \beta_3 + \dots, \quad (2.11)$$

where

$$\beta_n = \left(\frac{d^n \beta}{d\omega^n} \right)_{\omega=\omega_0}. \quad (2.12)$$

For pulse durations > 0.1 ps the cubic and higher-order terms in this expansion are generally negligible. Thus, with these simplifications the result is

$$\frac{\partial A(z,t)}{\partial z} + \beta_1 \frac{\partial A}{\partial t} + \frac{i}{2} \beta_2 \frac{\partial^2 A}{\partial t^2} + \frac{\alpha}{2} A = i\gamma |A(z,t)|^2 A(z,t), \quad (2.13)$$

where the nonlinearity coefficient is defined by

$$\gamma = \frac{n_2 \omega_0}{c A_{eff}}, \quad (2.14)$$

where the parameter A_{eff} is known as the effective core area. $A(z,t)$ is the slowly varying envelope of the electric field $E(z,t)$ given by

$$A(z,t) = \frac{1}{2} \sqrt{c_n} \sqrt{\varepsilon \varepsilon_0} E(z,t) e^{i(\omega_0 t - \beta_n(\omega_0)z)},$$

where c_n is the velocity of light in a dielectric material, ε is the dielectric constant and ε_0 is the vacuum permittivity. In obtaining Equation 2.13 the pulse amplitude A is normalized such that $|A|^2$ represents the optical intensity.

Equation 2.13 describes the propagation of an optical pulse in single-mode fibers. It is sometimes referred to as the nonlinear Schrödinger equation since it can be reduced to that equation under certain conditions. It includes the effects of fiber loss through α , of chromatic dispersion through β_1 (the group delay) and β_2 (the group delay dispersion (GDD)), and of the fiber nonlinearity through γ .

Since we have made several assumptions in the derivation of Equation 2.13 that are not valid for ultrashort pulses, this equation has to be modified for pulses shorter than 100 fs. First, higher-order dispersion terms have to be included for ultrashort pulses [40]. Second, the spectrum of such short pulses is wide enough (> 1 THz) that the Raman gain can amplify their low-frequency components by transferring energy from the high-frequency components of the same pulse. This effect is sometimes called intrapulse Raman scattering. As a result of intrapulse Raman scattering, the pulse spectrum shifts toward the red side as the pulse propagates inside the fiber, a phenomenon referred to as the self-frequency shift [41]. The physical origin of this effect is related to the retarded nature of nonlinear response [42]. Thus, the delayed nonlinear response has to be included as well. The last additional contribution results from including the first derivative of the slowly varying part P_{NL} of the nonlinear po-

larization in Equation 2.10. It is responsible for self-steepening and shock formation at a pulse edge [43, 44].

Thus, with the inclusion of these additional effects we obtain the generalized Schrödinger equation in the following form

$$\frac{\partial A(z, t)}{\partial z} = -\frac{\alpha}{2} A + i \sum_{n \geq 1} \frac{i^n \beta_n}{n!} \frac{\partial^n A}{\partial t^n} + i \gamma \left(1 + \frac{i}{\omega_0} \frac{\partial}{\partial t} \right) \left(A(z, t) \int_0^\infty R(t') |A(z, t - t')|^2 dt' \right), \quad (2.15)$$

where the time t' comes from the retarded medium response. The first term on the right hand side of Equation 2.15 describes the losses, the second term the higher-order dispersion, the first term in brackets includes SPM, FWM and intrapulse Raman scattering and the second term in the bracket is responsible for the effect of self-steepening. The nonlinear response function $R(t)$ should include both the electronic and vibrational (Raman) contributions. By assuming that the electronic contribution is nearly instantaneous, the functional form of $R(t)$ can be written as [45]

$$R(t) = (1 - f_R) \delta(t) + f_R h_R(t), \quad (2.16)$$

where f_R represents the fractional contribution of the delayed Raman response governed by $h_R(t)$. The Raman response function $h_R(t)$ can be obtained from the Raman gain spectrum that has been measured experimentally. By using the known numerical value of peak Raman gain, f_R is estimated to be about 0.18 [45].

Equation 2.15 together with the response function $R(t)$ governs the evolution of femtosecond optical pulses within the slowly varying envelope approximation. It is easy to see that Equation 2.15 reduces to the conventional nonlinear Schrödinger equation (Eq. 2.13) for optical pulses much longer than the time scale of the Raman response function $h_R(t)$ since $R(t)$ for such pulses is replaced by the delta function $\delta(t)$. Noting that $h_R(t)$ becomes nearly zero for $t > 1$ ps, this replacement is valid for pulses having widths much greater than 1 ps.

2.2 Supercontinuum Generation in Hollow Fibers

Ultrashort pulses can be obtained not only directly out of an oscillator, but also by applying extracavity compression techniques. In this approach, the pulses are spectrally broadened by propagation through a suitable nonlinear medium and subsequently compressed in a dispersive delay line. In 1981, a new method for optical pulse compression based on spectral broadening by SPM was introduced, which arises during the propagation of short pulses in single-mode optical fibers [46]. With this technique 6 fs pulses at 620 nm have been generated using a prism-pair for external dispersion compensation [47]. Using an improved ultrabroad-band dispersion compensation scheme even 4.5 fs pulses at 800 nm have been achieved with the same technique [48]. However, the use of single-mode optical fibers limits the pulse energy of the input pulses to a few nanojoules.

Therefore, with the availability of high-energy (mJ) femtosecond pulses from solid-state laser amplifiers the need for new spectral broadening techniques was born. One possibility is to achieve spectral broadening in bulk materials [49]. However, due to the very short interaction length high intensities are needed to achieve the necessary nonlinearity for spectral broadening. These high intensities can lead to damage and spatial beam quality problems due to multiphoton ionization. Another particularly suitable technique for high-energy ultrashort pulses was introduced in 1996. It relies on spectral broadening by SPM in a hollow cylindrical fused silica fiber filled with a noble gas under pressure [15]. Using this approach pulses shorter than 5 fs have been generated at multigigawatt peak powers [27, 28]. It is this technique which we will study in this section in more detail.

2.2.1 Spectral broadening mechanisms in hollow fibers

Hollow fibers are suitable for large pulse energies because they provide a guiding element with a large-diameter single mode. In addition, the use of noble gases as nonlinear medium offers several important advantages compared to optical fibers. First, as long as the pressure in the fiber is not too high, the third-order nonlinearity is purely electronic. Thus, the Raman effect does not occur in hollow fibers. Second, by changing the gas type and its pressure it is possible to change the nonlinearity. And last but not least, no-

ble gases exhibit a high threshold intensity for multiphoton ionization especially for femtosecond pulses [15].

Propagation along hollow fibers can be thought of as occurring through grazing incidence reflections at the dielectric inner surface. Due to the angle-of-incidence dependence of the losses caused by these multiple reflections higher order modes are greatly suppressed. Thus, in a sufficiently long fiber only the fundamental mode can propagate. By proper mode matching [50] (i.e., $w_0/a \approx 2/3$, where w_0 is the spot size at the fiber entrance and a is the capillary radius), the incident radiation can be dominantly coupled into the fundamental EH_{11} hybrid mode, whose intensity profile as a function of the radial coordinate r is given by $I_0(r) = I_0 J_0^2(2.405r/a)$, where I_0 is the peak intensity and J_0 is the zero-order Bessel function [51].

In general, pulse propagation in gas-filled hollow fibers can be described by the same equations used for optical fibers. In hollow fibers two pulse broadening regimes exist depending on the input pulse duration. For longer pulses (140 fs) a purely SPM-broadened highly modulated spectrum is observed [52]. Whereas for shorter pulses (20 fs) a much more uniform spectrum is obtained which indicates that besides SPM also gas dispersion plays an important role [52]. For such short pulses the higher-order nonlinear effect of self-steepening has to be taken into account as well. This effect results from the intensity dependence of the group velocity [43, 44] and leads to an asymmetry in the SPM-broadened spectra with a larger broadening on the blue side.

The relative weights of SPM and dispersion can be evaluated using characteristic parameters such as the nonlinear length L_{NL} and the dispersion length L_D , defined as $L_{NL} = 1/(\gamma P_0)$ and $L_D = T_0^2/|\beta_2|$ [53], where β_2 is the GVD of the fiber filled with gas, P_0 is the peak power of the pulse and T_0 is the half-width (at the 1/e-intensity point) of the pulse. As soon as the fiber length L exceeds the nonlinear length L_{NL} and/or the dispersion length L_D , SPM and/or dispersion will play an important role in pulse propagation through the fiber. For best pulse compression, i.e. for the generation of linearly chirped pulses, an optimum fiber length L_{opt} exists, which is approximated by $L_{opt} \approx (6L_{NL}L_D)^{1/2}$ [54].

Two considerations set the limit when scaling this approach to supercontinuum generation to higher pulse energies. First, the laser peak power must stay smaller than the critical power P_c for self-focusing (for a Gaussian beam $P_c = \lambda^2/2\pi n_2$). This sets a

constraint on the type of noble gas used and its pressure. Second, the laser peak intensity should be smaller than the multiphoton ionization threshold which applies for the given pulse duration. This represents a constraint on the hollow fiber diameter and the type of gas used. Since the threshold for multiphoton ionization increases with decreasing pulse duration, this second constraint can be “softened” by using shorter pulses.

2.3 Supercontinuum Generation in Microstructure Fibers

With the invention of PCFs and microstructured fibers in the late 1990s it became possible to generate broadband supercontinua using oscillator pulses with pulse energies in the nanojoule range and at a repetition rate of ~ 100 MHz. Until then supercontinuum generation was only possible using amplified pulses at a kHz repetition rate.

The two fiber types, PCFs and microstructure fibers, differ in their guiding mechanisms. PCFs, also called photonic bandgap fibers, guide light by means of a photonic bandgap. Whereas microstructure or holey fibers, as they are sometimes called, take advantage of a microstructure cladding that has a reduced refractive index compared with the core and guide light like step-index fibers. As we only use microstructure fibers in our experiments we will limit our discussion in this Subsection to them. We will discuss the very special properties of these newly developed fibers and the nonlinear phenomena underlying the spectral broadening process in these fibers.

2.3.1 Special properties of microstructure fibers

Two recently published review articles provide a very good introduction to these new fibers [55, 56]. Microstructure fibers consist of a solid silica core surrounded by an array of air holes as shown in Figure 2.1. The first working microstructure fiber, which consisted of an array of ~ 300 nm air holes, spaced $2.3 \mu\text{m}$ apart, with a central solid core was demonstrated in 1996 [32]. The striking property of this fiber was its “endlessly single-mode” behaviour in the experiment, ranging from 337 nm to at least 1550 nm [57].

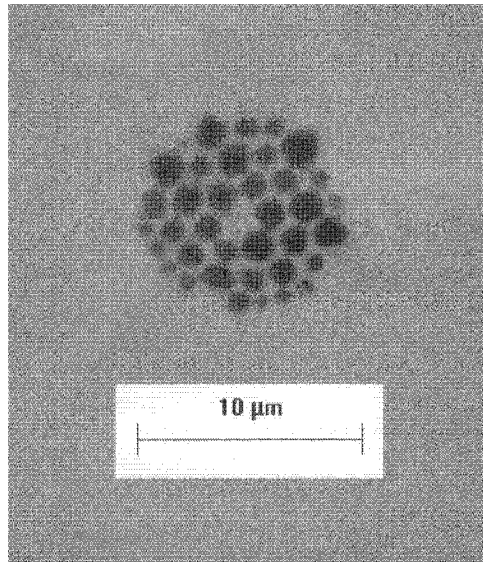


Figure 2.1: SEM-image of 1.7 μm core diameter microstructure fiber cross section (courtesy of Crystal Fibre).

Another very interesting property of microstructured fibers is that their dispersion can be controlled with unprecedented freedom. In conventional fibers the zero dispersion wavelength is located at 1.3 μm . But in microstructure fibers the zero dispersion point of the fiber can be shifted almost arbitrarily even to wavelengths in the visible by changing the waveguide contribution to the dispersion. By increasing (decreasing) the core diameter of the fiber, the waveguide contribution can be reduced (increased) thus allowing a fiber design with a zero dispersion wavelength anywhere from 650 nm to 1300 nm [58]. Only recently, a microstructure fiber was reported with close to zero dispersion over hundreds of nm in the infrared spectral region, making glass fiber almost as free of dispersion as vacuum [59].

Microstructure fibers with extremely small core diameters and very high air-filling fractions not only display unusual dispersion characteristics but also yield very high nonlinear interactions. Thus, one of the most successful applications of microstructure fibers is to nonlinear optics, where high effective nonlinearities together with a controllable dispersion are essential for efficient devices. As already mentioned, one such example is supercontinuum generation. It was discovered, that highly nonlinear microstructure fiber, designed with a zero dispersion wavelength close to 800 nm, displays giant spectral broadening when the 100 MHz pulses from a standard Ti:Sa-oscillator were injected into just a few cm of fiber [18, 60]. The emerging pulses have the band-

width of sunlight but are 10^4 times brighter ($> 100 \text{ GW m}^{-2}\text{sterad}^{-1}$). Thus it is not surprising, that this source is finding many uses, e.g. in optical coherence tomography [61]. The supercontinuum consists of millions of individual frequencies, precisely separated by the laser repetition rate. This “frequency comb” can be used to measure optical frequencies to an accuracy of one part in $5 \cdot 10^{-16}$ [62] or better.

2.3.2 Spectral broadening mechanisms in microstructure fibers

Unlike other nonlinear mechanisms the supercontinuum generation process in microstructure optical fibers is not yet fully understood. There exist several theories in parallel, some of them even contradicting each other. In this Subsection we will therefore present the most widespread opinion explained by means of two different propagation regime examples.

We begin our discussion by shortly explaining the spectral broadening mechanisms for picosecond input pulses. In contrast to femtosecond pulse pumping, the interplay between the different nonlinear processes involved is well understood. For picosecond pulses the contribution to spectral broadening from SPM is negligible. The primary mechanism is a combined action of SRS and parametric FWM [63].

In the femtosecond regime, there is a debate going on in the community about whether Raman processes are negligible for certain parameter regions (especially for input pulses with pulse durations of about 100 fs) or not. The most widely spread opinion is the following: For 100 fs pulses propagating through approximately 1m of fiber, a combination of SPM, FWM, SHG and Raman scattering produces a broad flat spectrum [18, 64]. In contrast, for pulses shorter than 30 fs propagating through only a few cm of fiber, the Raman contribution is suppressed and a stable continuum, generated primarily through SPM, is possible [64].

We split the discussion on femtosecond pulse propagation in two different pumping regimes. Depending on whether the pump wavelength is located below or above the zero dispersion wavelength (ZDW) of the fiber, we talk of normal dispersion pumping or anomalous dispersion pumping, respectively. Pumping in the normal dispersion regime allows for the generation of a stable continuum but at the cost of a limited bandwidth. The ultrabroadband, more than two octaves spanning supercontinua are

all produced in the anomalous dispersion regime, but have the disadvantage of being deeply modulated and unstable.

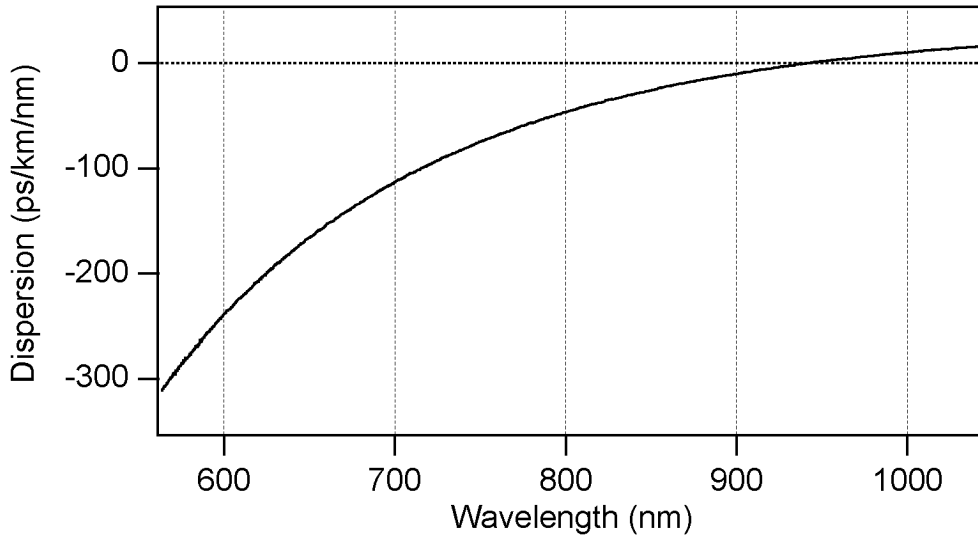


Figure 2.2: Dispersion curve of the 2.6 μm core diameter microstructure fiber showing a zero dispersion wavelength of 940 nm.

The 2.6 μm core diameter microstructure fiber, with which we were able to generate a stable continuum and demonstrated successful compression to 5.5 fs, exhibits the dispersion characteristics plotted in Figure 2.2. Its ZDW is at 940 nm and it is pumped by a Ti:Sa-oscillator centered at 790 nm. Therefore we start with the description of the spectral broadening process in the normal dispersion regime:

We first consider the case of pumping the fiber far below the ZDW (about 150 nm), as this is also the case in our experiment. We performed a numerical simulation on the propagation of 100 fs input pulses with a repetition rate of 80 MHz through 10 m of a microstructure fiber with the dispersion profile depicted above. More details on the numerical simulation are given in Chapter 5. At low powers launched into the fiber (5 mW) symmetric broadening due to SPM is observed (see Figure 2.3 for illustration). With increasing power new frequencies are generated on the red side through SRS, resulting in asymmetric broadening [65]. At 50 mW the output is very stable but has a limited bandwidth. It becomes unstable as soon as the first solitons are created when the broadened spectrum exceeds the ZDW. This happens at about 100 mW coupled into the fiber. The first soliton is formed just around the ZDW and is subsequently

self-frequency shifted to longer wavelengths as the pump power is further increased [66]. These simulation results are in good agreement with numerical simulations of other authors [65]. For powers of more than 100 mW our algorithm breaks down, but other simulations show that a tail starts to emerge on the blue side, its origin being self-steepening [65].

We did not try to pump closer to the ZDW, because in this case the generated continuum is more sensitive to changes in coupling efficiency and power fluctuations, leading to an increased instability. Here, the new spectral components generated on the short wavelength side are believed to originate from FWM, where solitons phase-match to spectral components from below the ZDW [66].

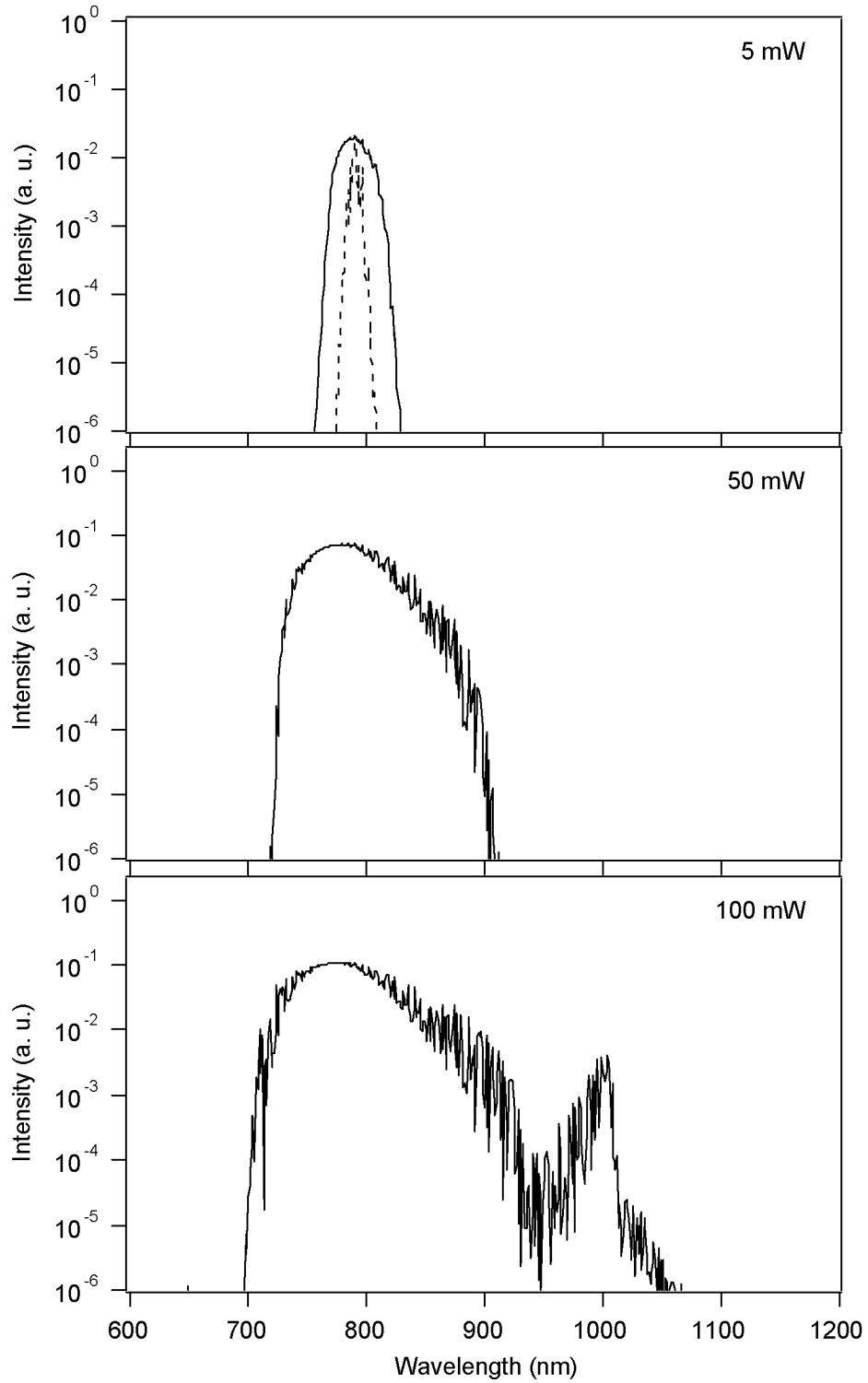


Figure 2.3: Simulation for 100 fs pulses propagating through 10 m of the 2.6 μm core diameter microstructure fiber for different launched input powers (the dashed curve shows the input pulse).

The second fiber used in our experiments, with which we generated broad white-light supercontinua but did not achieve successful compression, had a core diameter of $1.7\ \mu\text{m}$ and the ZDW at 665 nm. This is depicted in Figure 2.4. In contrast to the other fiber, this fiber was pumped in the anomalous dispersion regime.

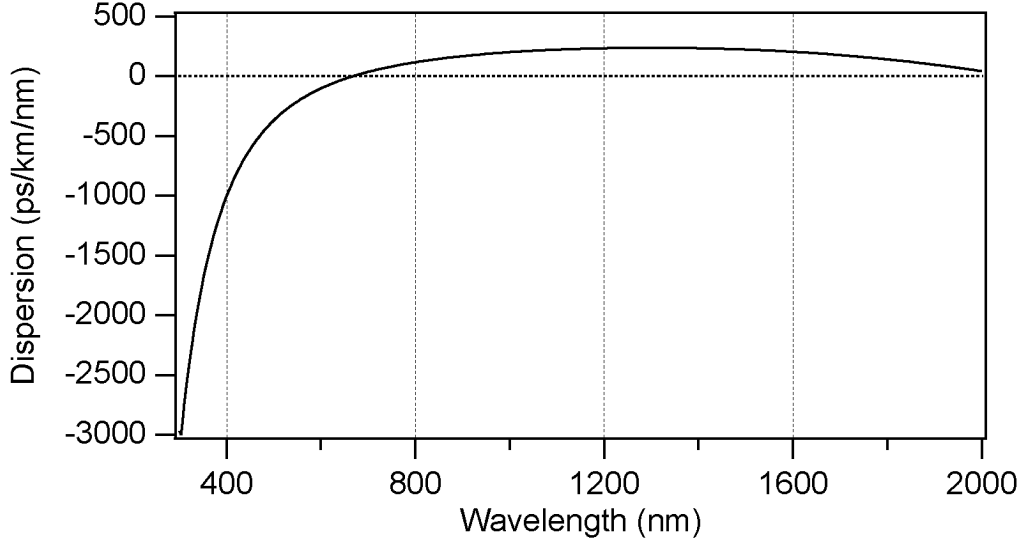


Figure 2.4: Dispersion curve of the $1.7\ \mu\text{m}$ core diameter microstructure fiber showing a zero dispersion wavelength of 665 nm.

Pumping significantly higher than the ZDW (around 100 nm higher), as it is the case for this fiber, leads to a complex interaction between multiple nonlinear effects allowing for ultrabroadband supercontinuum generation [66]. Again, we performed a numerical simulation on the propagation of 100 fs input pulses with a repetition rate of 80 MHz travelling through 5 m of a fiber with the dispersion profile shown in Figure 2.4. For an average power of 1 mW coupled into the fiber, the spectrum is initially broadened by SPM. This can be seen in Figure 2.5. The formation of a continuum is initiated by soliton decay due to Raman scattering. The initial pulse first decays into several sub-pulses: distinct redshifted Stokes components and simultaneously generated blueshifted anti-Stokes components (slowly growing) and a gap is formed in the vicinity of the ZDW.

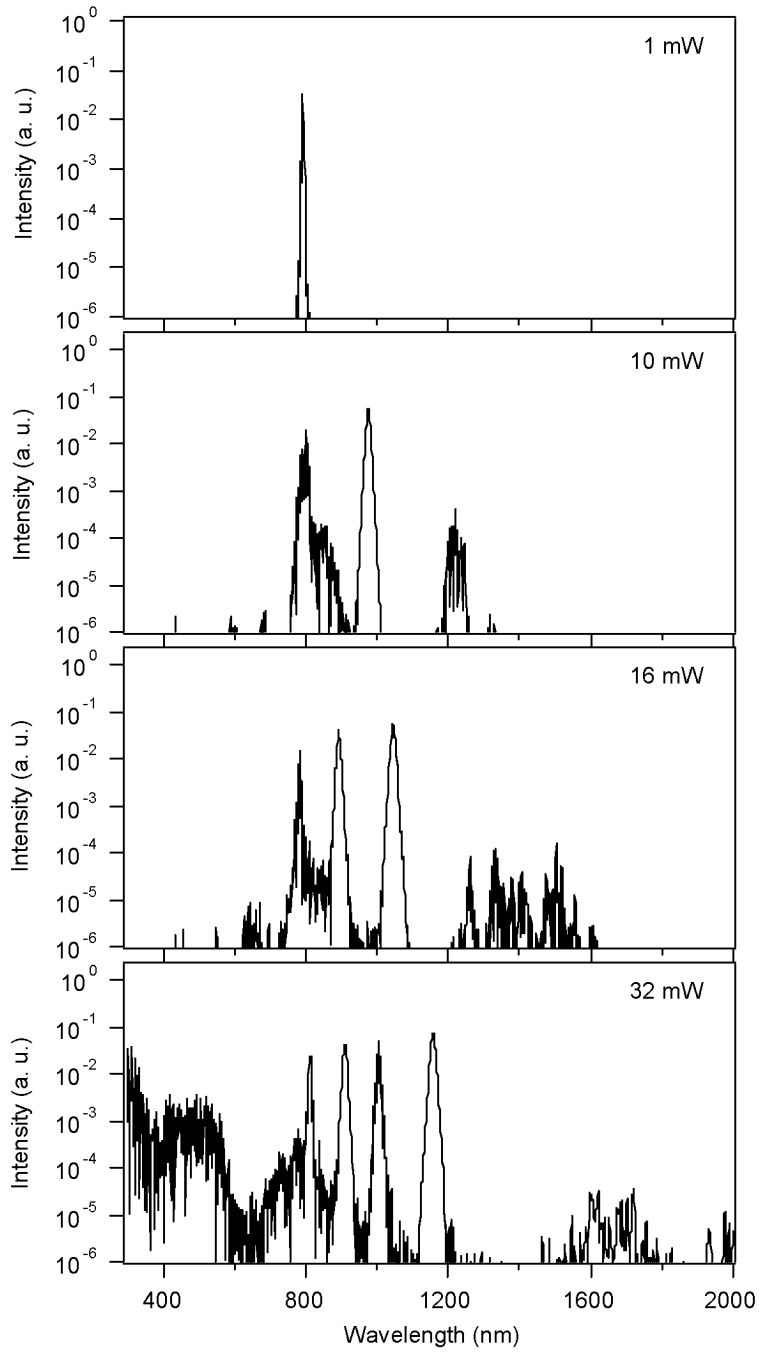


Figure 2.5: Simulation for 100 fs pulses propagating through 5 m of the 1.7 μm core diameter microstructure fiber for different launched input powers.

The onset of continuum generation can be described as follows: The pulse is initially compressed due to the combined effects of nonlinearities and anomalous dis-

persion before it breaks into multiple solitons. The solitons undergo a self-frequency shift and therefore appear in the spectrum as redshifted components (corresponding to the Stokes peaks). For input powers of about 30 mW these solitons get perturbed by higher order dispersion and therefore radiate energy to maintain their shape. This radiated energy appears in the spectrum as anti-Stokes peaks on the short wavelength side. Looking at the temporal evolution several delayed pulse components corresponding to the redshifted Raman solitons can be observed. The delay increases with peak power and thus with frequency shift. This is due to a decrease of the group velocity as the solitons shift towards the infrared. Dispersive waves are superimposed onto the temporal profile of the delayed solitons. These waves can be identified with the anti-Stokes components in the spectrum. This indicates that the Stokes and anti-Stokes components initially travel at the same group velocity so that energy transfer from the solitons to the radiated waves is possible. Pumping with higher average powers would result in the generation of a more uniform continuum [65]. Unfortunately, it was not possible to simulate this with our simulation algorithm.

Other simulations have shown that for 17.5 fs input pulses with the same peak intensity, the generated spectral width is 10 times smaller than for 100 fs pulses. This is in direct contrast to the behaviour of SPM-induced spectral broadening. Therefore, this indicates that in this regime, SPM is not the dominant contribution to spectral broadening, but that the spectrum broadens due to soliton fission. An explanation for the smaller bandwidth obtained with shorter pulse is that since for the smaller pulse duration the soliton number with $N = 1.5$ corresponds to one fundamental soliton, no soliton fission can occur and only an isolated blueshifted side peak is generated [67].

Let us now briefly consider the case of pumping only slightly above the ZDW in the anomalous dispersion regime. This leads to the same broadening mechanisms as described in the previous paragraphs, also for shorter (30 fs) pulses. But one can show that under these conditions the Raman contribution is negligible during the initial pulse propagation. Although Raman effects play an important role in the later stages of supercontinuum generation, the proximity of the pump wavelength to the ZDW means that the initial propagation is dominated by the interaction of SPM and self-steepening with higher-order dispersion (particularly TOD).

Pumping only slightly above the ZDW has the disadvantage, that the spectrum exhibits a highly complicated substructure that is extremely sensitive to the input pulse

energy. A 0.1% increase in pulse energy leads to a spectrum with a completely different fine substructure [68].

Chapter 3

Compression of Supercontinua

One application of coherent supercontinua is the generation of few-femtosecond optical pulses. To achieve this, the spectral phase distortion acquired during the spectral broadening process in the fiber has to be compensated for as good as possible. In the first Subsection of this Chapter, a short description of classical pulse compression techniques, such as the Gires-Tournois Interferometer (GTI) and prism and grating compressors [69, 70] is given. A well established technique for pulse compression based on silica fibers is the fiber-grating-compressor [71]. However, these classical techniques are not suitable anymore for the compression down to few-femtosecond pulses. Therefore, new dispersion compensation devices such as chirped [72] and double chirped mirrors [73, 74] have been invented. The disadvantage of these devices however is, that they are designed for one specific dispersion profile and it is not possible to continuously increase or decrease the introduced dispersion by an easily accessible, simple parameter of the mirrors or the mirror configuration (as it is possible with prism and grating compressors). It is only possible to change the amount of dispersion in discrete steps by adding or removing bounces off these mirrors. More flexible dispersion compensating devices are deformable mirrors [75] and spatial light modulators [76, 77]. Both devices are computer-controlled and can therefore be used for adaptive pulse compression or pulse shaping.

Using pixellated devices for dispersion compensation such as deformable mirrors or SLMs limits the compressor resolution and thus the amount of dispersion that can be compensated for. This effect is discussed in Section 3.3 and an estimation on the

maximum group delay and group delay dispersion, that can be compensated for with our SLM is given.

The most important prerequisite for proper dispersion compensation is an accurate measurement of the spectral phase of the pulse to be compressed. For such broadband pulses there exist only two reliable pulse characterization techniques: Frequency resolved optical gating (FROG) [78, 79] and spectral phase interferometry for direct electric field reconstruction (SPIDER) [80, 81]. Section 3.4 gives details on the SPIDER-setup used for our experiments and the improvements made to ensure correct pulse characterization of up to 600 nm broad spectra.

3.1 Different Compression Techniques

3.1.1 Classical techniques

3.1.1.1 Gires-Tournois Interferometer (GTI)

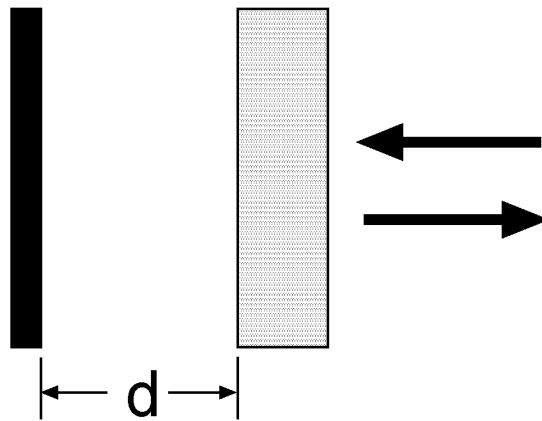


Figure 3.1: A Gires-Tournois Interferometer has a left mirror with a reflectivity of 100%, an air gap with thickness d , and a right mirror with a reflectivity of typically $< 10\%$.

A GTI is a Fabry-Perot reflector consisting of one mirror with a 100% reflectivity, an air gap or a non-absorbing material with thickness d , and a second mirror with a reflectivity of typically $< 10\%$. This is shown in Figure 3.1. This configuration introduces a

phase change, which is strongly frequency-dependent. In order to generate a large amount of negative dispersion, the thickness d must be relatively big. On the other hand the bandwidth is inversely proportional to d . This limits the applicability of the GTI typically to pulses longer than ~ 100 fs.

3.1.1.2 Prism-pair

Prism-pair compressors [69] are widely used for example inside Ti:sapphire-oscillators to compensate for the intracavity dispersion. In this technique the frequency-dependent deviation of a light beam as it passes through a prism is exploited. A schematic of such a prism compressor is shown in Figure 3.2. A prism with normal dispersion refracts short wavelength light (i.e. blue light) stronger than long wavelength light (i.e. red light). Therefore, the beam path inside the prism-pair is longer for the blue than for the red light. In this way, negative dispersion is produced. Because the beam is spectrally dispersed after the second prism one either reflects the beam back so that it passes through the same prisms again or one uses two more prisms aligned symmetrically to the first two prisms. This is a four-prism-compressor. The distance S between the two prisms determines the amount of negative dispersion. The prisms are Brewsters cut, which minimizes losses for p-polarized light and makes it possible to continuously adjust the total group velocity dispersion (GVD) of the prism sequence by moving one prism without spatially displacing the beam. By moving one prism into the beam positive dispersion is continuously added, because the beam has to propagate through a larger amount of prism material with positive dispersion.

One big advantage of prism compressors is that the introduced dispersion can be continuously adjusted without changing the beam position. A drawback of this technique is that it is usually only possible to compensate for one order of dispersion, typically the second. But the prism sequence itself introduces also third-order dispersion. Thus, for short pulses this limits the achievable pulse duration, because the non-compensated higher-order dispersion terms contribute dominantly to the pulse broadening. Using a prism-pair for the dispersion compensation of broad supercontinua would not be very practicable since the beam at the second prism would be spatially so much dispersed that either frequency components would be cut off or the second prism would have to be very big.

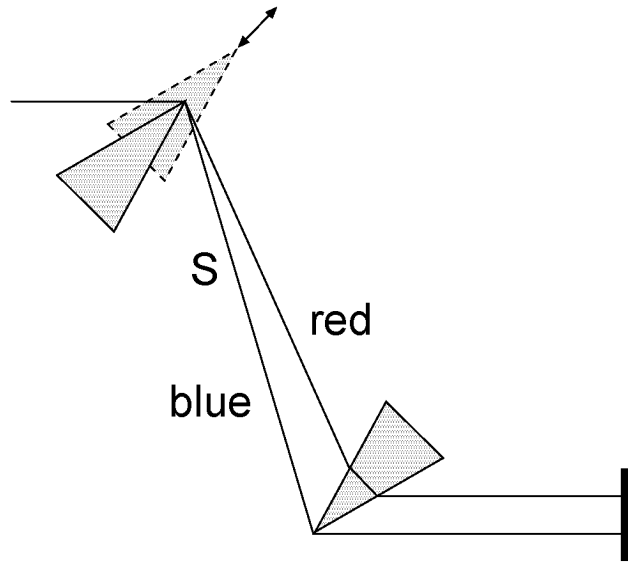


Figure 3.2: Schematic of a Four-prism-compressor, where the beam is backreflected with a mirror. The distance S between the prisms determines the amount of negative dispersion.

3.1.1.3 Grating-pair

Optical pulse compressors consisting of a diffraction grating pair have been developed already very early [70] and have found widespread use for example as stretcher-compressor assemblies in chirped pulse amplification (CPA) systems. Similar to the prism compressor the property that diffraction of light depends upon its wavelength is used for dispersion compensation. The difference is that here long wavelength light is diffracted more strongly than short wavelength light, thus increasing the beam path for the long wavelength components. Therefore, the frequency-dependent phase shift is introduced by the different beam paths the light passes between the gratings.

The incoming beam has an angle of incidence θ_i and the diffracted beam (m -th order) is determined by the angle θ_m . See Figure 3.3 for illustration. For $m > 0$ θ_m is larger than θ_i and gets even larger with longer wavelengths. Thus, the grating pair introduces positive dispersion. On the other hand, for $m < 0$, θ_m is smaller than θ_i and can even become negative. In this case, negative dispersion is produced.

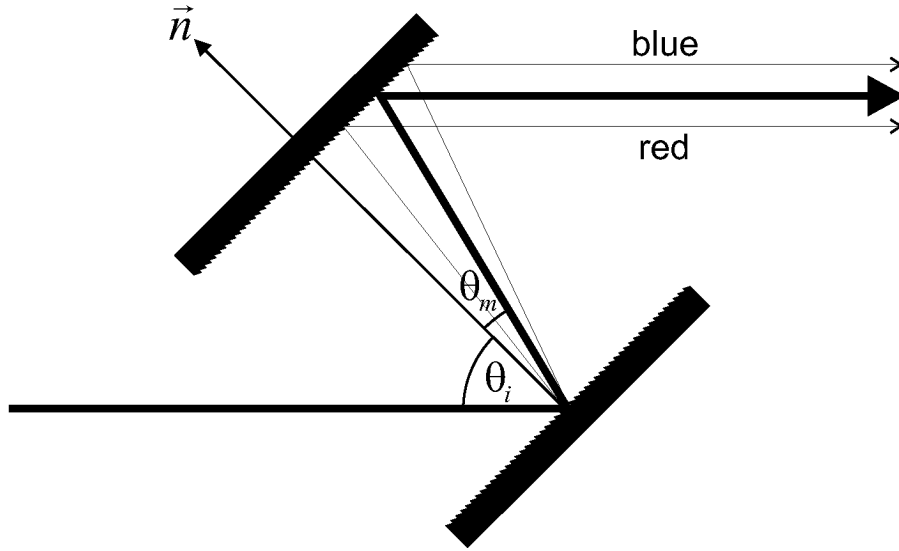


Figure 3.3: Negative dispersion introduced by a pair of diffraction gratings. θ_i is the angle of incidence of the incoming beam, and θ_m is the angle of diffraction.

In order to keep the losses in a grating compressor low, usually blazed gratings are used, because in such a grating only one order of diffraction is generated. According to the discussion above, a blazed grating for $m = -1$ is typically chosen for dispersion compensation. Diffraction efficiency is of particular importance, because analogous to the prism compressor, the light has to pass four gratings before the beam is spatially coherent again.

For pulse compression of broadband pulses, a grating pair is not the ideal solution because the diffraction efficiency of the gratings is strongly wavelength-dependent (and gratings with a good diffraction efficiency over several hundreds of nm do not exist). This may result in a significant spectral shaping of the continuum. The main disadvantage of using a grating pair for the compression of a continuum is however, that a large amount of higher-order dispersion is introduced.

3.1.1.4 Fiber-grating-compressor

SPM-induced pulse broadening can be used to further compress bandwidth-limited pulses. Pulse compression using fibers was first studied experimentally by Mollenauer et al. [82]. They used the combined action of SPM and negative dispersion in the fiber to compress the pulse already in the fiber itself. Working in the positive dispersion re-

gime of the fiber can also be used to further shorten a bandwidth-limited pulse by exploiting spectral broadening through SPM [54]. Here, the pulse is first launched into the fiber to broaden its spectrum and simultaneously it acquires a linear chirp during propagation through the fiber. This linear chirp is then compensated for by a grating pair as is illustrated in Figure 3.4. This technique was first developed by Nakatsuka and Grischkowsky [46, 83], whereas the grating compressor after the fiber was introduced by Shank [84].

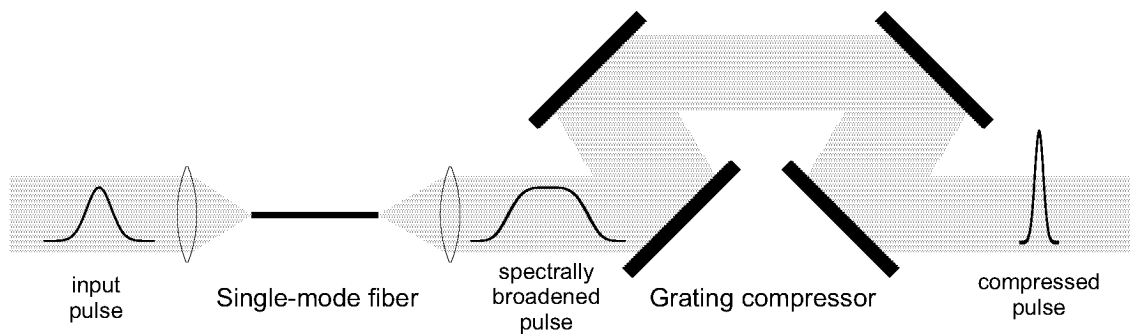


Figure 3.4: Schematic of a fiber-grating-compressor suitable for fs-pulses (after [71]).

To achieve pulse durations of below 10 fs the third-order dispersion had to be compensated for as well. Therefore, a combination of a grating- and a prism-compressor was used. This resulted in the generation of 6 fs pulses [47].

3.1.2 Chirped mirrors

A new concept for dispersion compensation was introduced in 1994 by Szipöcs et al. [72]. They designed a dielectric or “chirped” mirror which allows for the control of the effective plane of reflection of the different wavelength components. Chirped mirrors are custom tailored multilayer coatings, in which the Bragg wavelength is gradually decreased during deposition. Therefore, longer wavelengths can penetrate deeper into the coating than short wavelengths. This introduces negative dispersion.

A few years later, this original chirped mirror design was refined by the double chirped mirror (DCM) concept, which takes into account the impedance matching problem which occurs at the air mirror interface and the grating structure in the mirror [73, 74]. These DCMs resulted in new world-record pulse durations in the two-optical-cycle regime from Kerr-lens-modelocked (KLM) Ti:sapphire lasers [85, 86]. However, the

impedance matching to the air sets a limit. This impedance matching is based on a broadband anti-reflection (AR)-coating. Residual reflected light interferes with the main reflected beam. This interference results in a potentially detrimental modulation of the spectral phase. Therefore, the AR-coating has to be of high quality with a very low residual power reflectivity of less than 10^{-4} to minimize this effect [87]. However, this can only be achieved over a limited bandwidth and is impossible for more than about 0.7 optical octaves in the near-infrared and visible spectral range [88].

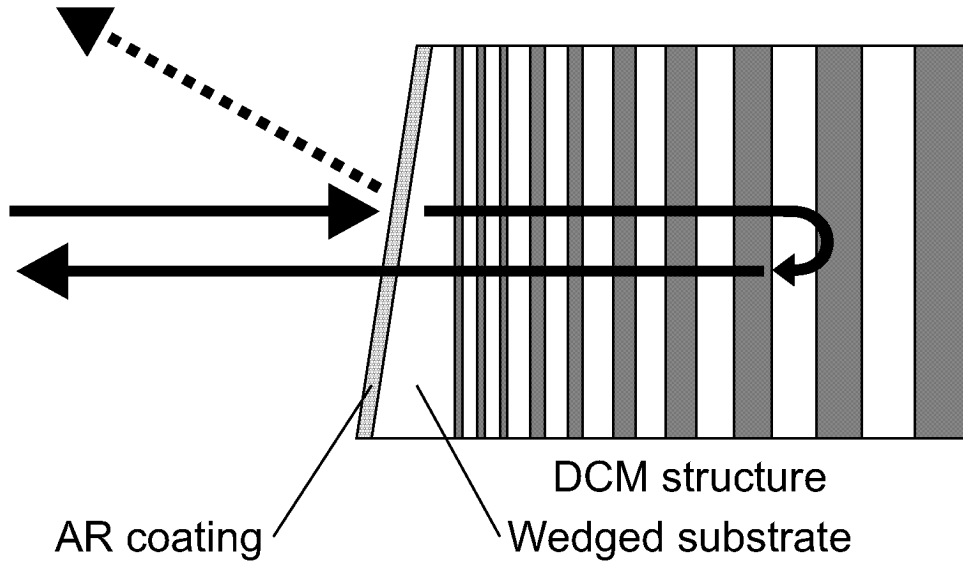


Figure 3.5: Schematic drawing of BASIC mirror showing the wedged substrate, the AR-coating on top of it and the DCM structure, which is deposited on the back of the substrate.

The invention of the back-side coated (BASIC) mirrors [87] or later the tilted front-side mirrors [89] resolved this issue. In the BASIC mirror, the DCM structure is impedance matched to the low index material of the mirror coating. The substrate material is chosen to match in refractive index to the low index coating material. The DCM structure is deposited on the back of the substrate. The substrate is slightly wedged or curved, so that the front reflection is directed out of the beam and does not deteriorate the dispersion properties of the DCM. An AR-coating is deposited on the front side of the substrate. For illustration see Figure 3.5. The purpose of this AR-coating is only to reduce the insertion losses of the mirror at the air-substrate interface. For most applications, it is sufficient to get this losses down to about 0.5%. Therefore, the bandwidth of such an AR-coating can be much broader. The trade-off is that the substrate has to be as thin as possible to minimize the overall material dispersion. In addition, the wedged

mirror leads to an undesired angular dispersion of the beam. Another possibility to overcome the AR-coating problem is given with the idea to use a DCM structure at the Brewster-angle incidence [90]. In this case, the low index layer is matched to air.

We conclude this Subsection with a discussion on the advantages and disadvantages of using chirped mirrors for dispersion compensation. It has to be noted, that the biggest advantage of chirped mirrors is that they allow for a very compact experimental setup and are easy to align. The limited bandwidth of conventional chirped mirrors and even DCMs was overcome with the invention of BASIC mirrors. But here the problem is, that these mirrors are very difficult to fabricate and very often several coating runs have to be performed before the mirrors have the dispersion properties they were designed for. Another disadvantage is that only relatively small amounts of dispersion can be compensated for by one mirror, so that usually several bounces off these mirrors are necessary for adequate dispersion compensation. In contrast to prism- and grating-compressors it is also not possible to continuously adjust the necessary dispersion. It is only possible to remove or add one bounce off a DCM. Thus, the step size is given by the amount of dispersion introduced by one mirror. A large number of bounces means also that the deviations from the desired phase multiply up.

3.2 Pulse Shaping Techniques: Deformable Mirrors and Spatial Light Modulators

Spatial light modulators (SLMs) and deformable mirrors were introduced not primarily for pulse compression applications but for femtosecond pulse shaping in general. Several different techniques for ultrafast pulse shaping have been developed. Here we concentrate on the most successful and widely spread method, in which waveform synthesis is achieved by spatial masking of the spatially dispersed optical frequency spectrum. We will focus on pulse shaping using deformable mirrors and in particular using SLMs. Both the deformable mirror and the SLM allow reprogrammable waveform generation under computer control.

Adaptive pulse shaping experiments have been performed using liquid crystal SLMs [91, 92, 93, 94, 95, 96], deformable mirrors [75], and acousto-optic modulators [97, 98]. Experimental demonstrations have included chirp compensation and shaping

of low energy pulses from femtosecond oscillators [75, 91, 92, 94], correction of residual chirps remaining after the pulse stretching and recompression process in high energy chirped pulse amplifiers [93, 95], and quantum control experiments, for example demonstrating adaptive pulse shape control of fluorescence yields [97] and photodissociation products [96].

In pulse shaping experiments it is generally desirable to be able to control both the phase and the amplitude of the pulse. As for our compression experiments only phase shaping is necessary, we will not discuss the aspects of amplitude shaping here.

Using adaptive pulse shapers in combination with a learning algorithm offers the big advantage, that an experimental observable (e.g., second harmonic generation intensity) can be optimized, for which the required spectral phase or pulse shape is not a priori known. The disadvantage is, that this method is very slow. The optimization procedure is significantly faster, if the required spectral phase is known, as it is the case in pulse compression experiments. Here, a measurement of the spectral phase or pulse shape is used as feedback. Thus, a few iterations are sufficient for optimization.

3.2.1 Femtosecond pulse shaping basics

3.2.1.1 Linear filtering

The description we use for the femtosecond pulse shaping approach is based on the linear, time-invariant filter, a concept well known in electrical engineering. Here linear filtering is applied for the generation of specially shaped optical waveforms on the picosecond and femtosecond time scale.

Linear filtering can be described either in the time domain or the frequency domain. This is shown in Figure 3.6 ([99]). In the time domain, the filter is characterized by an impulse response function $h(t)$. The output of the filter $e_{out}(t)$ in response to an input pulse $e_{in}(t)$ is given by the convolution of $e_{in}(t)$ and $h(t)$

$$e_{out}(t) = e_{in}(t) * h(t) = \int dt' e_{in}(t') h(t - t'), \quad (3.1)$$

where $*$ denotes convolution. If the input is a delta function, the output is simply $h(t)$.

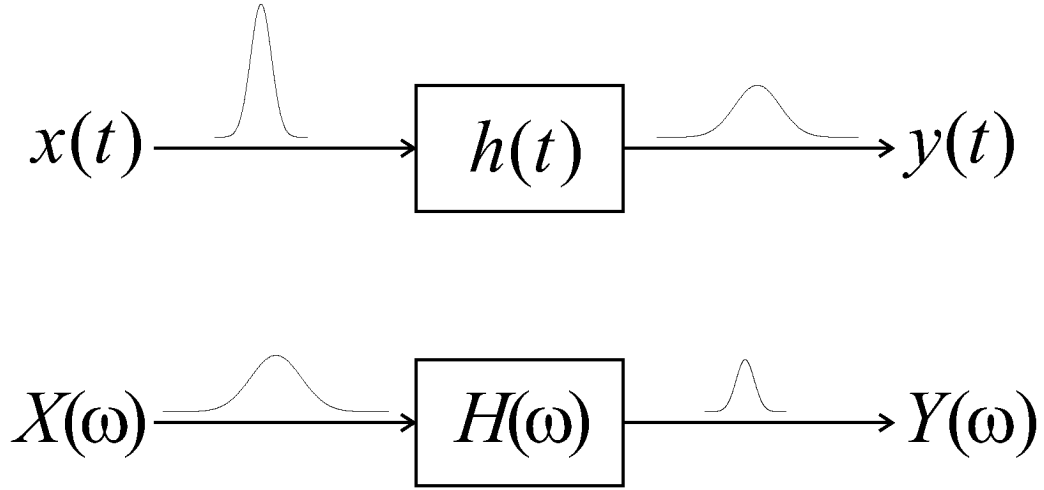


Figure 3.6: Pulse shaping by linear filtering. Top: Time-domain view, bottom: Frequency-domain view.

In the frequency domain, the filter is characterized by its frequency response $H(\omega)$. The output of the linear filter $E_{out}(\omega)$ is the product of the input signal $E_{in}(\omega)$ and the frequency response $H(\omega)$

$$E_{out}(\omega) = E_{in}(\omega)H(\omega) . \quad (3.2)$$

Here, $e_{in}(t)$, $e_{out}(t)$, and $h(t)$ and $E_{in}(\omega)$, $E_{out}(\omega)$, and $H(\omega)$, respectively, are Fourier transform pairs

$$H(\omega) = \int h(t)e^{-i\omega t} dt \quad (3.3)$$

and

$$h(t) = \frac{1}{2\pi} \int H(\omega)e^{i\omega t} d\omega . \quad (3.4)$$

For a delta function input pulse, the input spectrum $E_{in}(\omega)$ is equal to unity, and the output spectrum is equal to the frequency response of the filter. Therefore, due to the Fourier transform relations, generation of a desired output waveform can be accomplished by implementing a filter with the required frequency response.

3.2.1.2 Pulse shaping apparatus

A typical pulse shaping apparatus is shown in Figure 3.7. It consists of a pair of diffraction gratings and lenses, arranged in a configuration known as “zero dispersion pulse compressor”, and a pulse shaping mask [100]. The individual frequency components contained within the incident ultrashort pulse are angularly dispersed by the first diffraction grating, and then focused to small diffraction limited spots at the back focal plane of the first lens, where the frequency components are spatially separated along one dimension. Spatially patterned amplitude and phase masks (e. g. a SLM) are placed in this plane in order to manipulate the spatially dispersed frequency components. After a second lens and grating all the frequencies are recombined into a single collimated beam, and a shaped output pulse is obtained. As the name already suggests, the “zero dispersion” configuration of the gratings does ideally not introduce any dispersion, in contrast to the grating-compressor.

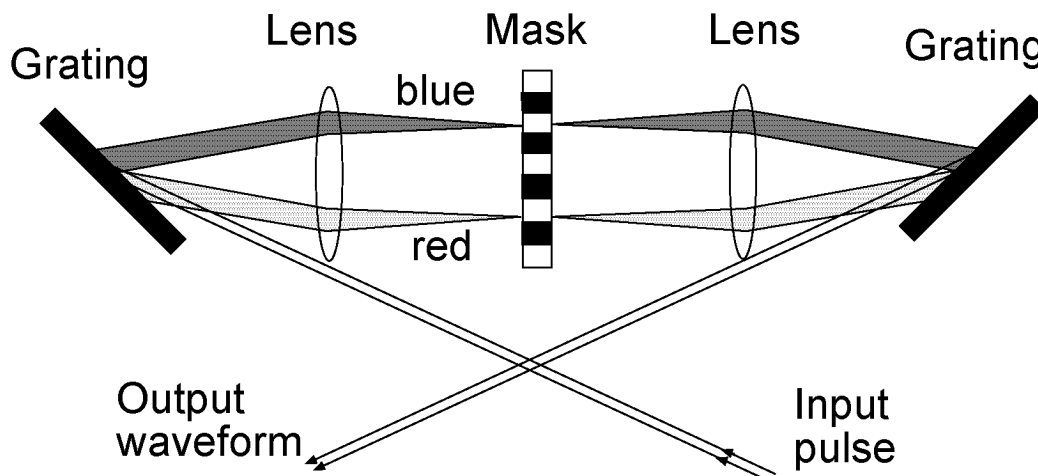


Figure 3.7: Pulse shaping setup that works by spatially masking spatially separated spectral components of a broadband optical pulse.

In order for this technique to work as desired, one has to make sure that in the absence of a pulse shaping mask, the output pulse is identical to the input pulse. Therefore, the grating and lens arrangement has to be truly free of dispersion. This can be guaranteed if the lenses are set up as a unit magnification telescope, with the gratings located at the outside focal planes of the telescope.

Note that this dispersion-free condition also depends on several approximations, e.g., that the lenses are thin and free of aberrations, that chromatic dispersion in passing through the lenses or other elements which may be inserted into the pulse shaper is small, and that the gratings have a flat spectral response. To fulfill these conditions is not a problem for pulses with durations down to roughly 50 fs (see [100, 101]). For much shorter pulses, especially in the 10 – 20 fs range, more care has to be taken to satisfy these approximations. For example, both the chromatic aberration of the lenses in the pulse shaper and the dispersion experienced in passing through the lenses can become important effects. However, by using spherical mirrors instead of lenses, these problems can be avoided and dispersion-free operation can be maintained [102].

The pulse shaper shown in Figure 3.7 was first used by Froehly et al., who performed pulse shaping experiments with 30-ps input pulses [103]. The same apparatus was subsequently adopted by Weiner et al. for manipulation of 100 fs pulses, initially using fixed masks [100] and later using programmable SLMs [76, 104]. With minor modifications, namely, replacing the lenses with spherical mirrors, pulse-shaping operation has been successfully demonstrated for input pulses on the 10 – 20 fs time scale [75, 91, 102, 105].

3.2.2 Deformable mirrors

Implementation of adaptive dispersion control based on a micro-machined deformable or flexible mirror requires spatial dispersion of the laser beam in order to actuate independently the path length of all frequency components across the spectrum. Therefore, the pulse compressor should inevitably incorporate a dispersion line that includes a focusing element and thereby provides a Fourier plane for spatial modulation of the dispersed laser beam. A common implementation of this device is shown in Figure 3.8, where a grating, which is set to the -1 diffraction order, is used to achieve the spectral divergence. This ensures that the system operates in the negative dispersion regime, which is important because of the low group delay correction provided by the membrane deflection of the micro-machined mirror. Therefore, the main correction of the spectral phase should be carried out by other elements of the pulse compressor, whereas the computer-controlled flexible mirror can only be employed for the fine group-delay tuning.

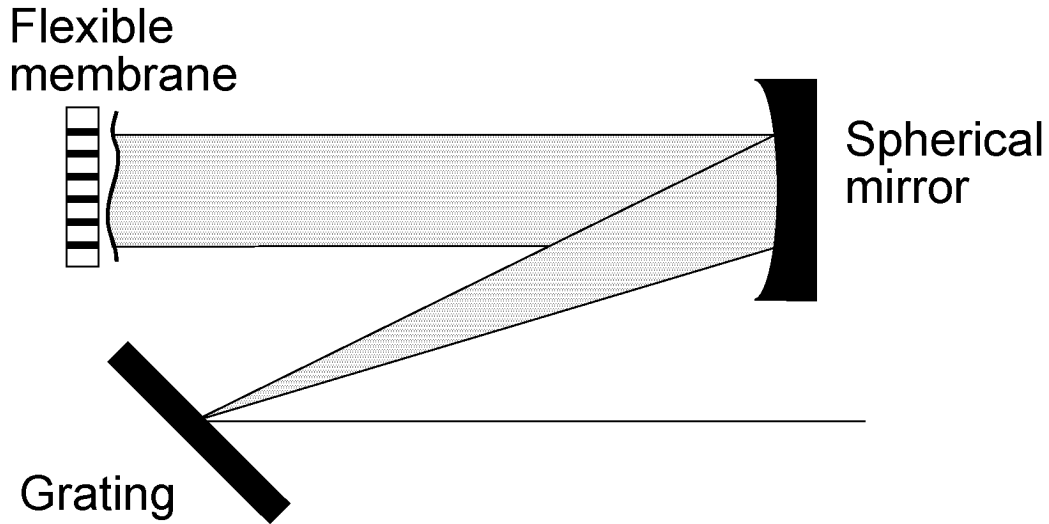


Figure 3.8: Schematic drawing of a typical implementation of a deformable mirror.

The membrane of a typical mirror frequently used by various groups is typically controlled by 39 actuators that are lined up in three rows and provides a clear aperture of $\sim 30 \times 7 \text{ mm}^2$ [75, 106]. The stiffness of the $0.5\text{-}\mu\text{m}$ silicon-nitride membrane depends on the material and amount of layers of the deposited optical coating. An Au coating with a Cr bonding layer underneath, for example, limits the maximum deflection to about $6 \text{ }\mu\text{m}$ in the center of the mirror.

Due to the relatively small number of actuators, and the existence of a minimum radius of curvature which can be induced on the membrane, this device is mainly useful for providing smooth phase variations.

Using a combination of chirped mirrors, a grating and a deformable mirror the successful compression of a noncollinear optical parametric amplifier (NOPA) spectrum to a pulse duration of 4 fs was demonstrated [31, 107].

3.2.3 Liquid crystal spatial light modulators

An excellent review on femtosecond pulse shaping using SLMs is given by Weiner [77]. Liquid crystal modulator arrays have been primarily configured for either phase-only or phase-and-amplitude operation. The liquid crystal array allows continuously variable phase control of each separate pixel (whereas fixed masks usually provide only

binary phase modulation) and allows programmable control of the pulse shape on a millisecond time scale.

Figure 3.9 shows a schematic of an electronically addressed, phase-only liquid crystal SLM [104]. A thin layer of a nematic liquid crystal ($\sim 9 \mu\text{m}$) is sandwiched between two pieces of glass. The nematic liquid crystal consists of long, thin, rod-like molecules, which in the absence of an electric field are aligned with their long axes along the x direction. When an electric field is applied (in the z direction), the liquid crystal molecules tilt along z , causing a refractive index change for x -polarized light. A maximum phase change of at least 2π is required for complete phase control. In order to apply the electric field, the inside surface of each piece of glass is coated with a thin, transparent, electrically conducting film of indium tin oxide. One piece is patterned into a number of separate electrodes (or pixels) with the corresponding fan out for electrical connections. Current commercially available liquid crystal SLMs have up to 640 pixels. Typically, each pixel is $97 \mu\text{m}$ wide and the pixels are separated by $3 \mu\text{m}$ gaps, thus such a SLM has a total aperture of 64 mm.

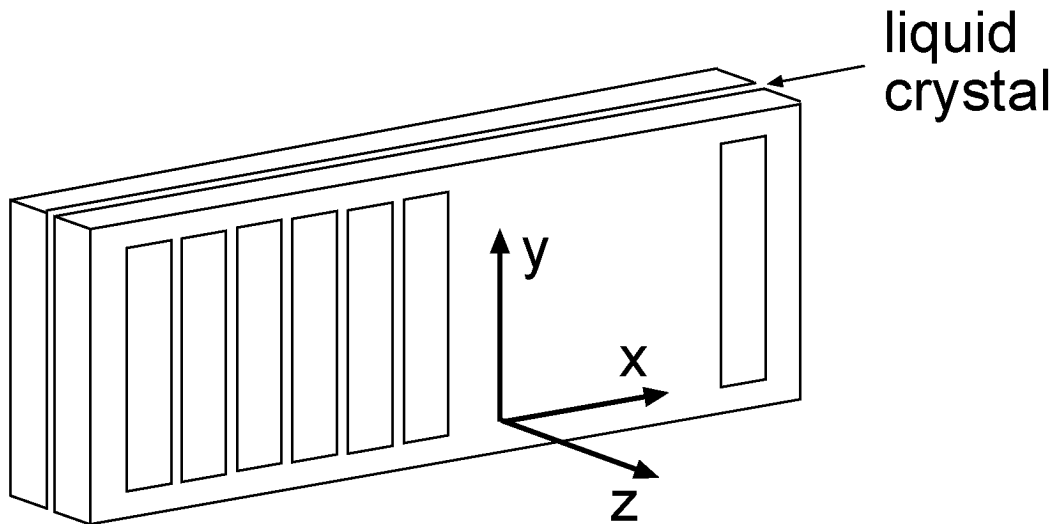


Figure 3.9: Schematic diagram of an electronically addressed, phase-only liquid crystal SLM.

In order to use liquid crystal SLMs for continuous phase control, a careful phase versus voltage calibration is required.

In comparison with deformable mirrors, liquid crystal SLMs have the advantage of much higher spectral resolution due to the much higher number of individual phase-controlling elements. Thus, it is possible to achieve complete dispersion compensation even for broadband spectra using only spatial light modulators [29, 108].

3.3 Compressor Resolution

Pixellated liquid crystal modulator arrays can be programmed to provide the desired phase function modulo 2π . This allows for the generation of large phase sweeps even with modulators, where the maximum phase change per pixel is as small as 2π . However, in any case of a smoothly varying target phase function the phase change from one pixel to the next should remain small enough that the staircase phase pattern, which is achieved by the liquid crystal modulator with its discrete pixels is a sufficiently good approximation to the desired phase function (mod 2π). In contrast to smooth phase functions, phase jumps can always be correctly shaped.

Let us now consider a smoothly varying phase function as it is required for pulse compression. Essentially the requirement addressed above is a sampling limitation: The phase must vary sufficiently slow that it is adequately sampled by the fixed modulator elements. This means we require $|\delta\phi| \ll \pi$, where $\delta\phi$ is the imposed phase change per pixel.

Assuming a compressor resolution of 1.1 nm as it is the case in our experiments, we calculate the maximum group delay (GD) and group delay dispersion (GDD) that can be compensated for by our 640-pixel SLM. For the maximum GD, we find the requirement

$$GD \ll \frac{\pi}{\Delta\omega_p}, \quad (3.5)$$

where $\Delta\omega_p$ is the frequency bandwidth spanned by one pixel. Since the grating generates a spatially dispersed beam, which is aequidistant in wavelength, the frequency bandwidth $\Delta\omega_p$ covered by one pixel varies significantly over the whole bandwidth of the spectrum. Therefore, we find a maximum GD of approximately 240 fs for 400 nm light and of 1500 fs for 1000 nm light.

For the maximum GDD we find as an estimate the condition

$$GDD \ll \frac{2\pi}{(\omega - \omega_0)^2 - ((\omega + \Delta\omega_p) - \omega_0)^2}, \quad (3.6)$$

where ω_0 is the vertex position of the parabolic phase corresponding to the GDD. The maximum GDD that can safely be shaped lies below the value obtained by this equation. The larger the bandwidth covered by the shaper the larger the safety margin with respect to this estimate needs to be. The reason for this lies again in the fact that the pixel spacing is evenly spaced in wavelengths but not in frequency.

For our shaper, covering a very large bandwidth from 310 nm to 1020 nm, the above equation yields $\sim 420 \text{ fs}^2$ and an $\omega_0 = 5.73 \text{ fs}^{-1}$ ($\lambda_0 = 329 \text{ nm}$) if we try to balance the maximum allowable GDD between the extreme blue and the extreme infrared side. In practice, we find that the real limit lies at about 200 fs^2 for this scenario. Significantly higher values can be achieved on the long wavelength side, if the requirements on the short wavelength side are relaxed (i. e., ω_0 is shifted to lower frequencies).

3.4 Broadband Pulse Characterization

The task of producing a shaped ultrashort pulse is closely related to the task of measuring such a shaped pulse. The field of ultrashort pulse measurement has undergone dramatic progress during the last decade, in parallel with progress in pulse shaping.

The technique which has been most often used for measuring shaped pulses (especially until recently) is intensity cross correlation [109]. The most significant limitation of this technique is the lack of any direct phase information. Furthermore, if the shaped pulse and the reference pulse are of comparable length, only very limited information on the shaped pulse shape can be extracted from the crosscorrelation. For measuring very broadband pulses the limited conversion efficiency bandwidth of the nonlinear crystal is another big drawback.

Unshaped pulses have been measured for many years via intensity autocorrelation [110]. However, for complicated pulse shapes, the intensity autocorrelation is usually not useful since most pulse shape information is lost.

An important breakthrough in the field of ultrafast optics was the relatively recent development of techniques for complete amplitude and phase characterization of ultrashort optical pulses. The two most widely spread techniques are frequency resolved optical gating (FROG) [78, 79] and spectral phase interferometry for direct electric field reconstruction (SPIDER) [81, 111].

In FROG, one gates the pulse to be measured with an identical time-delayed version of itself. The power spectrum of the output pulse resulting from the nonlinear gating interaction (usually second harmonic generation) is measured with a spectrometer as a function of time delay between the two pulses. Using an iterative computer algorithm both the complete intensity and phase profile of the ultrashort pulse can be recovered. A limitation of this approach is that for complicated waveforms, convergence of the iterative algorithm for recovering the temporal phase and intensity profiles from FROG data may become less dependable.

3.4.1 Spectral phase interferometry for direct electric-field reconstruction (SPIDER)

In our experiments, we choose to characterize the shaped pulses using the SPIDER-technique. In SPIDER, two temporally separated replicas of the pulse to be characterized are generated in a Michelson-Interferometer like setup and upconverted with a strongly linearly chirped pulse. This is illustrated in Figure 3.10. In the upconversion process, two identical but spectrally shifted pulses are generated. The resulting spectral interferogram is measured with a spectrometer and contains the phase difference between the two spectrally shifted pulses and a linear phase term owing to the time delay between them. Within the SPIDER retrieval algorithm this linear phase has to be subtracted from the SPIDER interferogram phase. Therefore, a calibration of the time delay is performed by additionally recording the interferogram of the SHG of the pulse replicas. Finally, the spectral phase is obtained by proper concatenation of the remaining phase differences.

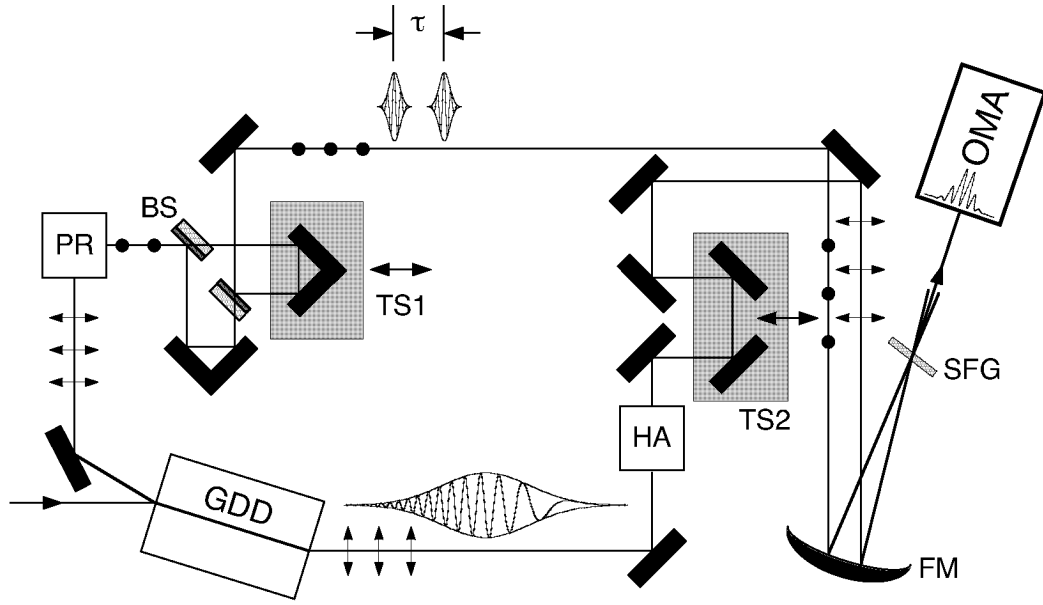


Figure 3.10: SPIDER setup: GDD: glass block for pulse stretching, PR: periscope for polarization rotation, BS: beamsplitter, TS1: translation stage for adjustment of delay, HA: periscope for height adjustment, FM: focusing mirror, SFG: nonlinear crystal, OMA: optical multichannel analyzer, TS2: translation stage for adjustment of overlap with upconverter pulse. Dots and arrows on the beam path display the polarization state of the beam.

A big advantage of SPIDER over other ultrashort pulse characterization techniques is that all the information is extracted from the fringe spacing of the interferogram. Therefore, slow variations in the nonlinear crystal's conversion efficiency over the pulse spectrum do not influence the reconstructed spectral phase. This is a consequence of the Takeda-theorem [112]. Another advantage especially compared to FROG is, that the reconstruction algorithm is much faster. Using SPIDER single-shot characterization of approximately 1 mJ pulses at a repetition rate of 1 kHz was demonstrated [113].

3.4.2 Implementation of a broadband SPIDER setup

When implementing our SPIDER setup for the characterization of broad supercontinua spanning bandwidths of up to 600 nm, we made sure not to introduce too much additional dispersion by using very thin beamsplitters and apart from that only reflective optics. Additionally, we were especially careful concerning the following two issues: the

bandwidth of our beamsplitters and the sum-frequency-generation (SFG) crystal we used.

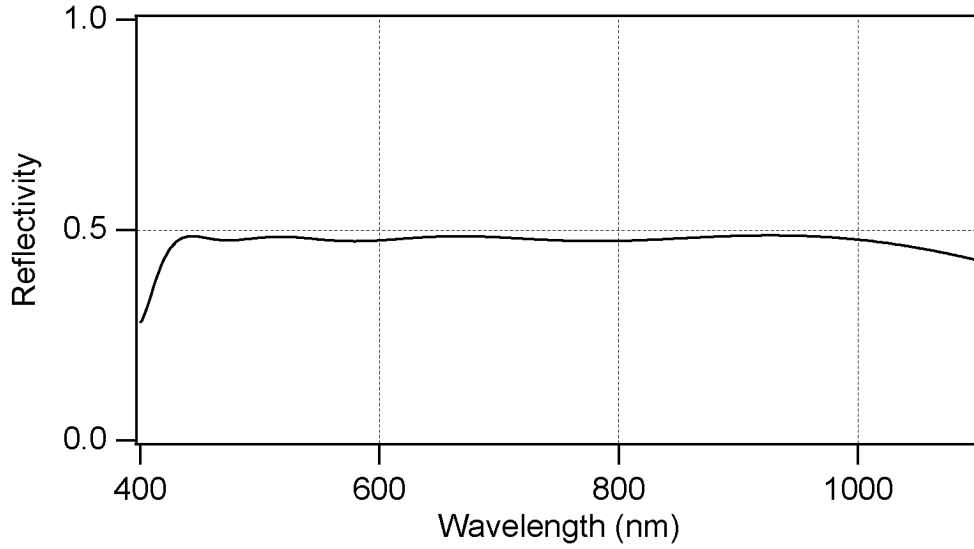


Figure 3.11: Designed reflectivity of the ultrabroadband beamsplitters.

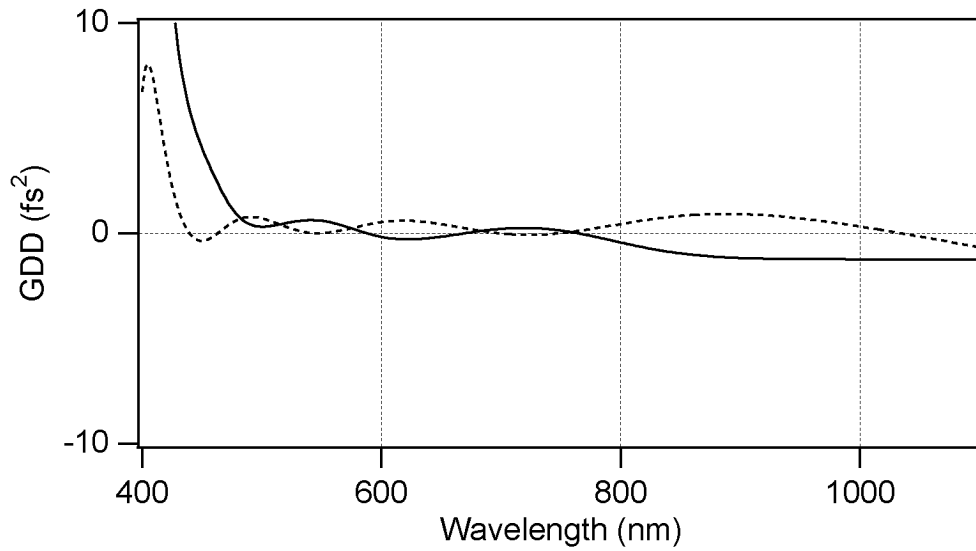


Figure 3.12: The solid curve shows the designed GDD of the beamsplitter coating in reflection and the dashed curve depicts the GDD in transmission.

We therefore decided to use custom-designed 400 μm thick ultrabroadband dielectric beamsplitters optimized for ultralow dispersion over bandwidths spanning from

450 nm to 1000 nm. As can be seen in Figure 3.11, the reflectivity of these beamsplitters varies only slightly over this bandwidth. Figure 3.12 shows the GDD on reflection and in transmission, respectively. In both cases the GDD varies only by a few fs^2 . We want to point out, that these are the theoretical design curves. From the measured transmission the reflectivity was calculated and is in very good agreement with the design. Simulations have shown that the dispersion properties of these beamsplitters are relatively insensitive against coating deposition errors.

For negative-uniaxial crystals, the phase-matching bandwidth in the ordinary axis of a type-II crystal is usually much larger than in a type-I crystal of same material and thickness, whereas the bandwidth in the extraordinary axis is smaller. Therefore, we chose a $30\text{ }\mu\text{m}$ thick β -barium-borate (BBO) crystal cut for type-II interaction. Using this crystal for type-II sum-frequency mixing of a broadband input pulse with the quasi-cw upconversion spectral slices in the extraordinary axis ensures a conversion efficiency bandwidth spanning from 530 nm to 1030 nm (FWHM) as is shown in Figure 3.13.

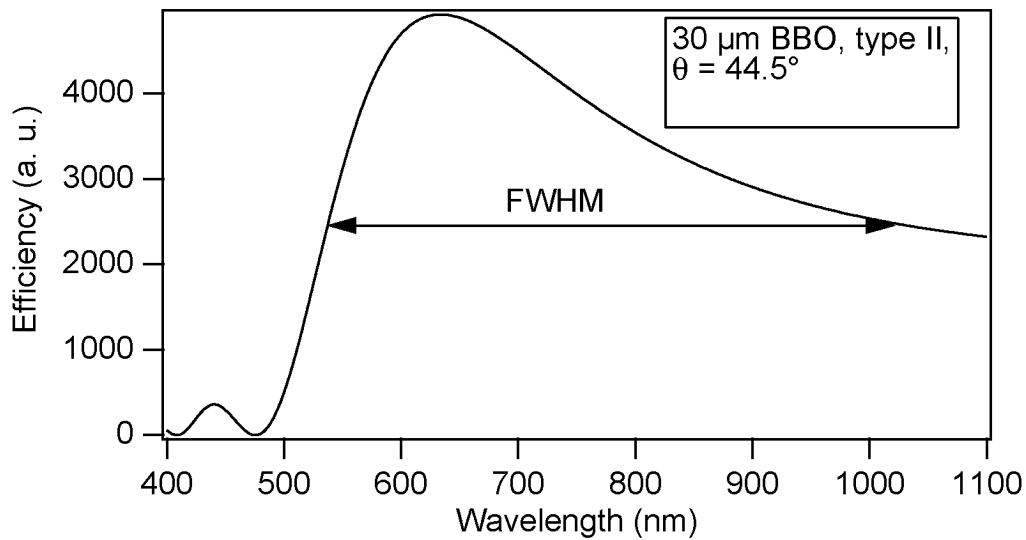


Figure 3.13: Conversion efficiency of a $30\text{ }\mu\text{m}$ BBO crystal cut for type II interaction at an angle of 44.5°

3.5 Adaptive Compression

We decided to use a 640-pixel liquid crystal spatial light modulator (SLM) for compression of the generated supercontinua, because it allows for adaptive and flexible optimization of the generated pulses. This is important because already slightly different fiber lengths make it necessary to be able to change the compressor settings. Compared to deformable mirrors the SLM has the advantage of a better compressor resolution due to a larger number of programmable elements.

One way to achieve compression with the SLM would be to use an evolutionary algorithm, starting the optimization procedure with a guess of the spectral phase. As this would result in a rather slow optimization and due to the fact, that we are able to measure the spectral phase of our supercontinuum, we decided to use this measured property as a feedback for our pulse compressor. In this way, compression can be achieved much faster after only a few iterations.

We will now explain how the adaptive compression of the generated supercontinua was implemented in our experiments. For illustration see Figure 3.14.

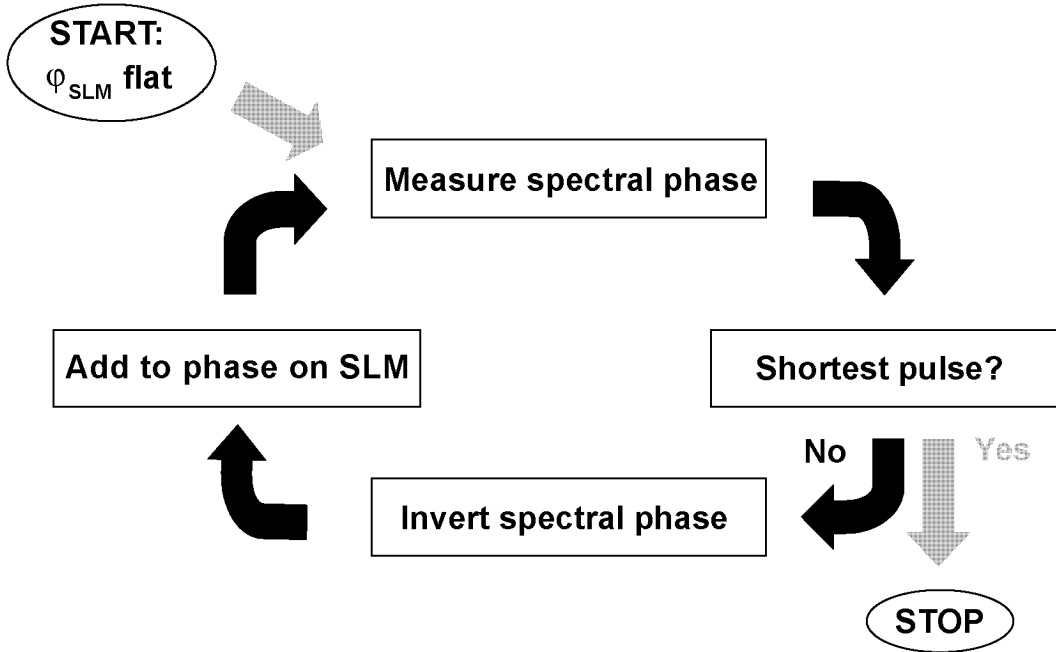


Figure 3.14: Schematic of the implementation of the compression algorithm used in the experiments

The compression was started by writing a flat spectral phase on the liquid crystal mask. Then the spectral phase of the transmitted pulse was measured using the SPIDER setup. Then we check whether the pulse is already fully compressed or not. If this is not the case yet, the spectral phase is inverted and added to the phase currently applied to the SLM. Then, we measure the spectral phase again and a new iteration begins. This procedure is continued until we yield the shortest pulse and then stopped. We find that typically 3-5 iterations are necessary to obtain maximum compression.

Chapter 4

Hollow-Fiber Experiments

In this Chapter, we will present our experiments on supercontinuum generation and compression using gas-filled hollow fibers. We were able to generate sub-4-fs light pulses with energies up to 15 μJ by compressing a portion of the supercontinuum produced in two cascaded gas-filled hollow fibers [108]. Dispersion compensation is achieved by measuring the spectral phase with spectral-phase interferometry for direct electric-field reconstruction (SPIDER, [81, 111]) and using this information as feedback for a liquid crystal SLM to iteratively compress the pulse.

The Chapter is organised as follows: First, we give a short motivation on why the generation of ultrashort pulses with high pulse energies is desirable and present an overview on what has been achieved towards this goal until now. The next Subsection is dedicated to our experimental setup including an explanation why we used two hollow fibers instead of only one. Our experimental results are presented in Subsection 4.3, followed by an estimation of the measurement error.

4.1 Motivation and Overview

The generation of high-peak power light pulses in the sub-4-fs regime is particularly important for a number of fundamental experiments, ranging from the production of single attosecond pulses by high-order harmonic generation [26], to the investigation of various nonlinear processes, where the absolute phase of the pulse plays a relevant role [25].

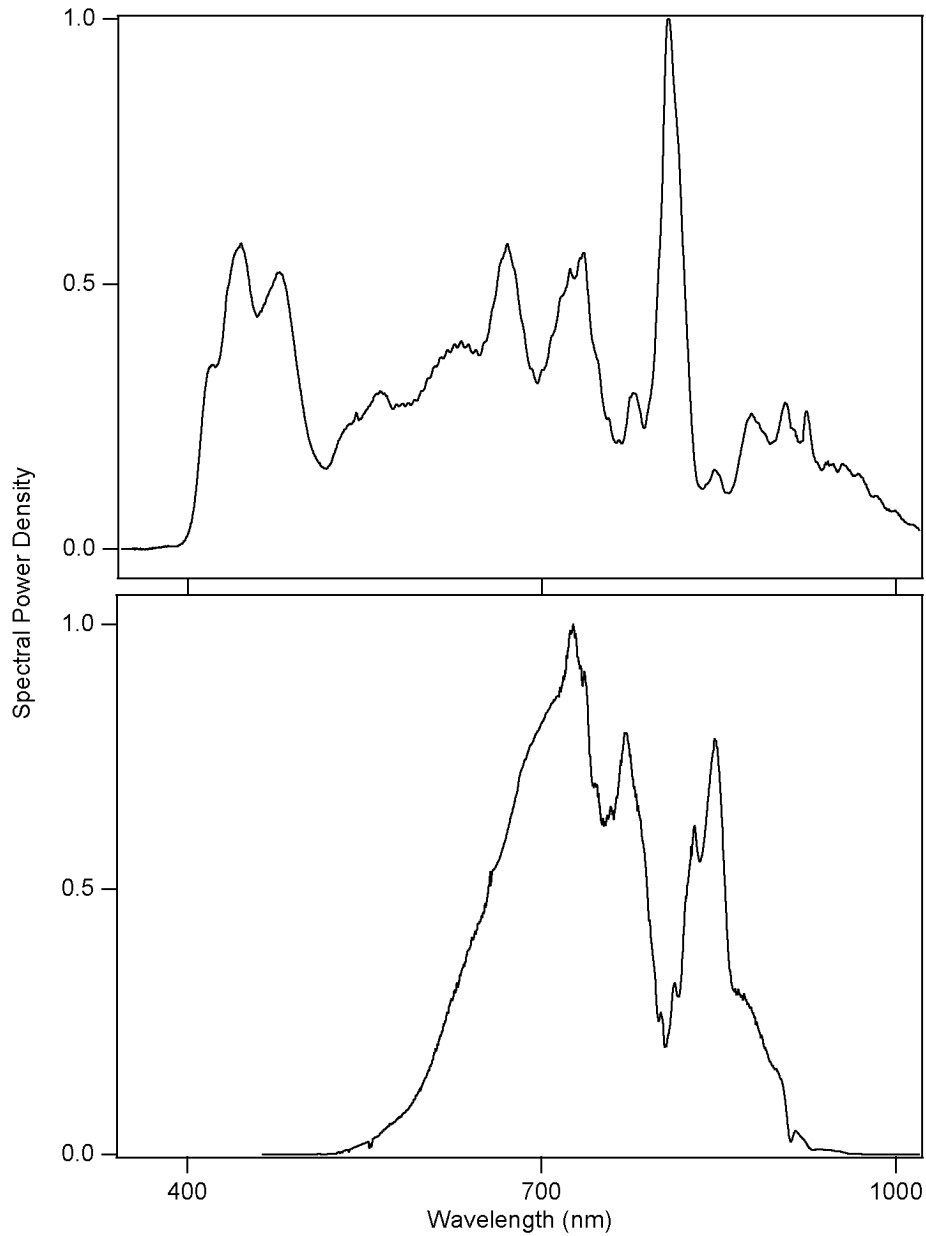


Figure 4.1: The top graph shows the measured supercontinuum output of two cascaded hollow fibers spanning a bandwidth of more than 600 nm. For comparison the output of a single hollow fiber is shown at the bottom.

In recent years, significant progress has been made in the generation of supercontinua in the visible and near-infrared spectral region from hollow and microstructured fibers. Since microstructure fiber supercontinua are not produced with high-energy pulses a detailed discussion on them is given separately in Chapter 5. Recently, a

high-energy supercontinuum extending on a bandwidth exceeding 500 THz (see Figure 4.1 (top graph)) has been generated using two gas-filled hollow fibers in a cascading configuration [20]. The main challenge now lies in the effective dispersion compensation and hence compression of the generated bandwidths to yield an isolated ultrashort optical pulse.

In previous work, compression of energetic supercontinua was achieved with different sources and/or compression techniques. The supercontinuum output of a single gas-filled hollow fiber has been compressed to 4.5 fs using a combination of chirped mirrors and thin prisms [27]. 5 fs pulses were obtained from the same technique by using chirped mirrors only [28] or a sole spatial light modulator (SLM) [29] for dispersion compensation. The generation of 4.5 fs pulses was achieved from a fiber-compressed output of a cavity-dumped Ti:sapphire laser [30]. From a completely different technique, pulses as short as 4 fs with an energy of 0.5 μJ have been generated using a non-collinear optical parametric amplifier (NOPA) and a dispersive delay line consisting of chirped mirrors, gratings and a programmable deformable mirror [31].

4.2 Experimental Setup

4.2.1 Continuum generation

The output beam of a 1-kHz Ti:Sapphire laser-amplifier system, delivering 25 fs pulses with pulse energies of 0.5 mJ, is focused into the first Argon-filled capillary consisting of a 60 cm long fiber with an inner diameter of 0.5 mm at the entrance side and 0.3 mm at the exit side (see Figure 4.2). The emerging pulses are then compressed by chirped mirrors (5 bounces, 30 fs² each). We like to note, that the gas pressure in the first fiber (0.3 bar) was not optimized for maximum spectral broadening, but chosen such that - after compression - 10 fs pulses with negligible wings are obtained. Sending these pulses ($\sim 300 \mu\text{J}$) into a second Ar-filled hollow fiber (constant inner diameter of 0.3 mm, 60 cm long) finally leads to a high-energy supercontinuum (100 μJ , 500 THz) with excellent spatial characteristics. Note that in comparison to a single hollow fiber, the use of two cascaded hollow fibers with an intermediate compression stage allows for the generation of a supercontinuum with more spectral energy in the blue and green part of the spectrum. This can be clearly seen in Figure 4.1, where the supercontinuum

obtained after two hollow fibers is plotted on top for comparison with the continuum generated with a single hollow fiber at the bottom.

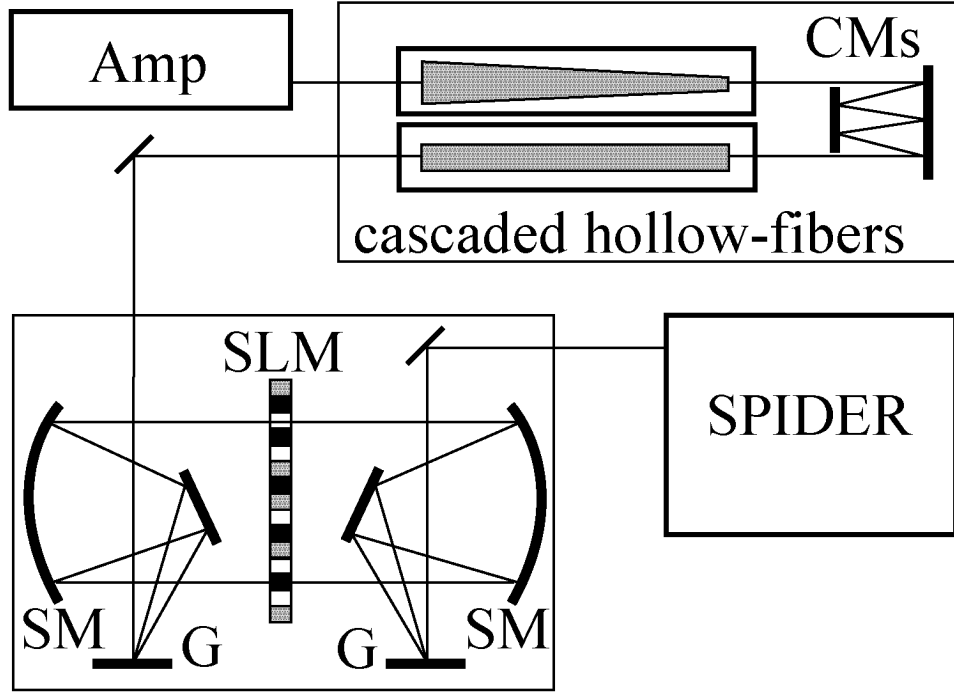


Figure 4.2: Schematic of our experimental setup: Amp, Ti:sapphire laser amplifier, 25 fs, 0.5 mJ, 1 kHz; CMs, chirped mirrors; Gs, 300 line/mm diffraction gratings; SMs, spherical mirrors, $f=300$ mm.

4.2.2 Pulse shaper

The emerging beam is then collimated and sent into the pulse shaper [77] consisting of a 640 pixel liquid crystal SLM (Jenoptik, each pixel is $97\text{ }\mu\text{m}$ wide and separated by a $3\text{ }\mu\text{m}$ gap), two 300 l/mm gratings and two 300 mm focal length spherical mirrors (4-f-setup). Alignment for normal incidence on the spherical mirrors (see Figure 4.2) proved to be very critical in order to preserve the good beam quality. This was necessary because of the very large beam diameter of 6.4 cm caused by the divergence of the gratings and the aperture of the SLM mask. Unfortunately, the gratings introduced considerable losses: with the pulse energy at the entrance of the pulse shaper being $100\text{ }\mu\text{J}$, it was measured to be $15\text{ }\mu\text{J}$ at the exit.

4.2.3 Pulse characterization and compression

Pulse characterization was performed by using SPIDER as it was already described in detail in Chapter 3. The spectral phase was reconstructed from the measured SPIDER trace and used to iteratively compress the pulse: Compression is started by writing an initially flat phase on the liquid crystal mask. Then, the measured spectral phase is inverted and added to the phase already applied to the SLM. In practice, we find that typically 5 iterations were necessary to yield the shortest pulse.

4.3 Results

The spectral phase of the supercontinuum has been observed to be very stable and constant for several hours. This is in excellent agreement with earlier measurements performed on phase fluctuations in hollow fibers [113] and is an important prerequisite for the successful application of this compression technique, which relies on a stable spectral phase.

To improve the performance of the SLM, it was necessary to reduce the steepness of the spectral phase in the center part of the spectrum. This decreases the phase difference applied to adjacent pixels on the liquid crystal mask and therefore facilitates dispersion compensation with the SLM. Herefor, we changed the position of the second grating in the pulse shaping setup from the zero dispersion position to a position, where most of the dominating quadratic phase of the pulse is compensated for.

Figure 4.3 shows the temporal profile of the shortest pulse we were able to generate with this technique. The full-width-at-half-maximum (FWHM) is measured to be 3.8 fs with a pulse energy of 15 μ J. The measured power spectrum spans a bandwidth of about 470 nm (see Figure 4.4) and has been cut at 530 nm by inserting a knife-edge into the spectrally dispersed beam inside the pulse shaping apparatus. The reason for this cutting is two-fold: Because of the lack of a strong enough up-conversion signal in the SPIDER apparatus from the shorter wavelength region, the spectral phase remained undetermined in this area. The second reason is the strong scattered fundamental light which has to be kept from interfering with the SPIDER-signal in the spectrometer and therefore from decreasing the modulation depth. These problems could be re-

solved by using cross-correlation-SPIDER [114], increasing the signal strength and decreasing interference effects with scattered light.

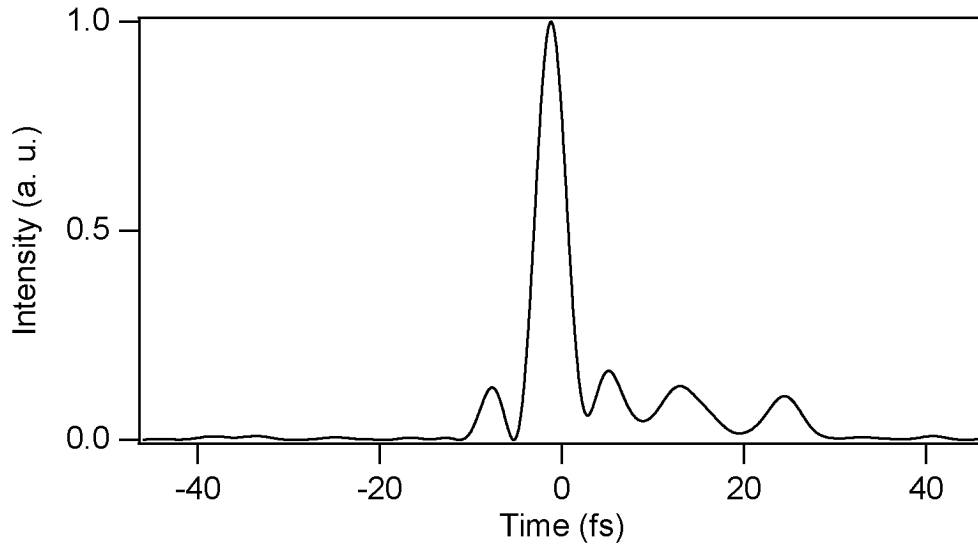


Figure 4.3: Reconstructed temporal pulse profile showing a FWHM pulse duration of 3.77 fs.

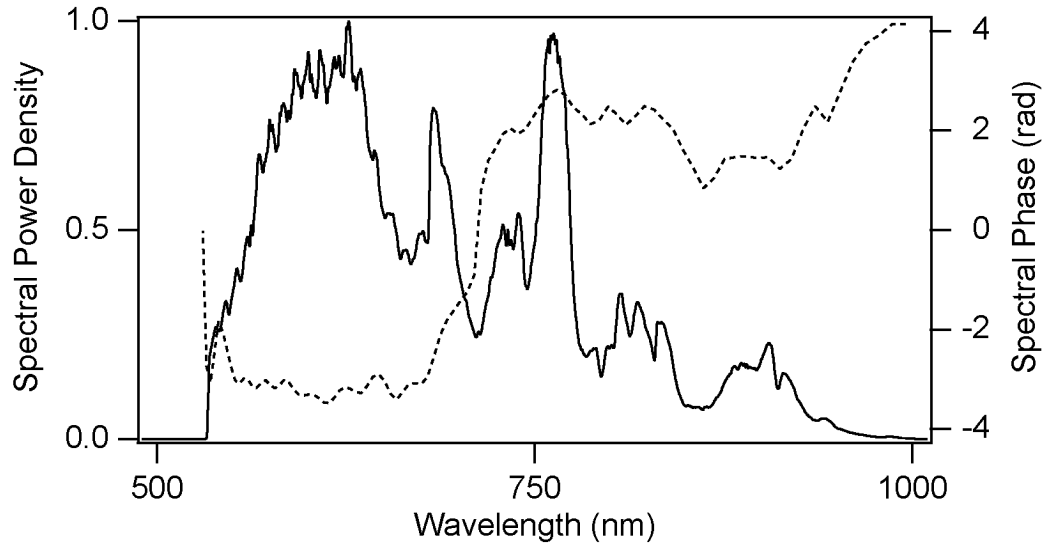


Figure 4.4: Solid curve, experimentally measured fundamental spectrum obtained after the pulse shaper, which has been cut at 530 nm and spans a bandwidth of 470 nm. The dashed curve depicts the reconstructed spectral phase of the pulse.

Figure 4.4 shows the spectral phase to be essentially flat over the entire bandwidth except for a near 2π step at about 710 nm. The jump in phase accounts for the pre- and after-pulses in the temporal domain (Figure 4.3). The corresponding SPIDER-trace is shown in Figure 4.5. As can be seen, the fringe visibility is good over the entire bandwidth.

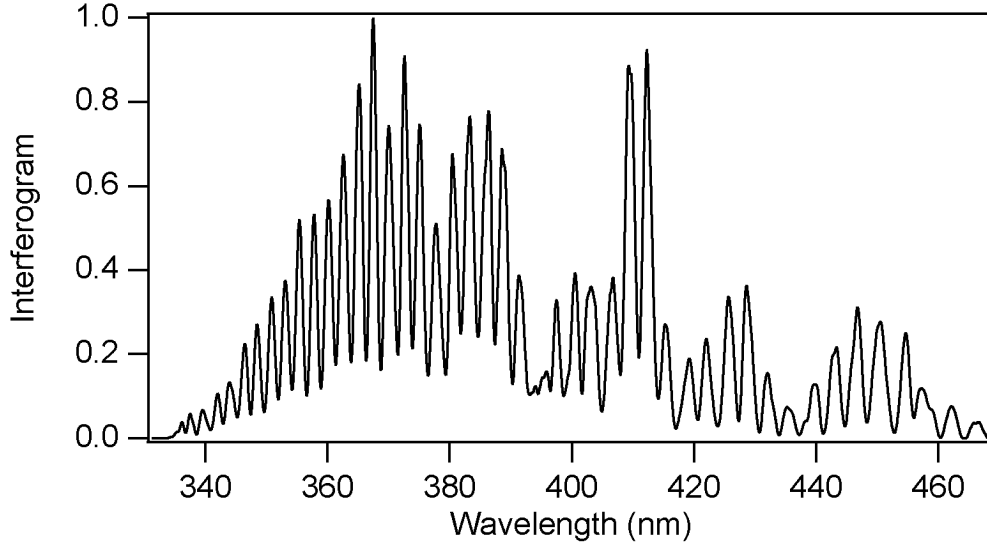


Figure 4.5: Measured SPIDER-interferogram showing a good fringe visibility over the entire bandwidth.

We calculated the center-wavelength of this pulse to be 673 nm. From this we find that the pulse is 1.7 cycles long. For further illustration the electric field of the pulse was calculated and is shown in Figure 4.6.

For completeness we also calculated the interferometric autocorrelation (IAC) of the pulse. Figure 4.7 shows that it is looking reasonable. If one extracts the pulse duration out of this IAC taking into account that the center wavelength is 673 nm, one finds that the pulse is only 3.5 fs long (assuming a sech^2 pulse shape).

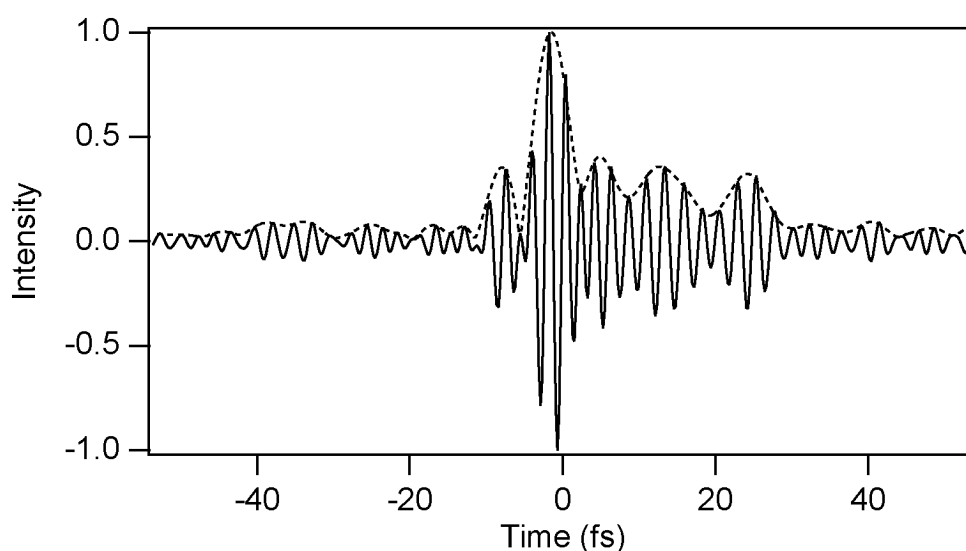


Figure 4.6: Solid curve: Calculated electric field showing 1.7 cycles under the pulse envelope (dashed curve).

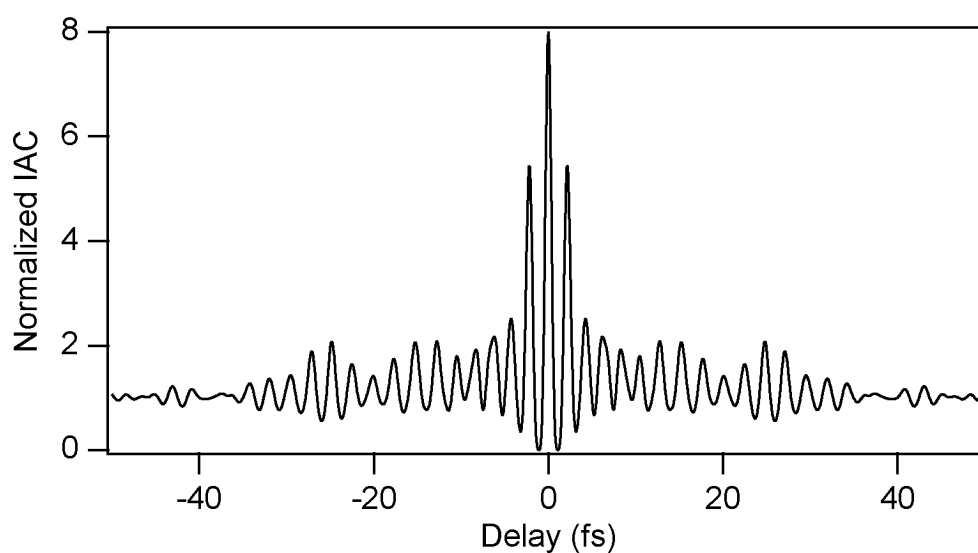


Figure 4.7: Calculated interferometric autocorrelation of the 3.8 fs pulse.

We tried to eliminate the phase jump by adding one more iteration but with no success. The top graph in Figure 4.8 shows the phase which was applied to the SLM at the time of measurement. An “edge” at 710 nm can be clearly seen, which is exactly the position at which the phase jump occurs in the measured spectral phase. Going back through the previous iterations we find, that this edge arises by adding up the individu-

ally measured spectral phases, which show some high-frequency noise around 710 nm. This disturbance can also be clearly seen in the bottom graph of the same Figure. Here, the phasedifference between adjacent pixels on the SLM is plotted versus wavelength. We note that careful application of a smoothing algorithm between the individual iterations could resolve the above problem.

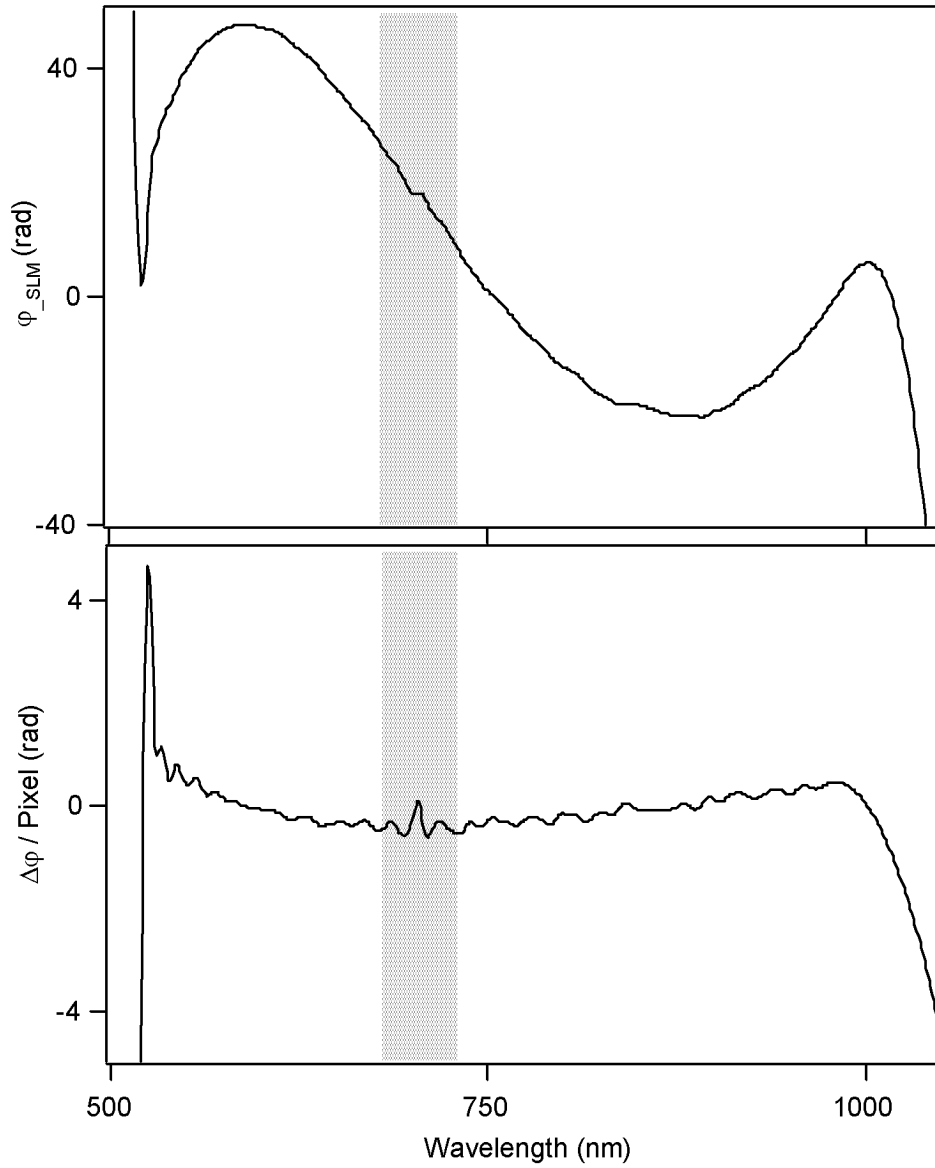


Figure 4.8: Top: Spectral phase applied to the SLM showing an edge at 710 nm, bottom: phasedifference between adjacent pixels on the SLM clearly showing a disturbance at 710 nm.

Due to this high-frequency noise locally accumulated over a few iterations, compression failed in this spectral region. However, due to the steep phase transition, the pulse duration was only slightly influenced and the main impact is on the pulse contrast. We proved this statement by adding 2π to the short wavelength part of the spectral phase and removing the dip which then appears in the center. This leads to an artificially flattened spectral phase over the entire bandwidth as shown in Figure 4.9. Using this artificial spectral phase to reconstruct the pulse shape leads to the pulse shown in Figure 4.10. The pulse has a FWHM pulse duration of 4.1 fs and less after-pulses.

It may be surprising, that the FWHM pulse duration of the pulse is slightly longer with the flat spectral phase. But this can be explained by the fact, that a flat spectral phase does not necessarily result in the shortest FWHM pulse duration, but does result in the shortest rms pulse duration, which takes into account the whole shape to the pulse.

In conclusion, we have demonstrated the generation of pulses as short as 3.8 fs with pulse energies of 15 μJ by adaptive compression of the supercontinuum output of two cascaded hollow fibers using only a SLM for dispersion compensation [108]. To the best of our knowledge, these are among the shortest pulses ever generated in the visible and near-infrared spectral region. Last year, the group of Yamashita demonstrated 3.4 fs pulses with a pulse energy of 0.5 μJ using only a single hollow fiber for continuum generation [19]. Compared to these pulses and the OPA [31] - the technique of adaptive cascaded hollow fiber compression provides more than an order of magnitude higher pulse energies (15 μJ) therefore being a potential source even for high harmonic generation experiments.

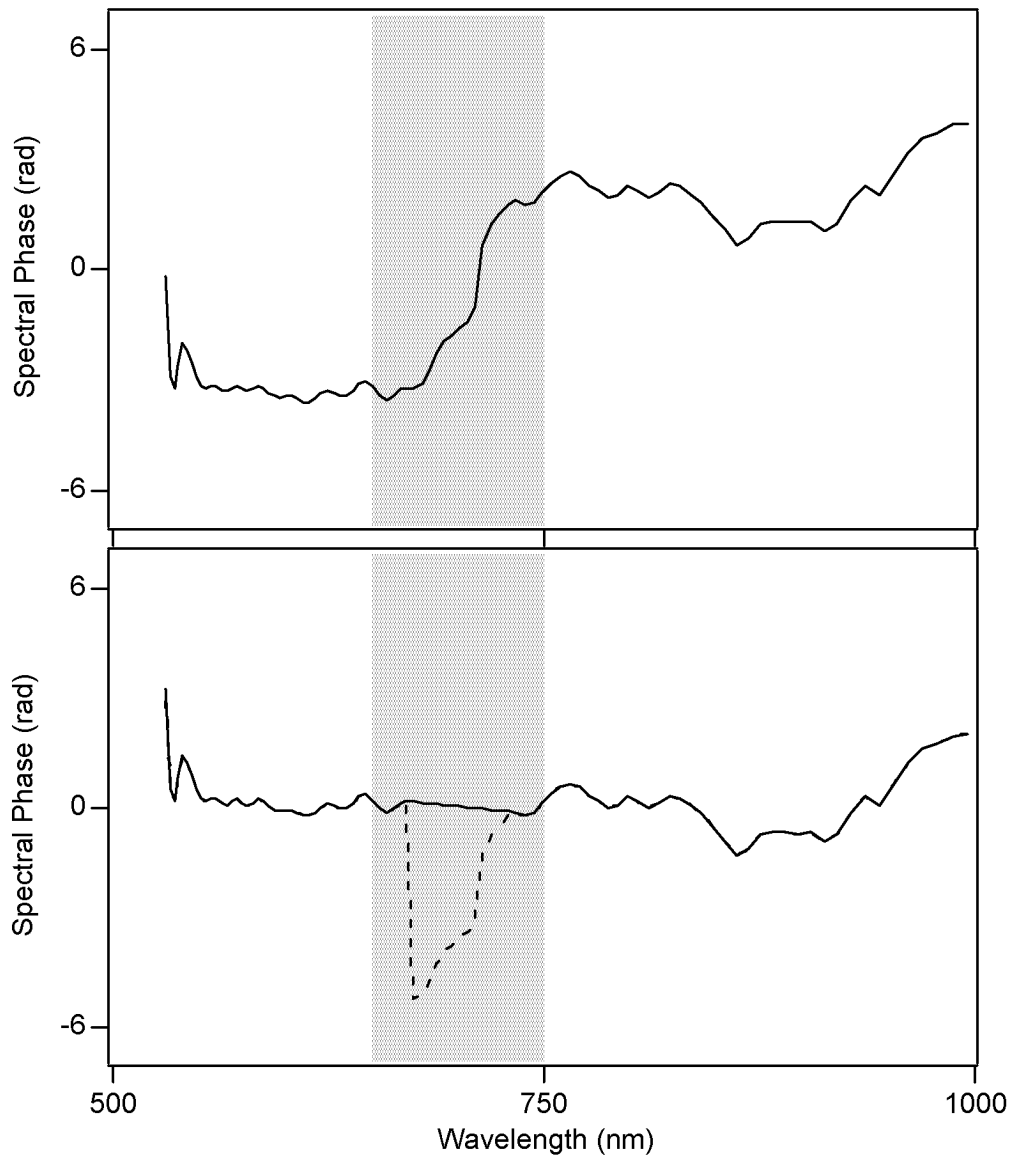


Figure 4.9: Artificially flattened spectral phase by adding 2π to the short wavelength side and removing the dip (dotted line), which then appears.

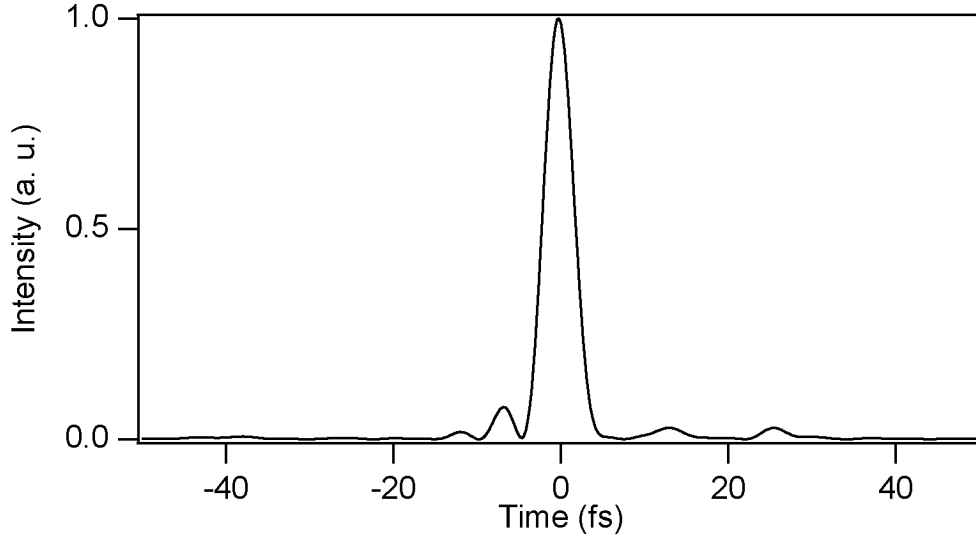


Figure 4.10: Reconstructed pulse shape showing a FWHM pulse duration of 4.1 fs, obtained with the artificially flattened spectral phase from the previous Figure.

4.4 Error Estimations

As already mentioned in Chapter 3, within the SPIDER retrieval algorithm, the linear phase owing to the time delay between the two pulse replicas has to be subtracted from the SPIDER interferogram phase [111]. The determination of this time delay is crucial because it has the most significant influence on measurement errors of the reconstructed pulse duration [115]. We therefore performed an error estimation on the measured pulse duration by evaluating the precision of the calibration of this time delay. The value of the delay retrieved from the interferogram of the two replicas was measured to be $\tau = 179.81$ fs. Hence, the reconstruction algorithm yields the spectral phase and temporal pulse profile with a FWHM duration of 3.77 fs depicted in Figure 4.4 and Figure 4.3 respectively. We compared the linear phase of the above measurement with the linear phase measured several hours before. We found that the long term stability is good enough to yield a value within $\Delta\tau = 0.01$ fs of the original delay. Performing the reconstruction with $\tau + \Delta\tau$ yields a FWHM pulse duration of 3.81 fs. The influence of random noise on the pulse reconstruction was estimated by fitting a straight line to the linear phase caused by the delay. The standard deviation of the delay was found to be $\langle\Delta\tau\rangle = 0.07$ fs. This corresponds to an error of $(3.77 + 0.11 - 0)$ fs in pulse duration.

From our experience with SPIDER and our particular implementation of it [81], we find that this delay parameter is typically reproducible to within better than 0.1 fs over hours of operation.

We have also checked the influence of the finite bandwidth of our sum-frequency mixing crystal on the measured pulse duration. Correcting the measured SPIDER-trace for a finite crystal bandwidth yields a FWHM pulse duration of 3.79 fs. Another possible error source is the measurement of the spectrum: We have performed a careful calibration of our spectrometer and have checked that wavelength-shifting the measured spectrum by ± 0.1 nm yields a deviation from our measured pulse duration of only 0.03 fs. Furthermore, the influence of noise on the spectrum was simulated by adding 1% rms gaussian noise onto the spectrum, which is significantly more than experimentally observed. We find that this only yields a 1% rms error in pulse duration. Therefore, we can conclude that these error sources play no significant role.

Chapter 5

Microstructure-Fiber Experiments

With the advent of microstructure fibers, supercontinuum generation has become possible even with nanojoule pulses directly generated by a mode-locked Ti:sapphire laser [18]. The continua generated in these fibers show some remarkable properties: they can span a whole optical octave or more, are spatially coherent, and have a brightness which exceeds the brightness of a light bulb by at least 5 orders of magnitude. These continua have already found applications in optical coherence tomography [61] and in frequency metrology, where they deliver precise octave-spanning frequency combs [22] [24]. The enormous bandwidth lead to the desire to compress these supercontinua to yield single-cycle pulses. However, the shortest pulse duration achieved so far with this approach is 25 fs [116] [117]. Here, we demonstrate compression down to as short as 5.5 fs and also discuss in depth the limitations of this technique.

It is known [118] that the spectral coherence of supercontinua generated in strongly nonlinear processes can be imperfect, and that this can inhibit the compression process, because the dispersive compressor can be adjusted only relatively slowly and thus can not be optimized for each pulse separately when the spectral phase undergoes strong fluctuations. Particularly for very broad spectra, this problem can be severe. However, it is also strongly affected by the detailed parameters of the fiber (in particular, by its dispersion) and of the initial pulses. In Section 5.3, we investigate this issue for our fibers, using numerical simulations of the pulse propagation. Also we discuss effects of the limited compressor resolution and a limitation of the SPIDER technique.

In this Chapter, we present our experiments on generation and compression of supercontinua using two different microstructure fibers. One is pumped in the normal dispersion region and has a core diameter of $2.6\text{ }\mu\text{m}$. With this fiber we were able to successfully demonstrate compression down to 5.5 fs . The other fiber has a smaller core diameter of only $1.7\text{ }\mu\text{m}$ and is pumped in the anomalous dispersion region. Using this fiber we were able to produce broader supercontinua spanning a bandwidth of more than 600 nm , but due to the above mentioned problems we have not been able to compress these supercontinua. Our simulations suggest that with today's state-of-the-art pulse compressors clean compression of these supercontinua is not possible due to the effects of coherence degradation and the limited compressor resolution.

We start this Chapter with a detailed presentation of our experimental setup. Again a spatial light modulator (SLM) is used for pulse compression and the feedback is obtained by measuring the spectral phase using a cross-correlation SPIDER setup. Section 5.2 is dedicated to our experimental results obtained with both fibers, and in Section 5.3 our numerical simulations are presented. A comparison with the experimental data shows qualitative agreement, although the simulations suggest, that pulse compression should in principle have been possible even for the $1.7\text{ }\mu\text{m}$ core diameter fiber, but at the cost of a poor pulse quality. At the end we give a discussion on the problems encountered with the smaller core diameter fiber and conclude with a comparison between the microstructure fiber and the hollow-fiber experiments.

5.1 Experimental Setup

5.1.1 Supercontinuum generation

Figure 5.1 shows our experimental setup. The seed laser is a Kerr-lens mode-locked Ti:sapphire laser in which dispersion compensation is achieved with a combination of 7 double-chirped mirrors [74] and a prism pair [69]. The laser generates 15-fs pulses with a pulse energy of 16 nJ , a center wavelength of 800 nm , and a repetition rate of 19 MHz . The relatively low repetition rate was chosen in order to obtain output pulses with a higher pulse energy, as required for achieving broad spectra in very short pieces (few millimeters) of microstructure fiber.

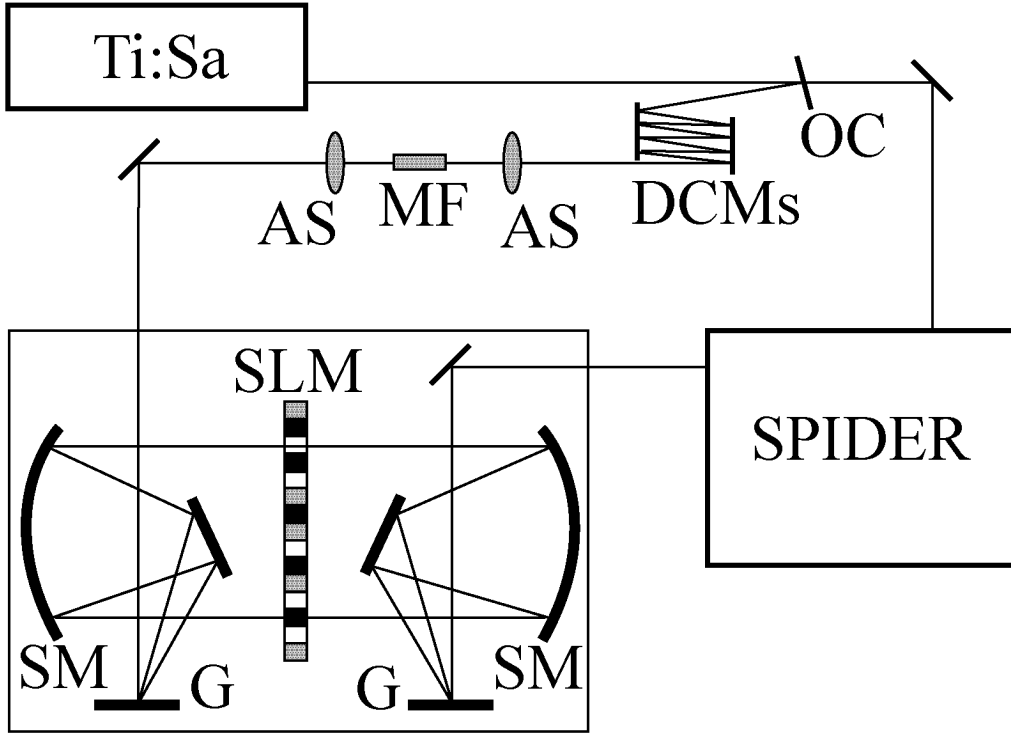


Figure 5.1: Schematic of our experimental setup: Ti:Sa, Ti:sapphire oscillator; OC, output coupler; DCMs, double chirped mirrors; AS, aspheric lens; MF, microstructure fiber; SM, spherical mirror; G, grating; SLM, spatial light modulator.

The use of such short fiber pieces has been motivated by the need to work with a limited compressor resolution: the SLM can control the spectral phase only for a discrete set of frequency components. The transmission phase should not vary by more than ≈ 1 rad between adjacent two of these spectral components. Thus, the achievable group delay, which is the frequency derivative of the spectral phase, is limited. In order to limit the group delay required for compression, we are using very short pieces of fiber, pumped with rather short initial pulses. The short initial pulse duration and the use of a fiber with normal dispersion also lead to a relatively good spectral coherence of the supercontinuum.

We use 75% of the initial pulse energy as incident power on the microstructure fiber, while 25% are split off before the fiber for use in the cross-correlation SPIDER setup (see Section 5.1.3) used for characterization of the compressed pulses. An aspheric lens with a focal length of 4.5 mm is used to couple the pulses into the 5-mm long microstructure fiber. The dispersion of the aspheric lens is precompensated with

two double-chirped mirrors (DCMs). Both ends of the fiber were cleaved at an angle of approximately 8° in order to prevent backreflections into the laser. The output beam from the fiber was collimated with another lens with a short focal length (10 mm) and a thickness of 3.9 mm, which contributes a significant amount of unwanted normal dispersion.

The microstructure fiber has a design as often used for supercontinuum generation, containing a regular hexagonal array of air holes, with the central hole missing. Effectively the central region is similar to a cylinder with a diameter of $2.6\text{ }\mu\text{m}$. Figure 2.2 in Chapter 2 shows the measured dispersion profile of this fiber.

Because of their importance for the supercontinuum coherence, we measured the power fluctuations of the transmitted pulses to be in the order of 3% rms in a 50-kHz bandwidth, while the rms fluctuations of the incident laser pulses were ≈ 4 times smaller. We explain the larger output pulse fluctuations with the beam pointing fluctuations of the laser, which affect the input coupling efficiency.

We also did some experiments with another fiber with a smaller core ($1.7\text{ }\mu\text{m}$ diameter). Due to its slightly elliptical core this fiber is polarization maintaining. Therefore, the coupling efficiency into the fiber is strongly polarization dependent. For this reason we placed the fiber in a rotational mount in order to adjust the fiber axes to the polarization of the input pulse. Usually one would not rotate the fiber itself for this purpose, but use a half-wave plate in front of the fiber, to rotate the polarization of the input pulse. We used the other approach to limit the amount of additional normal dispersion in the beam path. For this fiber, the power fluctuations of the transmitted pulses were even larger. This fiber delivered broader spectra of more than 600 nm width, but – as we will see – the shortest compressed pulses have been achieved with the other fiber.

The coupling efficiency into the fibers was estimated by comparison with numerical simulations (see below) to be $\approx 20\%$ for the fiber with the smaller core and $\approx 30\%$ for the other one. Note that it is difficult to measure the launch efficiency for a short piece of fiber where the parts launched into the core and the cladding of the fiber can not be easily separated.

5.1.2 Pulse shaper

The pulse shaper setup (see Figure 5.1), which is the same as described in Chapter 4, was designed for the broadest generated supercontinua spanning a range from ≈ 400 nm to 1050 nm. In order to obtain sufficient wavelength resolution (for sufficient group delay), we used a 640-pixel liquid crystal spatial light modulator (SLM), where the pixels are $97\text{ }\mu\text{m}$ wide and are separated by $3\text{-}\mu\text{m}$ gaps. The SLM was placed in the Fourier plane of a 4-f setup [77]. For mapping the range of 400-1050 nm onto the SLM, we used gratings with 300 lines/mm and spherical mirrors with a focal length of 300 mm. To avoid excessive astigmatism, we used plane folding mirrors next to the gratings and operated the spherical mirrors with nearly normal incidence. This proved to be very crucial for these huge bandwidth to get a collimated beam at the exit of the pulse shaper. The obtained compressor resolution is ≈ 1 nm, corresponding to a maximum group delay in the order of 340 fs. The total power throughput of the pulse shaping setup is only 15%, because the gratings introduce considerable losses over such a large bandwidth.

5.1.3 Pulse characterization and compression

After the pulse shaper the pulses are fed into the pulse characterization setup. Because of the losses introduced due to the coupling into the fiber and in the pulse shaping apparatus, the average power of the pulses at the entrance of the pulse characterization setup is only 4 mW. Due to the huge bandwidth of the supercontinua, the spectral energy density is therefore very low, making a conventional SPIDER [81, 111] measurement as it is described in Chapter 3 impossible. One would not be able to obtain a detectable SPIDER signal over the entire bandwidth of the spectrum. We therefore decided to build a cross-correlation SPIDER [114] using the laser pulse as the strongly linearly chirped pulse and feeding the continuum into the „replica“-arm. In principle the setup is the same as described in Chapter 3, except that we do not use a reflection off the glass block to generate the replicas but instead use the entire continuum beam. Due to the enormous bandwidths we used the same custom-designed beamsplitters and sum-frequency-generation (SFG) crystal as described in detail in Chapter 3.

When performing the SPIDER measurements with the broad supercontinuum generated with the $1.7\text{-}\mu\text{m}$ core diameter fiber, we noticed that strong scattered light from the shorter wavelength region of the fundamental spectrum completely overlapped

with the SPIDER signal in the spectrometer above 400 nm. We first tried to cut the shorter wavelength region of the supercontinuum by inserting a knife edge in the Fourier plane of the pulse shaping setup. However, the second diffraction order of the short wavelengths still overlapped in the Fourier plane with the long wavelengths, and its scattered light in the spectrometer was still too strong compared to the SPIDER signal. Therefore, we had to use a color filter (1 mm Schott GG 495) to cut all spectral components below 495 nm, although this meant introducing additional dispersion.

The spectral phase reconstructed from the SPIDER measurement is used as feedback to iteratively compress the pulse, as already described in Chapter 3. We start the compression by writing a flat phase onto the SLM. Then, we measure the spectral phase of the pulse using our SPIDER setup. We then control, whether the pulse is already short or not. If it is not short yet, the measured spectral phase is inverted and added to the phase currently applied to the SLM. Such iterations are repeated until the pulse does not change significantly any more. Typically, three iterations are required to obtain the shortest pulse.

5.2 Experimental Results

In this Section we present our experimental results obtained with two different microstructure fibers, where the core diameters are 2.6 μm and 1.7 μm , respectively. In both cases, the propagation length was 5 mm.

5.2.1 Microstructure fiber with 2.6 μm core diameter

For the measurements presented in this Subsection we used a 2.6- μm core diameter microstructure fiber from Crystal Fibre with a zero-dispersion wavelength of 940 nm, thus pumping in the normal dispersion region. With this fiber we were able to generate very bright and broadband spectra with excellent spatial characteristics. A typical spectrum obtained with a pulse energy of 2.7 nJ launched into the fiber, ranging from 520 nm and 950 nm, is shown in Figure 5.2.

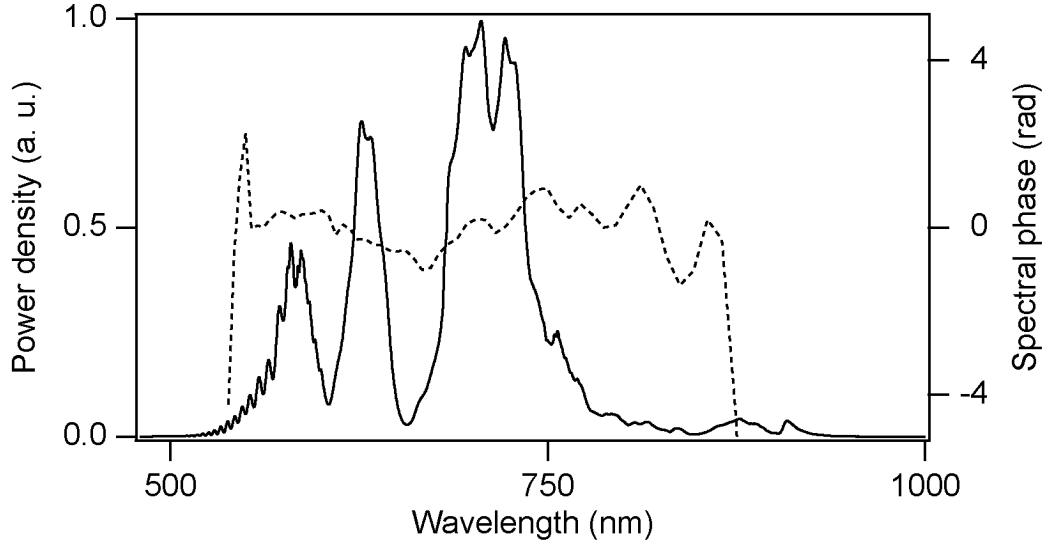


Figure 5.2: Solid curve: experimentally measured output spectrum of the 2.6 μm core diameter fiber. The dashed curve depicts the reconstructed spectral phase.

Due to the fact, that the spectrum is not octave-spanning, we did not have to use a color glass filter to suppress the shorter wavelengths (see Section 5.1.3). With these spectra, we experienced no difficulties concerning the SPIDER measurements: the recorded interferogram showed a good fringe visibility as shown in Figure 5.3, so that a reliable reconstruction of the spectral phase of the pulses was possible.

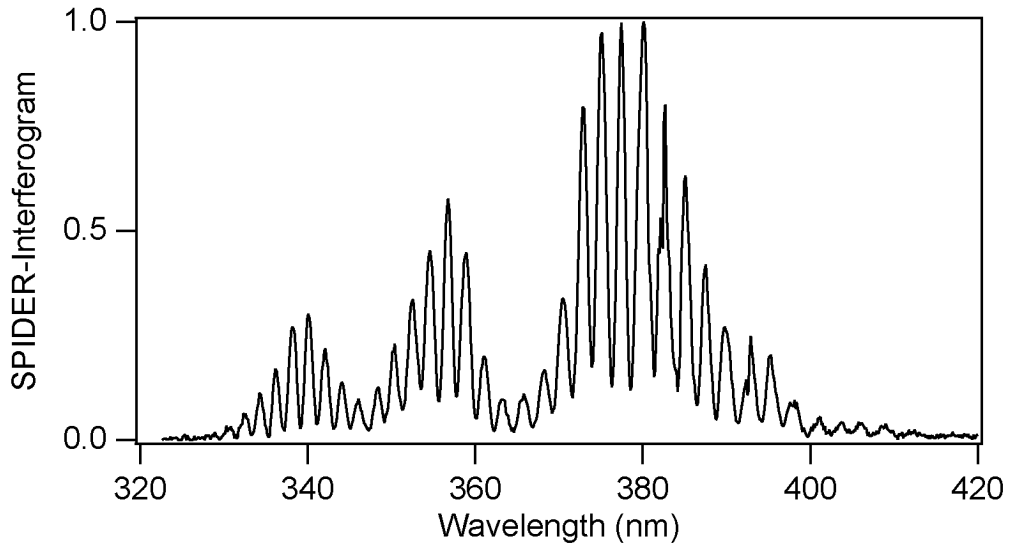


Figure 5.3: Recorded SPIDER-interferogram showing a good fringe visibility.

With this fiber we were able to demonstrate successful compression to a full width at half maximum (FWHM) pulse duration of 5.5 fs (see Figure 5.4). As can be seen in Figure 5.2, the spectral phase is flat over the full spectrum, except for the outer parts, where the spectral energy density is too low for reliable reconstruction of the spectral phase. This explains why the pulses are slightly longer than the theoretical transform-limited pulse duration of 4.8 fs for the full spectrum, or 5.3 fs for the spectrum between 545 nm and 970 nm. This spectral range corresponds to the bandwidth over which the reconstruction of the spectral phase was possible. To the best of our knowledge, these are the shortest pulses ever generated using a microstructure fiber.

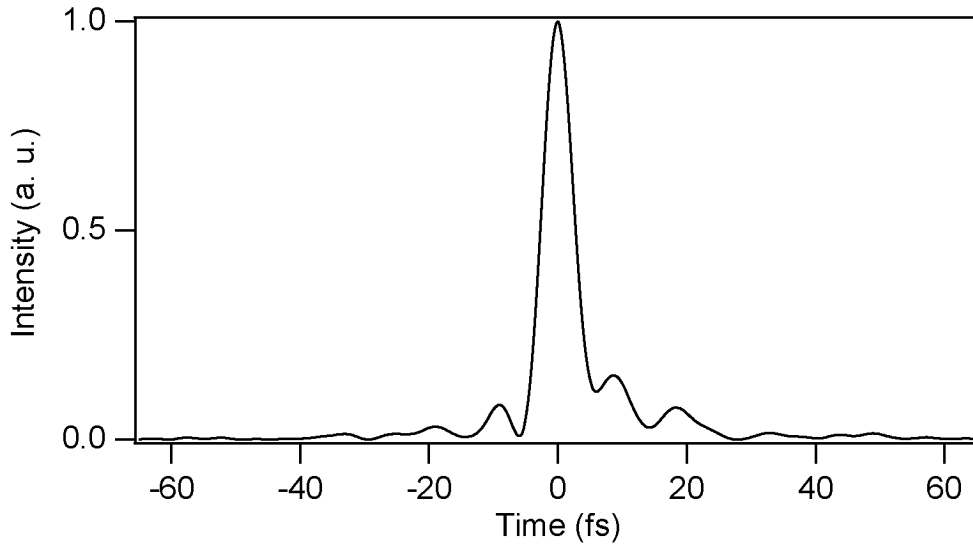


Figure 5.4: Reconstructed temporal pulse profile showing a FWHM pulse duration of 5.5 fs.

5.2.2 Microstructure fiber with 1.7 μm core diameter

For the generation of octave-spanning supercontinua, we used a polarization-maintaining microstructure fiber from Crystal Fibre with a core diameter of only 1.7 μm and a zero-dispersion wavelength of 665 nm, thus pumping in the anomalous dispersion region. With this fiber we were able to produce spectra spanning from 400 nm to more than 1000 nm. On the long wavelength side the measurement was limited by the detector sensitivity (Si). A typical spectrum measured without the color glass filter is shown in Figure 5.5. The spectrum is strongly modulated and shows sharp spectral features in the wavelength range of the input laser beam. We believe these features to result from

interferences between the core and the cladding modes, although it is not clear why this effect was observed only with the smaller core fiber.

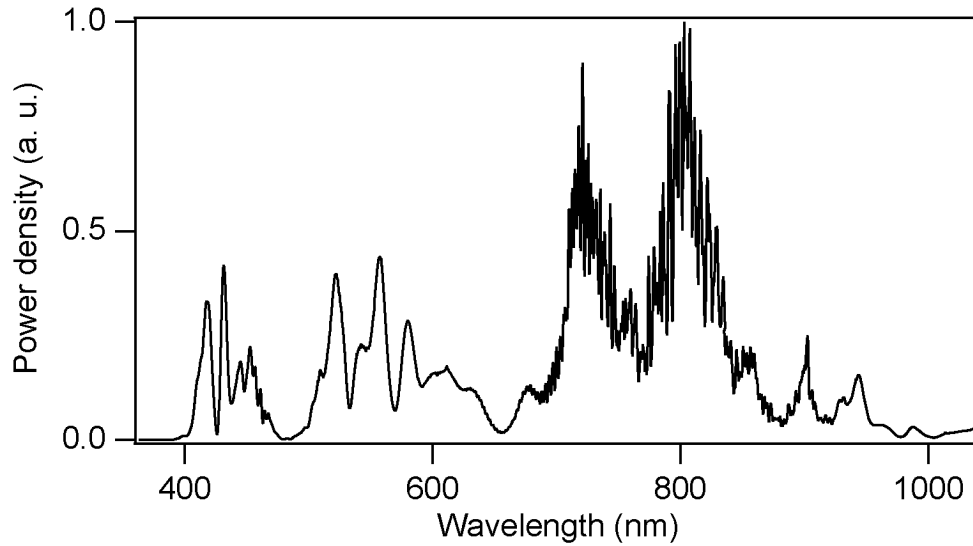


Figure 5.5: Experimentally measured supercontinuum from the 1.7 μm core diameter fiber exhibiting strong modulations and interferences in the spectral region of the laser beam (700 nm to 900 nm).

We encountered several problems related to the characterization of these strongly structured broad supercontinua. As already mentioned for the 2.6 μm fiber, the spectral energy density in the wings of the spectrum was too low for the detection of an upconversion signal even with the crosscorrelation SPIDER setup. With the much broader spectra from the 1.7 μm core fiber, this problem was even more severe. While the latter problem could possibly be overcome by using pulses with higher energies, the mentioned sharp features on the spectra represent a more fundamental problem: they destroy the fringe visibility in the SPIDER interferogram (shown in Figure 5.6) and thus inhibit the correct reconstruction of the spectral phase.

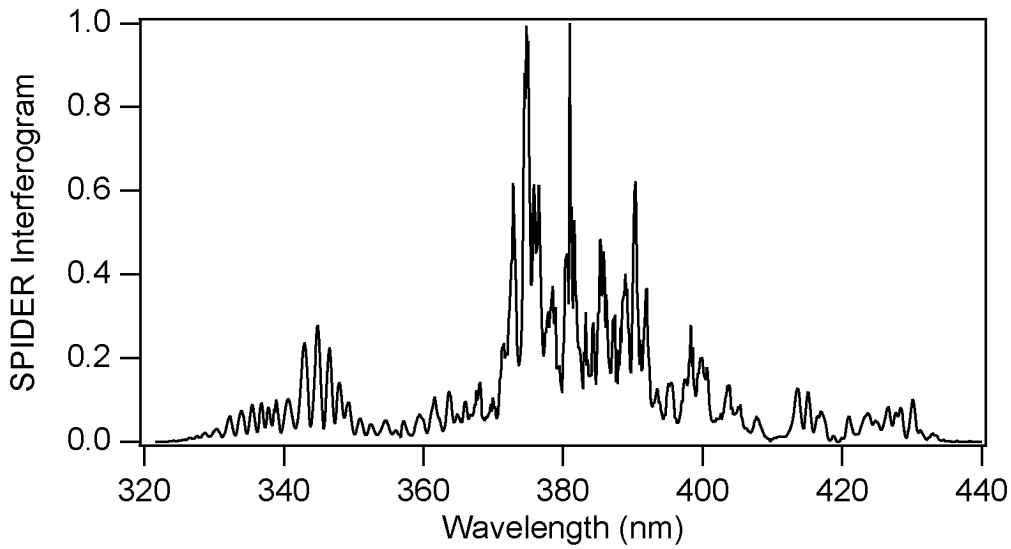


Figure 5.6: Typical recorded SPIDER Interferogram obtained with the output of the 1.7 μm core diameter fiber.

5.3 Theoretical Considerations

In this Section, we investigate two important limiting factors for the dispersive compression of supercontinua: the limited spectral coherence, and the effect of the limited compressor resolution.

The probably most fundamental limitation for supercontinuum compression is the limited coherence. The broadest spectra are often achieved when the fiber dispersion is anomalous in a large spectral range and the pulse intensity is high, as is possible with small mode areas. However, the launched pulses then correspond to solitons with very high soliton order, which subsequently break up into numerous weaker pulses. The latter can partly propagate as solitons and partly as dispersive radiation. The highly nonlinear nature of the involved processes can be extremely sensitive to the input pulse parameters [68] [67] [119] [120]. As a result, the generated output can vary significantly in spectral structure and spectral phase from pulse to pulse, even if the input pulses are at the quantum noise limit. With the large low-frequency excess noise of typical mode-locked lasers, the coherence of the generated supercontinuum can become so poor that

effective compression is not possible, because the spectral phase would have to be separately optimized for each single pulse.

However, the severity of the coherence issue strongly depends on a number of parameters, such as the fiber dispersion, fiber length, and the initial pulse duration. In particular, the normal dispersion regime tends to lead to better coherence, although the achieved bandwidth is often smaller [118]. Also, the coherence is favored by the use of short initial pulses [118] [121] [122]. As a tentative explanation, the coherence can be poor for long pump pulses because then the Raman gain occurs outside the initial pulse bandwidth and thus generates new spectral components by amplifying quantum noise. In contrast, for pump pulses with durations well below 100 fs the Raman gain only acts on already existing spectral components and therefore does not introduce that much noise. Finally, it has been found [123] that often the coherence is good below a certain threshold for the pulse energy, where already a broad spectral width is achieved, while the coherence rapidly degrades for higher pulse energies. Of course, this threshold depends on the fiber length.

Our experimental result, obtained in the normal dispersion regime with short initial pulses and a short fiber piece of only 5 mm length, shows that compression down to 5.5 fs is possible. In the following, we quantitatively investigate the coherence and other issues in the regime of our experiment. Note that calculations with the actual experimental parameters are required for the optimization of the setup and the interpretation of the obtained data. Conclusions from investigations in other parameter ranges can usually not be used, since the behavior differs very much between different parameter ranges.

5.3.1 Simulation basics

We numerically simulated the propagation of pulses in the microstructure fibers using a generalized scalar propagation equation (including fiber losses) suitable for use in studying broadband pulse evolution. This propagation equation (Equation 2.15) was derived in Chapter 2 and has also been used by other authors in the field [65, 118]. It models the effects of the nonlinear propagation, taking into account the effects of dispersion, self-phase modulation, self-steepening, four-wave mixing, and intra-pulse Raman scattering. The response function $R(t) = (1 - f_R)\delta(t) + f_R h_R(t)$ includes both the in-

stantaneous and delayed nonlinear responses of the fiber, where $f_R = 0.18$ is the fractional contribution of the Raman delayed response. For h_R , we used the experimentally determined Raman response of silica [33]. To solve the propagation equation, we used a standard split-step Fourier algorithm treating dispersion in the frequency domain and the nonlinearity in the time domain, apart from the temporal derivative for the self-steepening effect, which was evaluated using Fourier transforms.

5.3.2 Calculation of coherence

Recently a modified Young two-source experiment was used to characterize the coherence of supercontinua generated in bulk [23]. Here, two spatially separated and independently generated supercontinua are superposed to yield a polychromatic far-field interference pattern. The spectral resolution of this pattern reveals distinct fringes at each wavelength in the spectrum, with the wavelength dependence of the fringe visibility providing a rigorous measure of the local coherence properties. This is due to the fact that it is directly related to the modulus of the complex degree of (mutual) coherence between the independent supercontinua. We use this measure of coherence to examine numerically the coherence properties of the supercontinua generated in our fibers.

In particular, the simulations have been performed for e.g. 100 initial pulses which differ in intensity due to some initial intensity noise with Gaussian probability distribution and an rms value of a few percent of the average intensity. Note that due to the relatively long measurement times (e.g. several seconds for a SPIDER trace) the low-frequency classical noise is important, and this is far above the shot noise level.

As our simulation show (see later in this Section) the generated supercontinua are affected by spectral and temporal jitter. This jitter is associated with coherence degradation caused by severe fluctuations in the spectral phase at each wavelength. To study this coherence degradation numerically we quantified it by means of the modulus of the complex degree of first-order coherence calculated over a finite bandwidth at each wavelength in the supercontinuum:

$$|g_{12}^{(1)}(\lambda, t_1 - t_2)| = \left| \frac{\langle E_1^*(\lambda, t_1) E_2(\lambda, t_2) \rangle}{\left[\langle |E_1(\lambda, t_1)|^2 \rangle \langle |E_2(\lambda, t_2)|^2 \rangle \right]^{1/2}} \right| \quad (5.1)$$

The angle brackets denote an ensemble average over independently generated supercontinuum pairs $[E_1(\lambda, t), E_2(\lambda, t)]$, and t is the time measured at the resolution time scale of the spectrometer that has been used to resolve the spectra. Because we are interested mainly in the wavelength dependence of the coherence, we calculate $|g_{12}^{(1)}|$ at $t_1 - t_2 = 0$, which, in practice, would correspond to measuring the fringe visibility at the center of the fringe pattern in a Young two-source experiment [118].

5.3.3 Results for 2.6 μm core diameter fiber and comparison with experiment

Figure 5.7 shows a simulation with 100 runs for 15 fs input pulses, a center wavelength of 790 nm, an average power of 50 mW coupled into the fiber at a repetition rate of 19 MHz, and power fluctuations of 5% rms. The spectral amplitudes for all single runs as well as the average spectral amplitude is shown. Despite the power fluctuations on the input pulses, the overall shape of the generated spectra is the same and only relatively small variations in the spectral amplitudes can be observed. In addition, the degree of coherence (see top of Figure 5.7), calculated as described above, is found to be good in all spectral regions with significant spectral intensity. We like to note that the simulations can give a useful estimate for the coherence even if the spectral details are not all fully reproduced.

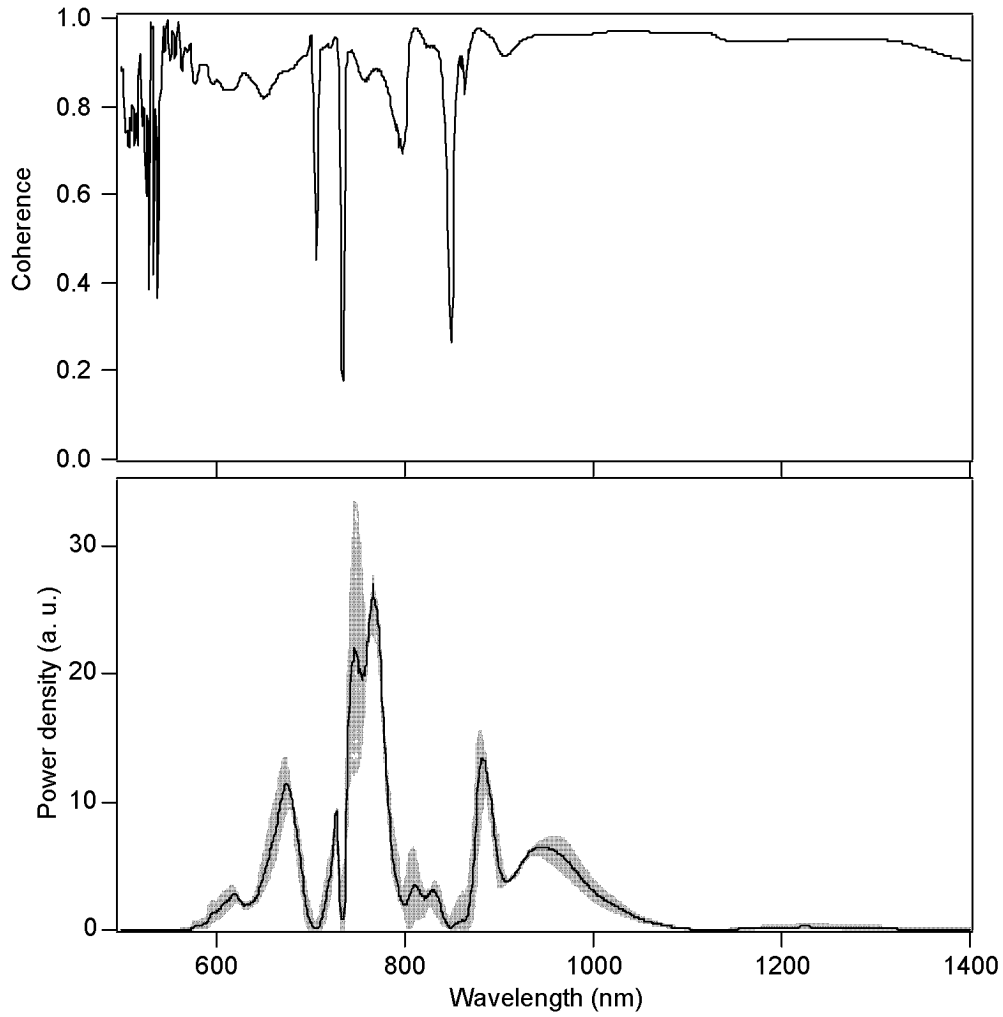


Figure 5.7: Simulations for the 2.6 μm core diameter fiber: Bottom: the light grey curves show an ensemble of 100 individual spectra, the solid black curve depicts the averaged spectrum. Top: Calculated degree of coherence for these spectra.

Using these data, we simulated the pulse compression, where the compressor parameters were set according to the averaged spectral phase of the pulses, and the spectral intensity for wavelengths >950 nm was suppressed as in the experiments. The spectral phase was corrected only with a finite compressor resolution similar to the experiment. The simulation result demonstrated that the compression is not significantly affected by the limited coherence and the compressor resolution: the obtained FWHM pulse duration is on average 4.9 fs (see Figure 5.8), close to the transform limit of 4.8 fs for the averaged spectrum. This agrees with the successful experimental compression described in Section 5.2.1.

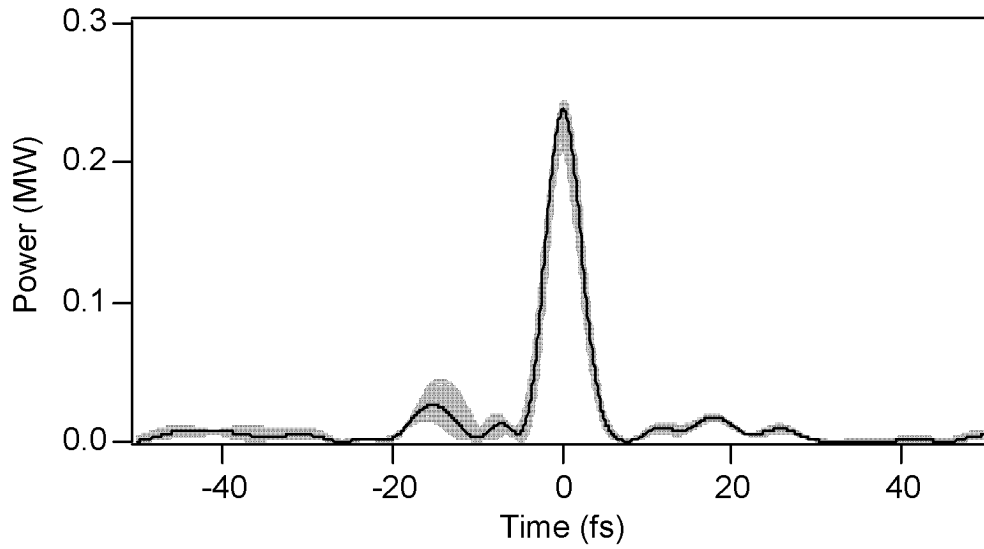


Figure 5.8: Calculation of compressed pulses for the 2.6 μm core diameter fiber: the light grey curves show 100 individual pulses compressed with the averaged spectral phase, the black solid curve is the average of these 100 compressed pulses.

Comparing the measured spectrum with the numerically simulated spectra (see Figure 5.2 and Figure 5.7) shows that both spectra span a bandwidth of more than 400 nm and qualitatively agree concerning their shapes, although they are slightly frequency-shifted. The long wavelength tail from 950 nm up to 1400 nm in the simulated spectra is suppressed in the measured one, because the spectral sensitivity of our CCD-camera ranges from 180 nm to 1000 nm. Exact quantitative agreement cannot be expected due to uncertainties in the dispersion data (including possible variations along the fiber length) and the properties of the initial pulses, keeping in mind the sensitivity of the results on such parameters.

5.3.4 Results for 1.7 μm core diameter fiber and comparison with experiment

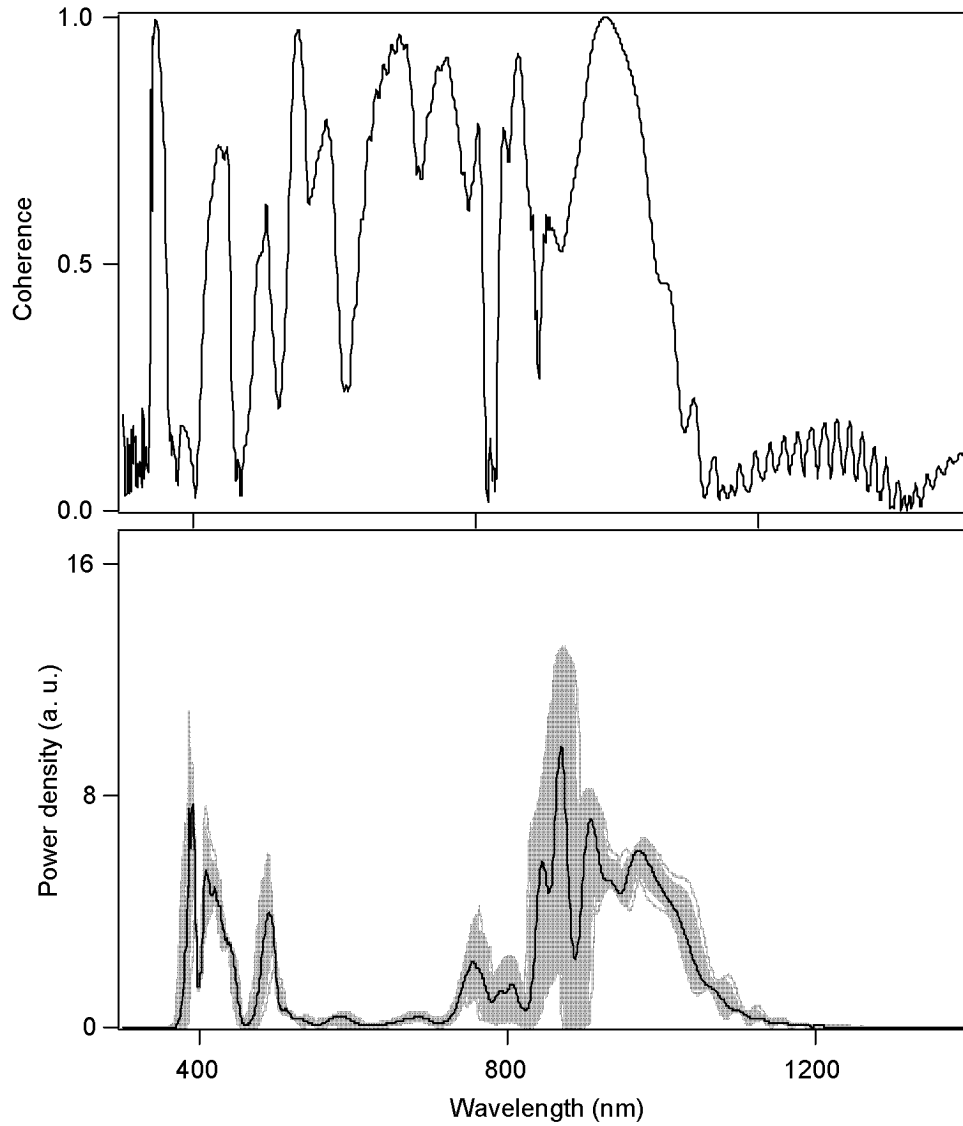


Figure 5.9: Simulations for the 1.7 μm core diameter fiber: Bottom: the light grey curves show an ensemble of 100 individual spectra, the solid black curve depicts the averaged spectrum. Top: Calculated degree of coherence for these spectra.

We did similar simulations for the fiber with a smaller core diameter of 1.7 μm , where the obtained spectra were significantly broader. Figure 5.9 shows an ensemble of 100 spectra and the average spectrum as solid curve obtained with the same input pulse parameters as used for the 2.6 μm core diameter fiber. Compared to the simulation result

for the 2.6 μm core diameter fiber the spectral amplitudes show much stronger fluctuations for the same input power fluctuations, especially in the 800 nm to 900 nm region. Here, the calculated coherence (top of Figure 5.9) is significantly worse, especially in regions with a large amount of spectral energy.

The simulation of the compression (under the same conditions as above, except that all wavelengths above 1000 nm were suppressed as in the experiment) showed that although the average duration of the compressed pulses is still close to the transform limit, the amount of power in the temporal side lobes has significantly increased compared to the theoretical result for the compressed average pulse (see Figure 5.10). Also we found that the limited compressor resolution has some degrading effect in this case. Despite these problems, the simulations suggest that in principle one may obtain compressed pulses with sub-2 fs average duration, although only with poor pulse quality. Even this was not achieved in the experiment, probably due to the influence of cladding modes as explained in Section 5.2.2.

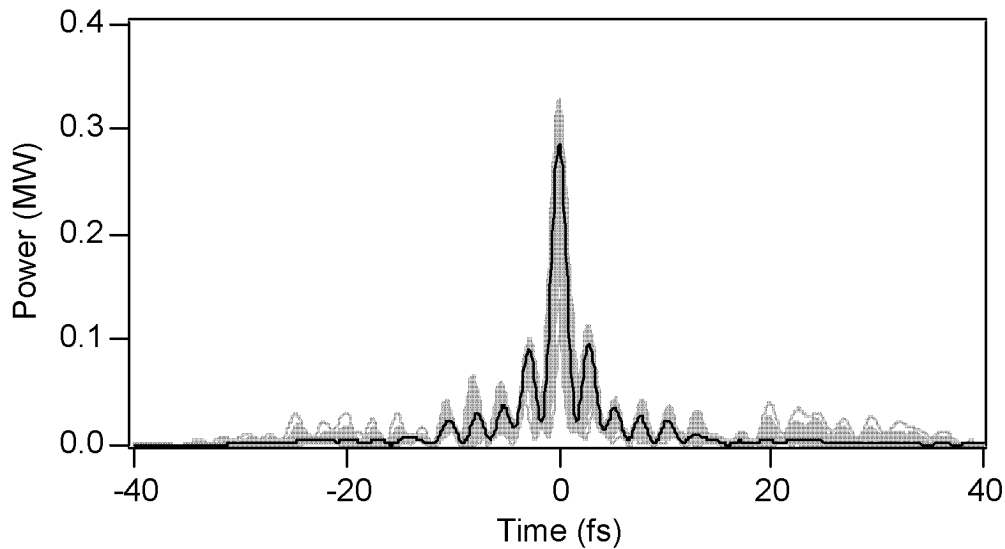


Figure 5.10: Calculation of compressed pulses from the 1.7 μm core diameter fiber: the light grey curves show 100 individual pulses compressed with the averaged spectral phase, the black solid curve is the average of these 100 compressed pulses.

Compared to the measured supercontinua (see Figure 5.5) the bandwidth is roughly the same except for the long wavelength region, which can not be detected by our CCD anymore. Another difference is that the measured spectra have more spectral

energy in the 700 nm to 800 nm region and that it is this wavelength region, where the sharp spectral features occur. An explanation for this difference is the interference with the cladding modes, which can not be eliminated over such a short fiber length.

5.4 Discussion

Following the presentation of the experimental and theoretical results, we dedicate this Section to the discussion of the main limitations for the compression of a microstructure fiber supercontinuum to single-cycle pulses.

5.4.1 Coherence degradation due to power fluctuations

It has been suggested that a limiting factor for successful compression of microstructure fiber supercontinua could be the coherence degradation of the supercontinuum due to quantum noise only. As numerical simulations by J. Dudley [118] show, this should not be a problem for short input laser pulses. Therefore, we started our compression experiment by launching 15 fs short pulses into the microstructure fiber.

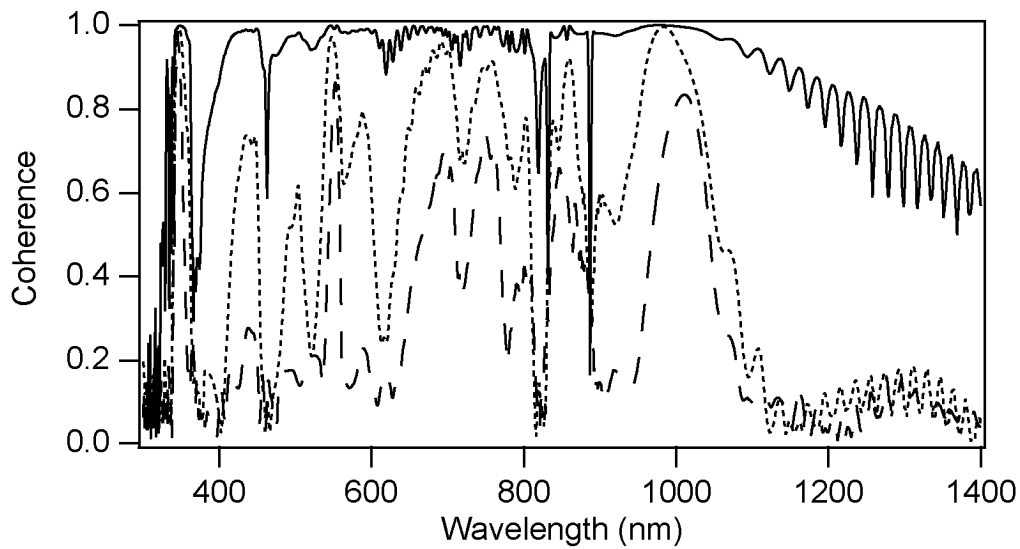


Figure 5.11: Calculated coherence (for the 1.7 μm fiber) for an ensemble of 100 pulses assuming three different power fluctuations: solid curve: 1% rms, dotted curve: 5% rms, and dashed curve: 10% rms.

Our simulations show that for increasing power fluctuations the coherence is gradually degrading. This is shown in Figure 5.11 for the 1.7 μm core diameter fiber, where the coherence was calculated for three different power fluctuations on the input pulse with the same parameters as used in Section 5.3.4. As can be seen the coherence degradation due to power fluctuations is dramatic for this fiber. For comparison, we also calculated the degree of coherence for the same power fluctuations for the 2.6 μm core diameter fiber. Figure 5.12 shows the result for the same parameters as used in Subsection 5.3.3. In contrast to the 1.7 μm core diameter fiber, the coherence degradation in this fiber is not that severe.

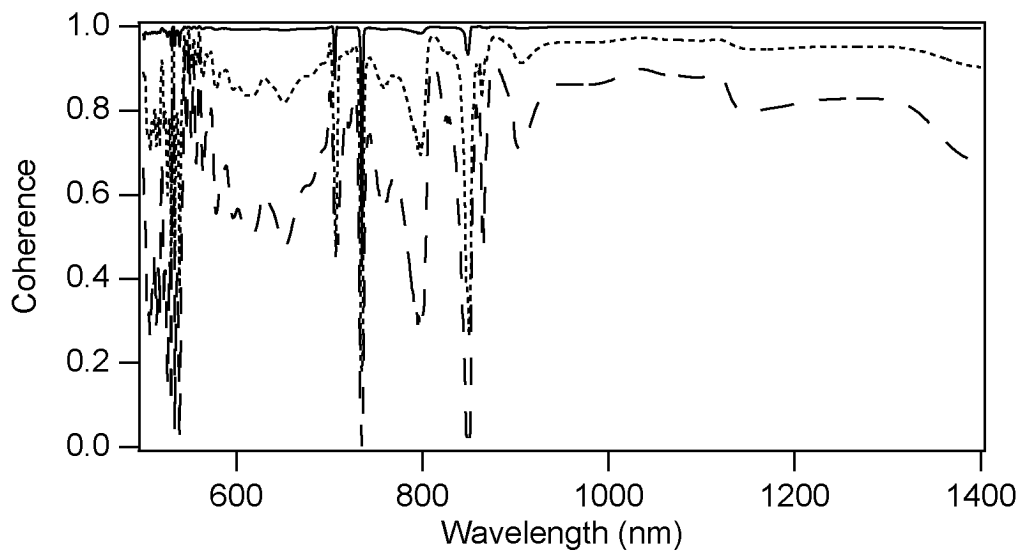


Figure 5.12: Calculated coherence (for the 2.6 μm fiber) for an ensemble of 100 pulses assuming three different power fluctuations: solid curve: 1% rms, dotted curve: 5% rms, and dashed curve: 10% rms.

As we measured power fluctuations of 3% rms after the fiber due to beam pointing instabilities of the oscillator (see Subsection 5.1.1), we included this in our simulation and found that for the 2.6 μm fiber the coherence is still good enough to allow for successful compression of the pulses. As described in Section 5.2.1 we proved experimentally that compression to 5.5 fs using a 2.6 μm core diameter microstructure fiber is possible. For the 1.7 μm core diameter fiber we find that for some wavelengths the coherence is significantly degraded and that although pulse compression should in principle still be possible, this coherence degradation is too big to allow for the com-

pression of a clean ultrashort pulse. To resolve this problem one might think about trying to position stabilize the input laser beam.

5.4.2 Cladding modes due to short fibers

The problems we encountered with the 1.7 μm core diameter microstructure fiber, namely the sharp spectral features in the spectrum as well as in the SPIDER-interferogram due to interferences with the cladding modes could be resolved by using a longer piece of fiber. The advantage of using longer fiber pieces would be the possibility of reducing or even completely stripping off the cladding modes, so that smooth spectra and interferograms could be recorded and thus the spectral phase could be unambiguously determined. But this would only be possible at the expense of more dispersion introduced by propagating through a longer piece of fiber. As soon as the dispersion exceeds a certain limit, the limited compressor resolution of the liquid crystal SLM makes a successful compression impossible [77]. If we take into account that the dispersion of the output coupling lens has to be compensated for as well and that the compression has to be achieved by the SLM only, we find experimentally that the maximum fiber length is about 5 mm.

To avoid the additional dispersion introduced by the output coupling lens, one could replace this lens by a spherical mirror or a paraboloid. Since the divergence of the output beam is enormous, spherical optics with short focal lengths are needed in order to avoid using optics with large dimensions. However, spherical optics with short focal lengths introduce strong astigmatism and aberrations. Even if one would use large-scale optics with longer focal lengths, the collimated beam would have an enormous diameter. Thus, the use of a reflective beam expander (or “impander”) would be necessary in order to obtain a collimated beam with a reasonable diameter. This however is complicated, introduces wave front errors and reduces the overall transmission even further.

We like to note that although in principle one could remove the cladding modes e.g. using a mode cleaner (with focusing optics and pinhole), such operations are problematic when applied to these extremely broad spectra, which are very sensitive to effects like chromatic aberrations and add additional dispersion. Additionally, the enormous difference in spot sizes for blue and near-infrared light limits the applicability of a mode cleaner for such huge bandwidths.

5.4.3 SPIDER problem for structured spectra

As a result of the interferences between the core and the cladding modes in the 1.7 μm core diameter microstructure fiber, we observed the same sharp spectral features in the recorded SPIDER-interferogram. These sharp „spikes“ destroy the fringe visibility and thus inhibit the correct reconstruction of the spectral phase.

Even without interference from cladding modes, the spectra are strongly structured when the supercontinuum generation is optimized for large bandwidth. Particularly the spectral regions with nearly vanishing spectral intensity cause problems for the reconstruction of the phase in the SPIDER method. If the SPIDER interferogram is zero for some wavelengths, the spectral phase of these wavelengths is not defined anymore and thus the reconstruction fails.

Probably for these reasons, attempts to compress the broader spectra from the fiber with the smaller core were not successful. This shows that the best fiber for pulse compression is not necessarily the one generating the broadest spectra, and this holds not only due to the issue of spectral coherence.

5.5 Conclusions

In conclusion, we have demonstrated pulse compression down to 5.5 fs from a supercontinuum generated in a microstructure fiber. The compression was achieved with iterative optimization of the setting of a liquid crystal spatial light modulator. The pulses were characterized by performing a cross-correlation SPIDER measurement.

To our best knowledge, the obtained pulse duration is by far the shortest demonstrated with this method. Key points were to use a rather short piece of fiber (5 mm), to start with short (15 fs) pump pulses, and to choose a fiber with normal dispersion, where the spectral coherence is better.

We have discussed various limitations of the general method and of the particular experimental results. For the obtained compression results, we could not use the full generated spectrum because some parts had too low spectral intensity for SPIDER characterization. For compression of broader spectra, more pulse energy would be

needed. Even with higher pulse energies, the SPIDER characterization can be invalidated by strongly modulated spectral structures, particularly if spectral regions with low power density exist, or if cladding modes destroy the fringe visibility. Finally, the spectral coherence tends to get worse for broader spectra, although this strongly depends on the chosen regime of fiber dispersion, initial pulse duration, etc. The coherence can greatly suffer from classical excess noise in the initial pulses, including their beam pointing instability which affects the launch efficiency. However, we have shown that even with significant classical excess noise the limited spectral coherence is not necessarily the most important limiting factor for pulse compression.

An alternative method for supercontinuum generation is based on propagation in hollow fibers [15]. Compared to microstructure fibers, much higher pulse energies in the order of 1 mJ are required for strong spectral broadening in hollow fibers. This makes it necessary to use amplified pulses from an amplifier, operating at a repetition rate of e.g. 1 kHz. Of course, the resulting pulse energies are correspondingly higher, making it easier to do a precise SPIDER characterization. The spectral phase of the output of a hollow fiber was investigated with a single-shot SPIDER technique and was found to be very stable [113]. Dispersive compression of such pulses with the same pulse shaper has allowed the generation of sub-4-fs pulses [108].

Compared to hollow fiber compression, the compression of microstructure fiber supercontinua has the advantage of being possible with much lower pulse energies (well below 100 nJ) and therefore at the full laser repetition rate. Despite a number of challenges, which included more than only the problem of limited spectral coherence, we have demonstrated the generation of 5.5-fs pulses with this technique.

Chapter 6

Conclusion and Outlook

In this thesis, the generation and compression of supercontinua using two different techniques has been studied experimentally. Numerical simulations have been performed for one of these techniques supporting our experimental observation, that compression is limited by a number of factors in this case. The enormous bandwidths spanning up to 600 nm made it necessary to use compression and pulse characterization schemes, that are capable of handling these bandwidths. Therefore, we employed an optimized implementation of the pulse compressor setup consisting of a 640-pixel spatial light modulator in the Fourier plane of a 4-f setup. We characterized the pulses with a broadband, low-dispersion SPIDER-setup designed for sub-10 fs pulses [81]. This setup was further improved by using custom designed ultrabroadband beamsplitters and 30 μm thick, type-II BBO crystal ensuring a broad enough conversion bandwidth for SFG. Iterative compression of the pulses is achieved by using the measured spectral phase as feedback for the SLM.

With the development of microstructure fibers, it became possible to generate supercontinua spanning more than an optical octave even with nanojoule pulses from an oscillator. We therefore investigated supercontinuum generation with two such fibers exhibiting different dispersion properties. One fiber, having a core diameter of 2.6 μm , was pumped in the normal dispersion regime, which allowed for the production of relatively stable supercontinua. With this fiber, we achieved pulse compression to 5.5 fs pulses. These pulses are the shortest pulses ever obtained using a microstructure fiber. The second fiber had a core diameter of 1.7 μm and was pumped in the anomalous dispersion regime. Using this fiber, we were able to generate broad supercontinua spanning

a bandwidth of more than 600 nm, but we have not been able to show successful compression in this case. It has been predicted that supercontinua generated in this regime exhibit a coherence degradation which limits their compressibility [118]. We therefore performed numerical simulations on the propagation through microstructure fibers including a calculation of the coherence and taking the limited compressor resolution of the SLM into account. These simulations show that the coherence of the supercontinua generated in the normal dispersion regime is still good enough to achieve a clean compression. This is in excellent agreement with our experimentally generated 5.5 fs pulses. For the other fiber, however, the simulations show that the coherence degradation and the limited compressor resolution would in principle still allow for a compression of these huge supercontinua to sub-2-fs pulses, but only with a poor pulse quality. We tentatively attribute the fact that we did not even arrive at this poor compression to a limitation of the SPIDER technique. The supercontinua generated in the anomalous dispersion regime showed strong spectral features, which were translated onto the SPIDER-signal. This had a detrimental impact on the fringe visibility making a correct reconstruction of the spectral phase impossible.

Our simulations showed that power fluctuations of a few percent rms induced by input laser beam pointing instabilities are responsible for the coherence degradation of the generated supercontinua. To overcome this effect one could try to stabilize the position of the input laser beam to the fiber entrance. Without this one would need a pulse compressor allowing for the separate compression of each single pulse, which is not possible with today's state-of-the-art pulse compressors. Even if the coherence of the supercontinua could be improved by reducing the power fluctuations, the finite compressor resolution will prevent clean compression of these spectra.

The very low pulse energies on the order of 0.2 nJ of the generated pulses will limit their usefulness for future applications.

In a second approach we used amplified pulses with mJ pulse energies at a repetition rate of 1 kHz to generate broad supercontinua using two cascaded hollow-core fibers filled with Ar. Previous single-shot measurements on phase fluctuations in hollow fibers showed that the spectral phase of these supercontinua is very stable and constant for several hours [113]. With this technique we were able to demonstrate successful compression to 3.8 fs pulses with an energy of 15 μ J using only the SLM for dispersion compensation. These pulses are among the shortest pulses ever generated in

the visible and near-infrared spectral region [19, 31, 108]. Compared to these other pulses with similar durations, our pulses have more than an order of magnitude higher pulse energies.

Since we could not use the full bandwidth of our generated supercontinua for pulse compression because the spectral energy in the wings was too low to obtain a detectable SPIDER-signal, we believe that by using a cross-correlation SPIDER setup even broader spectra can be compressed using our approach, thus yielding even shorter pulses.

Such high-peak-power light pulses in the single-cycle regime are especially interesting for application in higher-order harmonic generation (HHG). CEO-stabilizing these pulses allows to make sure, that exactly one cycle of the electric field is above the threshold for generating higher harmonics in the cut-off region. This is the precondition for the generation of single attosecond pulses [26].

Another potential application of these pulses is the investigation of various nonlinear processes, in which the absolute phase of a pulse plays a relevant role [25].

References

1. "The Holy Bible," Genesis 9:13
2. R. Alfano, *The supercontinuum laser source* (Springer, Berlin, 1989)
3. R. R. Alfano, and S. L. Shapiro, "Emission in the region 4000 to 7000 Å via four-photon coupling in glass," *Phys. Rev. Lett.* **24**, 584 (1970).
4. R. R. Alfano, and S. L. Shapiro, "Observation of self-phase-modulation and small-scale filaments in crystals and glasses," *Phys. Rev. Lett.* **24**, 592 (1970).
5. W. Yu, R. R. Alfano, C. L. Sam, and R. J. Seymour, "Spectral broadening of picosecond 1.06 μm pulse in KBr," *Opt. Comm.* **14**, 344 (1975).
6. W. Werncke, A. Lau, M. Pfeiffer, K. Lenz, H.-J. Weigmann, and C. D. Thuy, "An anomalous frequency broadening in water," *Opt. Comm.* **4**, 413 (1972).
7. A. Penzkofer, A. Laubereau, and W. Kaiser, "Stimulated short-wave radiation due to single-frequency resonances of χ^3 ," *Phys. Rev. Lett.* **31**, 863 (1973).
8. W. L. Smith, P. Liu, and N. Bloembergen, "Superbroadening in H₂O and D₂O by self-focused picosecond pulses from a YAlG:Nd laser," *Phys. Rev. A* **15**, 2396 (1977).
9. R. L. Fork, C. V. Shank, C. Hirlimann, R. Yen, and W. J. Tomlinson, "Femtosecond white-light continuum pulses," *Opt. Lett.* **8**, 1 (1983).
10. P. B. Corkum, C. Rolland, and T. Srinivasan-Rao, "Supercontinuum generation in gases," *Phys. Rev. Lett.* **57**, 2268 (1986).
11. V. Francois, F. A. Ilkov, and S. L. Chin, "Experimental study of the supercontinuum spectral width evolution in CO₂ gas," *Opt. Comm.* **99**, 241 (1993).
12. J. Kasparian, R. Sauerbrey, D. Mondelain, S. Niedermeier, J. Yu, J.-P. Wolf, Y.-B. André, M. Franco, B. Prade, S. Tzortzakis, A. Mysyrowicz, M. Rodriguez, H. Wille, and L. Wöste, "Infrared extension of the supercontinuum generated by femtosecond terawatt laser pulses propagating in the atmosphere," *Opt. Lett.* **25**, 1397 (2000).
13. C. Lin, and R. H. Stolen, "New nanosecond continuum for excited-state spectroscopy," *Appl. Phys. Lett.* **28**, 216 (1976).
14. P. L. Baldeck, and R. R. Alfano, "Intensity effects on the stimulated four photon spectra generated by picosecond pulses in optical fibers," *J. Lightwave Technol.* **5**, 1712 (1987).
15. M. Nisoli, S. D. Silvestri, and O. Svelto, "Generation of high energy 10 fs pulses by a new pulse compression technique," *Appl. Phys. Lett.* **68**, 2793 (1996).
16. P. C. Becker, H. L. Fragnito, R. L. Fork, F. A. Beisser, and C. V. Shank, "Generation of tunable 9 femtosecond optical pulses in the near infrared," *Appl. Phys. Lett.* **54**, 411 (1989).

17. R. W. Schoenlein, J.-Y. Bigot, M. T. Portella, and C. V. Shank, "Generation of blue-green 10 fs pulses using an excimer pumped dye amplifier," *Appl. Phys. Lett.* **58**, 801 (1991).
18. J. K. Ranka, R. S. Windeler, and A. J. Stentz, "Visible continuum generation in air-silica microstructure optical fibers with anomalous dispersion at 800 nm," *Opt. Lett.* **25**, 25 (2000).
19. K. Yamane, Z. Zhang, K. Oka, R. Morita, M. Yamashita, and A. Suguro, "Optical pulse compression to 3.4 fs in the monocycle region by feedback phase compensation," *Opt. Lett.* **28**, 2258 (2003).
20. M. Nisoli, G. Sansone, S. Stagira, S. De Silvestri, O. Svelto, C. Vozzi, "Ultrabroadband continuum generation by hollow fiber cascading," *Appl. Phys. B* **75**, 601 (2002).
21. D. J. Jones, S. A. Diddams, J. K. Ranka, A. Stentz, R. S. Windeler, J. L. Hall, and S. T. Cundiff, "Carrier-envelope phase control of femtosecond mode-locked lasers and direct optical frequency synthesis," *Science* **288**, 635 (2000).
22. S. A. Diddams, D. J. Jones, J. Ye, S. Cundiff, J. L. Hall, J. K. Ranka, R. S. Windeler, R. Holzwarth, T. Udem, and T. W. Hänsch, "Direct link between microwave and optical frequencies with a 300 THz femtosecond laser comb," *Phys. Rev. Lett.* **84**, 5102 (2000).
23. M. Bellini, and T. W. Hänsch, "Phase-locked white-light continuum pulses: toward a universal optical frequency-comb synthesizer," *Opt. Lett.* **25**, 1049 (2000).
24. R. Holzwarth, T. Udem, T. W. Hänsch, J. C. Knight, W. J. Wadsworth, and P. S. J. Russell, "Optical frequency synthesizer for precision spectroscopy," *Phys. Rev. Lett.* **85**, 2264 (2000).
25. G. G. Paulus, F. Grasborn, H. Walther, P. Villoresi, M. Nisoli, S. Stagira, E. Priori, and S. D. Silvestri, "Absolute-phase phenomena in photoionization with few-cycle laser pulses," *Nature* **414**, 182 (2001).
26. M. Hentschel, R. Kienberger, Ch. Spielmann, G.A. Reider, N. Milosevic, T. Brabec, P. Corkum, U. Heinzmann, M. Drescher, F. Krausz, "Attosecond metrology," *Nature* **414**, 511 (2001).
27. M. Nisoli, S. De Silvestri, O. Svelto, R. Szipöcs, K. Ferenz, C. Spielmann, S. Sartania, and F. Krausz, "Compression of High Energy Laser Pulses Below 5 fs," *Opt. Lett.* **22**, 522 (1997).
28. G. Cerullo, S. D. Silvestri, M. Nisoli, S. Sartania, S. Stagira, and O. Svelto, "Few-Optical-Cycle Laser Pulses: From High Peak Power to Frequency Tunability," *IEEE J. Sel. Topics Quant. Electronics* **6**, 948 (2000).
29. N. Karasawa, L. Li, A. Suguro, H. Shigekawa, R. Morita, M. Yamashita, "Optical pulse compression to 5.0 fs by use of only a spatial light modulator for phase compensation," *J. Opt. Soc. Am. B* **18**, 1742 (2001).
30. A. Baltuska, M. S. Pshenichnikov, and D. A. Wiersma, "Amplitude and phase characterization of 4.5-fs pulses by frequency-resolved optical gating," *Opt. Lett.* **23**, 1474 (1998).

31. A. Baltuska, T. Fuji, T. Kobayashi, "Visible pulse compression to 4 fs by optical parametric amplification and programmable dispersion control," *Opt. Lett.* **27**, 306 (2002).
32. J. C. Knight, T. A. Birks, P. S. Russell, and D. M. Atkin, "All-silica single-mode optical fiber with photonic crystal cladding," *Opt. Lett.* **21**, 1547 (1996).
33. G. P. Agrawal, *Nonlinear Fiber Optics* (Academic Press, San Diego, CA, 2001)
34. Y. R. Shen, *The Principles of Nonlinear Optics* (John Wiley & Sons, New York, 1984)
35. R. H. Stolen, and C. Lin, "Self-phase-modulation in silica optical fibers," *Phys. Rev. A* **17**, 1448 (1978).
36. A. Hasegawa, and F. Tappert, "Transmission of stationary nonlinear optical pulses in dispersive dielectric fibers. I. Anomalous dispersion," *Appl. Phys. Lett.* **23**, 142 (1973).
37. R. H. Stolen, E. P. Ippen, and A. R. Tynes, "Raman Oscillation in Glass Optical Waveguide," *Appl. Phys. Lett.* **20**, 62 (1972).
38. E. P. Ippen, and R. H. Stolen, "Stimulated Brillouin scattering in optical fibers," *Appl. Phys. Lett.* **21**, 539 (1972).
39. E. P. Ippen, *Laser Applications to Optics and Spectroscopy*, Addison-Wesley **2**, (1975).
40. E. Bourkoff, W. Zhao, R. I. Joseph, and D. N. Christodoulides, "Evolution of femtosecond pulses in single-mode fibers having higher-order nonlinearity and dispersion," *Opt. Lett.* **12**, 272 (1987).
41. F. M. Mitschke, and L. F. Mollenauer, "Discovery of the soliton self-frequency shift," *Opt. Lett.* **11**, 659 (1986).
42. J. P. Gordon, "Theory of the soliton self-frequency shift," *Opt. Lett.* **11**, 662 (1986).
43. F. DeMartini, C. H. Townes, T. K. Gustafson, and P. L. Kelley, "Self-Steepening of Light Pulses," *Phys. Rev.* **164**, 312 (1967).
44. D. Grischkowsky, E. Courtens, and J. A. Armstrong, "Observation of Self-Steepening of Optical Pulses with Possible Shock Formation," *Phys. Rev. Lett.* **31**, 422 (1973).
45. R. H. Stolen, J. P. Gordon, W. J. Tomlinson, and H. A. Haus, "Raman response function of silica-core fibers," *J. Opt. Soc. Am. B* **6**, 1159 (1989).
46. H. Nakatsuka, D. Grischkowsky, and A. C. Balant, "Nonlinear picosecond-pulse propagation through optical fibers with positive group velocity dispersion," *Phys. Rev. Lett.* **47**, 910 (1981).
47. R. L. Fork, C. H. B. Cruz, P. C. Becker, and C. V. Shank, "Compression of optical pulses to six femtoseconds by using cubic phase compensation," *Opt. Lett.* **12**, 483 (1987).
48. A. Baltuska, Z. Wei, M. S. Pshenichnikov, and D. A. Wiersma, "Optical pulse compression to 5 fs at 1 MHz repetition rate," *Opt. Lett.* **22**, 102 (1997).
49. C. Rolland, and P. B. Corkum, "Compression of high-power optical pulses," *J. Opt. Soc. Am. B* **5**, 641 (1988).

50. M. Nisoli, S. Stagira, S. D. Silvestri, O. Svelto, S. Sartania, Z. Cheng, G. Tempea, C. Spielmann, and F. Krausz, "Toward a terawatt-scale sub-10-fs laser technology," *IEEE J. Sel. Top. Quantum Electron.* **4**, 414 (1998).
51. E. A. J. Marcatili, and R. A. Schmeltzer, "Hollow metallic and dielectric waveguides for long distance optical transmission and lasers," *Bell Syst. Tech. J.* **43**, 1783 (1964).
52. M. Nisoli, S. Stagira, S. D. Silvestri, O. Svelto, S. Sartania, Z. Cheng, M. Lenzner, C. Spielmann, and F. Krausz, "A novel high-energy pulse compression system: generation of multigigawatt sub-5-fs pulses," *Appl. Phys. B* **65**, 189 (1997).
53. G. P. Agrawal, *Nonlinear Fiber Optics* (Academic Press, Inc., 1995)
54. W. J. Tomlinson, R. H. Stolen, and C. V. Shank, "Compression of optical pulses chirped by self-phase modulation in fibers," *J. Opt. Soc. Am. B* **1**, 139 (1984).
55. P. Russell, "Photonic Crystal Fibers," *Science* **299**, 358 (2003).
56. J. C. Knight, "Photonic crystal fibres," *Nature* **424**, 847 (2003).
57. T. A. Birks, J. C. Knight, and P. S. Russell, "Endlessly single-mode photonic crystal fiber," *Opt. Lett.* **22**, 961 (1997).
58. J. K. Ranka, R. S. Windeler, and A. J. Stentz, "Optical properties of high-delta air-silica microstructure optical fibers," *Opt. Lett.* **25**, 796 (2000).
59. W. H. Reeves, J. C. Knight, P. S. Russell, and P. J. Roberts, "Demonstration of ultra-flattened dispersion in photonic crystal fibers," *Opt. Express* **10**, 609 (2002).
60. W. J. Wadsworth, A. Ortigosa-Blanch, J. C. Knight, T. A. Birks, T.-P. M. Man, and P. S. Russell, "Supercontinuum generation in photonic crystal fibers and optical fiber tapers: a novel light source," *J. Opt. Soc. Am. B* **19**, 2148 (2002).
61. I. Hartl, X. D. Li, C. Chudoba, R. K. Ghanta, T. H. Ko, J. G. Fujimoto, J. K. Ranka, and R. S. Windeler, "Ultrahigh-resolution optical coherence tomography using continuum generation in an air-silica microstructure optical fiber," *Opt. Lett.* **26**, 608 (2001).
62. T. Udem, R. Holzwarth, and T. W. Hänsch, "Optical frequency metrology," *Nature* **416**, 233 (2002).
63. S. Coen, A. H. L. Chau, R. Leonhardt, J. D. Harvey, J. C. Knight, W. J. Wadsworth, and P. S. J. Russell, "Supercontinuum generation by stimulated Raman scattering and parametric four-wave mixing in photonic crystal fibers," *J. Opt. Soc. Am. B* **19**, 753 (2002).
64. J. K. Ranka, and R. S. Windeler, "Nonlinear Interactions in Air-Silica Microstructure Optical Fibers," *OPN*, **20** (August 2000).
65. G. Genty, M. Lehtonen, H. Ludvigsen, J. Broeng, and M. Kaivola, "Spectral broadening of femtosecond pulses into continuum radiation in microstructured fibers," *Opt. Express* **10**, 1083 (2002).
66. K. P. Hansen, J. R. Jensen, D. Birkedal, J. M. Hvam, and A. Bjarklev, "Pumping wavelength dependence of super continuum generation in photonic crystal fibers," in *Conference on Optical Fiber Communication OFC*, 2002.

67. A. V. Husakou, and J. Herrmann, "Supercontinuum Generation of Higher-Order Solitons by Fission in Photonic Crystal Fibers," *Phys. Rev. Lett.* **87**, 203901 (2001).
68. A. L. Gaeta, "Nonlinear propagation and continuum generation in microstructured optical fibers," *Opt. Lett.* **27**, 924 (2002).
69. R. L. Fork, O. E. Martinez, and J. P. Gordon, "Negative dispersion using pairs of prisms," *Opt. Lett.* **9**, 150 (1984).
70. E. B. Treacy, "Optical Pulse Compression with Diffraction Gratings," *IEEE J. Quantum Electron.* **5**, 454 (1969).
71. W. Kaiser, Eds., *Ultrashort Laser Pulses*, vol. 60 (Springer Verlag, 1988).
72. R. Szipöcs, K. Ferencz, C. Spielmann, and F. Krausz, "Chirped multilayer coatings for broadband dispersion control in femtosecond lasers," *Opt. Lett.* **19**, 201 (1994).
73. F. X. Kärtner, N. Matuschek, T. Schibli, U. Keller, H. A. Haus, C. Heine, R. Morf, V. Scheuer, M. Tilsch, and T. Tschudi, "Design and fabrication of double-chirped mirrors," *Opt. Lett.* **22**, 831 (1997).
74. N. Matuschek, F. X. Kärtner, and U. Keller, "Theory of Double-Chirped Mirrors," *IEEE J. of Sel. Topics in Quantum Electronics* **4**, 197 (1998).
75. E. Zeek, K. Maginnis, S. Backus, U. Russek, M. Murnane, G. Mourou, H. Kapteyn, and G. Vdovin, "Pulse compression by use of deformable mirrors," *Opt. Lett.* **24**, 493 (1999).
76. A. M. Weiner, D. E. Leaird, J. S. Patel, and J. R. Wullert, "Programmable femtosecond pulse shaping by use of a multielement liquid-crystal phase modulator," *Opt. Lett.* **15**, 326 (1990).
77. A. M. Weiner, "Femtosecond pulse shaping using spatial light modulators," *Rev. Sci. Instrum.* **71**, 1929 (2000).
78. R. Trebino, and D. J. Kane, "Using phase retrieval to measure the intensity and phase of ultrashort pulses: frequency-resolved optical gating," *J. Opt. Soc. Am. A* **10**, 1101 (1993).
79. R. Trebino, K. W. DeLong, D. N. Fittinghoff, J. Sweetser, M. A. Krumbügel, and B. Richman, "Measuring ultrashort laser pulses in the time-frequency domain using frequency-resolved optical gating," *Rev. Sci. Instrum.* **68**, 1–19 (1997).
80. C. Iaconis, and I. A. Walmsley, "Self-Referencing Spectral Interferometry for Measuring Ultrashort Optical Pulses," *IEEE J. Quantum Electron.* **35**, 501 (1999).
81. L. Gallmann, D. H. Sutter, N. Matuschek, G. Steinmeyer, U. Keller, C. Iaconis, and I. A. Walmsley, "Characterization of sub-6-fs optical pulses with spectral phase interferometry for direct electric-field reconstruction," *Opt. Lett.* **24**, 1314 (1999).
82. L. F. Mollenauer, R. H. Stolen, and J. P. Gordon, "Experimental Observation of Picosecond Pulse Narrowing and Solitons in Optical Fibers," *Phys. Rev. Lett.* **45**, 1095 (1980).
83. D. Grischkowsky, and A. C. Balant, "Optical pulse compression based on enhanced frequency chirping," *Appl. Phys. Lett.* **41**, 1 (1982).

84. C. V. Shank, R. L. Fork, R. Yen, R. H. Stolen, and W. J. Tomlinson, "Compression of femtosecond optical pulses," *Appl. Phys. Lett.* **40**, 761 (1982).
85. D. H. Sutter, G. Steinmeyer, L. Gallmann, N. Matuschek, F. Morier-Genoud, U. Keller, V. Scheuer, G. Angelow, and T. Tschudi, "Semiconductor saturable-absorber mirror-assisted Kerr-lens mode-locked Ti:sapphire laser producing pulses in the two-cycle regime," *Opt. Lett.* **24**, 631 (1999).
86. R. Ell, U. Morgner, F. X. Kärtner, J. G. Fujimoto, E. P. Ippen, V. Scheuer, G. Angelow, T. Tschudi, M. J. Lederer, A. Boiko, and B. Luther-Davies, "Generation of 5-fs pulses and octave-spanning spectra directly from a Ti:sapphire laser," *Opt. Lett.* **26**, 373 (2001).
87. N. Matuschek, L. Gallmann, D. H. Sutter, G. Steinmeyer, and U. Keller, "Back-Side coated chirped mirror with ultra-smooth broadband dispersion characteristics," *Appl. Phys. B* **71**, 509 (2000).
88. J. A. Dobrowolski, A. V. Tikhonravov, M. K. Trubetskov, B. T. Sullivan, and P. G. Verly, "Optimal single-band normal-incidence antireflection coatings," *Appl. Opt.* **35**, 644 (1996).
89. G. Tempea, "Tilted-front-interface chirped mirrors," *JOSA B* **18**, 1747 (2001).
90. G. Steinmeyer, "Brewster-angled chirped mirrors for high-fidelity dispersion compensation and bandwidths exceeding one optical octave," *Opt. Express* **11**, 2385 (2003).
91. D. Yelin, D. Meshulach, and Y. Silberberg, "Adaptive femtosecond pulse compression," *Opt. Lett.* **22**, 1793 (1997).
92. D. Meshulach, D. Yelin, and Y. Silberberg, "Adaptive real-time femtosecond pulse shaping," *J. Opt. Soc. Am. B* **15**, 1615 (1998).
93. A. Efimov, M. D. Moores, N. M. Beach, J. L. Krause, and D. H. Reitze, "Adaptive control of pulse phase in a chirped-pulse amplifier," *Opt. Lett.* **23**, 1915 (1998).
94. T. Baumert, T. Brixner, V. Seyfried, M. Strehle, and G. Gerber, "Femtosecond pulse shaping by an evolutionary algorithm with feedback," *Appl. Phys. B* **65**, 779 (1997).
95. T. Brixner, M. Strehle, and G. Gerber, "Feedback-controlled optimization of amplified femtosecond laser pulses," *Appl. Phys. B* **68**, 281 (1999).
96. A. Assion, T. Baumert, M. Bergt, T. Brixner, B. Kiefer, V. Seyfried, M. Strehle, and G. Gerber, "Control of chemical reactions by feedback-optimized phase-shaped femtosecond laser pulses," *Science* **282**, 919 (1998).
97. C. J. Bardeen, V. V. Yakovlev, K. R. Wilson, S. D. Carpenter, P. M. Weber, and W. S. Warren, "Feedback quantum control of molecular electronic population transfer," *Chem. Phys. Lett.* **280**, 151 (1997).
98. T. C. Weinacht, J. Ahn, and P. H. Bucksbaum, "Controlling the shape of a quantum wavefunction," *Nature* **397**, 233 (1999).
99. A. M. Weiner, "Femtosecond optical pulse shaping and processing," *Prog. Quant. Electr.* **19**, 161 (1995).

100. A. M. Weiner, J. P. Heritage, and E. M. Kirschner, "High-resolution femtosecond pulse shaping," *J. Opt. Soc. Am. B* **5**, 1563 (1988).
101. A. M. Weiner, J. P. Heritage, and J. A. Salehi, "Encoding and decoding of femtosecond pulses," *Opt. Lett.* **13**, 300 (1988).
102. D. H. Reitze, A. M. Weiner, and D. E. Leaird, "Shaping of wide bandwidth 20 femtosecond optical pulses," *Appl. Phys. Lett.* **61**, 1260 (1992).
103. C. Froehly, B. Colombeau, and M. Vampouille, *Progress in Optics* **20**, edited by E. Wolf (1983).
104. A. M. Weiner, D. E. Leaird, J. S. Patel, and J. R. Wullert, "Programmable shaping of femtosecond optical pulses by use of 128-element liquid crystal phase modulator," *IEEE J. Quantum Electron.* **28**, 908 (1992).
105. A. Efimov, C. Schaffer, and D. H. Reitze, "Programmable shaping of ultrabroad-bandwidth pulses from a Ti:sapphire laser," *J. Opt. Soc. Am. B* **12**, 1968 (1995).
106. E. Zeek, R. Bartels, M. M. Murnane, H. C. Kapteyn, S. Backus, and G. Vdovin, "Adaptive pulse compression for transform-limited 15-fs high-energy pulse generation," *Opt. Lett.* **25**, 587 (2000).
107. A. Baltuska, and T. Kobayashi, "Adaptive shaping of two-cycle visible pulses using a flexible mirror," *Appl. Phys. B* **75**, 427 (2002).
108. B. Schenkel, J. Biegert, U. Keller, C. Vozzi, M. Nisoli, G. Sansone, S. Stagira, S. D. Silvestri, and O. Svelto, "Generation of 3.8-fs pulses from adaptive compression of a cascaded hollow fiber supercontinuum," *Opt. Lett.* **28**, 1987 (2003).
109. J. W. Nicholson, J. Jasapara, W. Rudolph, F. G. Omenetto, and A. J. Taylor, "Full-field characterization of femtosecond pulses by spectrum and cross-correlation measurements," *Opt. Lett.* **24**, 1774 (1999).
110. H. A. Haus, C. V. Shank, and E. P. Ippen, "Shape of passively mode-locked laser pulses," *Opt. Commun.* **15**, 29 (1975).
111. C. Iaconis, and I. A. Walmsley, "Spectral Phase Interferometry for Direct Electric Field Reconstruction of Ultrashort Optical Pulses," *Opt. Lett.* **23**, 792 (1998).
112. M. Takeda, H. Ina, and S. Kobayashi, "Fourier-transform method of fringe-pattern analysis for computer-based topography and interferometry," *J. Opt. Soc. Am. B* **72**, 156 (1982).
113. W. Kornelis, J. Biegert, J.W.G. Tisch, M. Nisoli, G. Sansone, C. Vozzi, S. De Silvestri, U. Keller, "Single-shot kilohertz characterization of ultrashort pulses by spectral phase interferometry for direct electric-field reconstruction," *Opt. Lett.* **28**, 281 (2003).
114. M. Zavelani-Rossi, G. Cerullo, S. D. Silvestri, L. Gallmann, N. Matuschek, G. Steinmeyer, U. Keller, G. Angelow, V. Scheuer, and T. Tschudi, "Pulse compression over a 170-THz bandwidth in the visible by use of only chirped mirrors," *Opt. Lett.* **26**, 1155 (2001).

115. M. E. Anderson, L. E. E. de Araujo, E. M. Kosik, and I. A. Walmsley, "The effects of noise on ultrashort-optical-pulse measurement using SPIDER," *Appl. Phys. B* **70**, 85 (2000).
116. G. McConnell, and E. Riis, "Ultra-short pulse compression using photonic crystal fibre," *Appl. Phys. B*, published online 13 Feb 2004 (2004).
117. S. Lako, J. Seres, P. Apai, J. Balazs, R. S. Windeler, and R. Szipöcs, "Pulse compression of nanojoule pulses in the visible using microstructure optical fiber and dispersion compensation," *Appl. Phys. B* **76**, 267 (2003).
118. J. M. Dudley, and S. Coen, "Coherence properties of supercontinuum spectra generated in photonic crystal and tapered optical fibers," *Opt. Lett.* **27**, 1180 (2002).
119. J. M. Dudley, X. Gu, L. Xu, M. Kimmel, E. Zeek, P. O'Shea, R. Trebino, S. Coen, and R. S. Windeler, "Cross-correlation frequency resolved optical gating analysis of broadband continuum generation in photonic crystal fiber: simulations and experiments," *Opt. Express* **10**, 1215 (2002).
120. X. Gu, L. Xu, M. Kimmel, E. Zeek, P. O'Shea, A. P. Shreenath, R. Trebino, and R. S. Windeler, "Frequency-resolved optical gating and single-shot spectral measurements reveal fine structure in microstructure-fiber continuum," *Opt. Lett.* **27**, 1174 (2002).
121. K. L. Corwin, N. R. Newbury, J. M. Dudley, S. Coen, S. A. Diddams, K. Weber, and R. S. Windeler, "Fundamental Noise Limitations to Supercontinuum Generation in Microstructure Fiber," *Phys. Rev. Lett.* **90**, 113904 (2003).
122. K. L. Corwin, N. R. Newbury, J. M. Dudley, S. Coen, S. A. Diddams, B. R. Washburn, K. Weber, and R. S. Windeler, "Fundamental amplitude noise limitations to supercontinuum spectra generated in a microstructured fiber," *Appl. Phys. B*, published online 24 Jun 2003 (2003).
123. G. Chang, T. B. Norris, and H. G. Winful, "Optimization of supercontinuum generation in photonic crystal fibers for pulse compression," *Opt. Lett.* **28**, 546 (2003).

Curriculum Vitae

Personal Data

Name: Birgit Schenkel
Date of birth: March 15, 1976
Place of birth: Karlsruhe, Germany
Nationality: German

School Education

1982-1994 *Europäische Schule*, Luxembourg
07/1994 *Abitur*

University

1994-2000 Study of physics at the University of Heidelberg, Germany
04/2000 Diploma in physics from the University of Heidelberg
Diploma thesis: "*Aufbau eines elektrooptischen Ellipsometers zur Bestimmung der Doppelbrechung der Hornhaut*"
(Kirchhoff-Institut für Physik)
06/2000-06/2004 Ph.D. studies at the Swiss Federal Institute of Technology Zurich, Switzerland

Danksagung

An dieser Stelle möchte ich mich ganz herzlich bei allen Freunden und Kollegen bedanken, die zum Erfolg dieser Doktorarbeit beigetragen haben. Insbesondere gilt mein Dank:

Prof. Dr. Ursula Keller, für die Möglichkeit, in ihrer Gruppe diese Arbeit auf einem aktuellen und interessanten Gebiet durchführen zu können.

Prof. Dr. Mauro Nisoli, for serving on my thesis committee and for giving me the opportunity to perform my experiments in his laboratory in Milano for several weeks.

Dr. Jens Biegert, für die Betreuung der Hohlfaser-Experimente und für die Übernahme des Koreferats.

PD Dr. Rüdiger Paschotta, für seine wertvolle Hilfe bei den numerischen Simulationen zur Pulspropagation durch Mikrostruktur-Fasern.

PD Dr. Günter Steinmeyer, für die Betreuung dieser Arbeit in den ersten beiden Jahren.

Ganz besonders möchte ich mich bei Mathis Bruck, Lukas Gallmann, Anastasia Gosteva, Christoph Hauri, Wouter Kornelis, Jens Kunde, und Thomas Rupp bedanken, mit denen ich im Laufe meiner Arbeit das Büro geteilt habe, für die stets lockere Atmosphäre und den einen oder anderen Büroplausch.

Rosmarie Ehram, für ihre “Wetterberichte” und für ihr einfühlsames Zuhören, wenn es einem mal nicht so gut ging.

Ich danke ebenfalls allen anderen ehemaligen und aktuellen Doktoranden der Arbeitsgruppe für das ausgezeichnete Arbeitsklima untereinander. Namentlich sind dies (ohne Berücksichtigung von Titeln): Marc Achermann, Alex Aschwanden, Felix Brunner, Henry Frick, Tobias Fritz, Rachel Grange, Reto Häring, Markus Haiml, Arne Heinrich, Florian Helbing, Edith Innerhofer, Lukas Krainer, Steve Lecomte, Valeria Liverini, Dirk Lorensen, Deran Maas, Sergio Vincenzo Marchese, Andreas Rutz, Adrian Schlatter, Gabriel Spühler, Gert Wrigge, und Simon Zeller.

Ein weiteres Dankeschön geht an alle anderen aktuellen und ehemaligen Mitarbeiter der Gruppe, Marcel Anscombe, Dirk Ebling, Matthias Golling, Philip Schlup, Silke Schön, John Tisch und Heiko Unold.

Ausserdem danke ich Harald Hediger und den Mitarbeitern in der Mechanikwerkstatt für die präzise, schnelle und zuverlässige Ausführung aller Aufträge.

Important parts of this thesis would not have been possible without the collaboration with groups from outside of ETH Zurich. I would like to thank the people in Prof. Sandro DeSilvestri's group at the Politecnico di Milano for a very fruitful collaboration. Special thanks go to Prof. Mauro Nisoli, Giuseppe Sansone, Caterina Vozzi, and Salvatore Stagira. Furthermore, I would like to thank Prof. John Dudley from the Université de Franche-Comté for helpful discussions on the numerical simulation of pulse propagation through microstructure fibers and for the calculation of the fibers dispersion profile.

Ferner gilt mein Dank meinen Eltern und Geschwistern für die vielen aufmunternden Worte in schwierigen Zeiten meiner Doktorarbeit.

Mein letzter und ganz besonderer Dank geht an meinen Verlobten und baldigen Ehemann Lukas Gallmann, der mir nicht nur mit unzähligen fachlichen Tipps zur Seite gestanden hat, sondern der Grund dafür war, dass ich jeden Abend mit einem Lächeln nach Hause gegangen bin.

Zürich, Juni 2004